

NANOCRYSTAL SILICON BASED VISIBLE LIGHT EMITTING PIN DIODES

A THESIS SUBMITTED TO
THE GRADUATE SCHOOL OF NATURAL AND APPLIED SCIENCES
OF
MIDDLE EAST TECHNICAL UNIVERSITY

BY

MUSTAFA ANUTGAN

IN PARTIAL FULFILLMENT OF THE REQUIREMENTS
FOR
THE DEGREE OF DOCTOR OF PHILOSOPHY
IN
PHYSICS

DECEMBER 2010

Approval of the thesis:

NANOCRYSTAL SILICON BASED VISIBLE LIGHT EMITTING PIN DIODES

submitted by **MUSTAFA ANUTGAN** in partial fulfillment of the requirements for the degree of **Doctor of Philosophy in Physics Department, Middle East Technical University** by,

Prof. Dr. Canan Özgen
Dean, Graduate School of **Natural and Applied Sciences**

Prof. Dr. Sinan Bilikmen
Head of Department, **Physics**

Prof. Dr. Bayram Katırcıoğlu
Supervisor, **Physics Dept., METU**

Examining Committee Members:

Assoc. Prof. Dr. İsmail Atılgan
Physics Dept., METU

Prof. Dr. Bayram Katırcıoğlu
Physics Dept., METU

Prof. Dr. İbrahim Günel
Physics Dept., METU

Prof. Dr. Bülent Akınoğlu
Physics Dept., METU

Assoc. Prof. Dr. Barış Akaoğlu
Engineering Physics Dept., Ankara University

Date:

I hereby declare that all information in this document has been obtained and presented in accordance with academic rules and ethical conduct. I also declare that, as required by these rules and conduct, I have fully cited and referenced all material and results that are not original to this work.

Name, Last Name: MUSTAFA ANUTGAN

Signature :

ABSTRACT

NANOCRYSTAL SILICON BASED VISIBLE LIGHT EMITTING PIN DIODES

Anutgan, Mustafa

Ph.D., Department of Physics

Supervisor : Prof. Dr. Bayram Katırcıoğlu

December 2010, 135 pages

The production of low cost, large area display systems requires a light emitting material compatible with the standard silicon (Si) based complementary metal oxide semiconductor (CMOS) technology. The crystalline bulk Si is an indirect band semiconductor with very poor optical properties. On the other hand, hydrogenated amorphous Si (a-Si:H) based wide gap alloys exhibit strong visible photoluminescence (PL) at room temperature, owing to the release of the momentum conservation law. Still, the electroluminescence (EL) intensity from the diodes based on these alloys is weak due to the limitation of the current transport by the localized states.

In the frame of this work, first, the luminescent properties of amorphous silicon nitride (a-SiN_x:H) thin films grown in a plasma enhanced chemical vapor deposition (PECVD) system were analyzed with respect to the nitrogen content. Then, the doping efficiency of *p*- and *n*-type hydrogenated nanocrystalline Si (nc-Si:H) films was optimized via adjusting the deposition conditions. Next, the junction quality of these doped layers was checked and further improved in a homojunction *pin* diode.

Heterojunction *pin* light emitting diodes (LEDs) were fabricated with a-SiN_x:H as the luminescent active layer. The EL efficiency of the fresh diodes was very low, as expected.

As a solution, the diodes were electro-formed under high electric field leading to nanocrystallization accompanied by a strong visible light emission from the whole diode area. The current-voltage (I-V) and EL properties of these transformed diodes were investigated in detail.

Keywords: hydrogenated amorphous silicon nitride, thin film *pin* LED, efficiency, forming process, nanocrystallization

ÖZ

NANOKRİSTAL SİLİSYUM TABANLI GÖRÜNÜR IŞIK YAYAN PIN DİYOTLAR

Anutgan, Mustafa

Doktora, Fizik Bölümü

Tez Yöneticisi : Prof. Dr. Bayram Katırcıoğlu

Aralık 2010, 135 sayfa

Geniş yüzeylerde düşük maliyetli gösterim sistemlerinin üretimi, standart silisyum (Si) tabanlı tamlayıcı metal oksit yarıiletken (CMOS) teknolojisiyle uyumlu ışık yayan bir malzeme gerektirmektedir. Dolaylı yasak enerjili bir yarıiletken olan kristal Si çok zayıf optik özelliklere sahiptir. Hidrojenlenmiş amorf Si (a-Si:H) tabanlı geniş yasak enerji aralıklı alaşımlar ise, momentum korunumunun esnemesi sayesinde, oda sıcaklığında görünür bölgede güçlü foto-ışım (PL) sergilerler. Ancak bu alaşımlar kullanılarak üretilen diyotların elektro-ışım (EL) şiddeti, akım yoğunluğunun, yerleşmiş kusurlar tarafından sınırlandırılması nedeniyle yetersiz kalır.

Bu çalışma çerçevesinde, önce, plazma destekli kimyasal buhar biriktirme (PECVD) sistemi ile büyütülen amorf silisyum nitrür (a-SiN_x:H) ince filmlerin ışım özellikleri azot miktarına göre analiz edildi. Sonra, üretim koşulları değiştirilerek *p*- ve *n*-tipi hidrojenlenmiş nanokristal Si (nc-Si:H) filmlerin katkılanma verimliliği en uygun hale getirildi. Daha sonra ise, bu katkılanmış tabakaların kalitesi türdeş eklem *pin* yapılar denetlenerek geliştirildi.

Türlü eklem *pin* ışık yayan yapılarda (LEDs), ışıyan etkin tabaka olarak a-SiN_x:H kullanıldı. Taze diyotların EL verimliliği beklendiği gibi çok düşüktü. Çözüm olarak, üretilen diyotların etkin tabakası, yüksek elektrik alan altında, yer yer nano-kristal Si oluşumuna

uđratılarak, tüm diyot yüzeyinden güçlü görünür ışıma elde edilmiştir. Bu dönüşmüş yapının akım-voltaj (I-V) ve EL özellikleri ayrıntılı incelenmiştir.

Anahtar Kelimeler: hidrojenlenmiş amorf silisyum nitür, ince film *pin* LED, verimlilik, oluşum süreci, nanokristalizasyon

To my wife

ACKNOWLEDGMENTS

I would first like to thank my thesis advisors Prof. Dr. Bayram Katirciođlu and Assoc. Prof. Dr. İsmail Atılgan for their guidance in my Ph.D. thesis research.

I acknowledge Prof. Dr. Bayram Katirciođlu for conducting scientific discussions and debates on my experimental results.

The help and advices of Assoc. Prof. Dr. İsmail Atılgan at all the stages of the experimental works are appreciated.

I am grateful to The Scientific and Technological Research Council of Turkey (TÜBİTAK) for the financial support provided during my Ph.D. study. In addition, I thank the Middle East Technical University Scientific Research Project Coordination (METU-BAP) for supplying some of the necessary laboratory materials.

I thank Mustafa Kulakçı for his practical advices in the photoluminescence measurements. Also, the special thanks go to Nazım Dugan who helped me to take the photographs of the LEDs with his semi-professional camera.

I am thankful to Uđur Yalçıner and Taylan Zeyrek for their help during the patent application.

I thank my parents and sister for their love and patience during my academic work.

Finally, I express my gratitude to my wife and colleague, Tamila Aliyeva Anutgan, for being respectful to my efforts during my tough times. Her advices, analyses, critical reading of the manuscript and being involved in some of the experiments have enriched this work.

TABLE OF CONTENTS

ABSTRACT	iv
ÖZ	vi
ACKNOWLEDGMENTS	ix
TABLE OF CONTENTS	x
LIST OF TABLES	xiii
LIST OF FIGURES	xiv
CHAPTERS	
1 INTRODUCTION	1
1.1 Review on light sources	1
1.2 Silicon based photonics	2
1.3 Radiative recombination in amorphous semiconductors	5
1.4 Doping and related defects in a-Si:H	10
1.5 Hydrogenated amorphous silicon based pin diodes	13
1.6 Light extraction from a-SiN _x :H based diodes	18
1.7 Thesis outline	22
2 ABSORPTION AND RECOMBINATION PROPERTIES OF a-SiN _x :H THIN FILMS	23
2.1 Introduction	23
2.2 Experimental details	24
2.3 Results and discussions	25
2.3.1 Optical absorption properties	25
2.3.2 Recombination properties by PL spectroscopy	30
2.3.3 Analyses on PL efficiency	36

2.4	Conclusion	39
3	DOPING OF HYDROGENATED NANOCRYSTALLINE SILICON	41
3.1	Introduction	41
3.2	Experimental details	43
3.3	Results and discussions	44
3.4	Conclusion	48
4	FABRICATION OF HYDROGENATED AMORPHOUS SILICON HOMO- JUNCTION PIN DIODE	49
4.1	Introduction	49
4.2	Experimental details	49
4.3	Results and discussions	54
4.3.1	Deposition parameters for optimum pin diode	54
4.3.2	I-V measurements of the optimized pin diode	56
4.3.3	DOS calculation from SCLC and CPM results	60
4.4	Conclusion	63
5	ELECTROLUMINESCENT a-SiN _x :H BASED PIN DIODES	64
5.1	Introduction	64
5.2	Experimental details	65
5.3	Results and discussions	68
5.3.1	Forming process of pin diodes	68
5.3.2	Electrical characteristics of formed pin diodes	79
5.3.2.1	Low field regime	79
5.3.2.2	Intermediate field regime	84
5.3.2.3	High field regime	87
5.3.2.4	Memory effect in the formed pin diodes	89
5.3.3	Electroluminescence from formed pin diodes	94
5.4	Conclusion	103
6	SUMMARY	105
	REFERENCES	108
	APPENDICES	

A	PHOTOMETRY	114
B	LITERATURE REVIEW CHARTS FOR THE LUMINESCENT PROPERTIES OF a-SiN _x :H THIN FILMS	118
C	SPECTRAL RESPONSIVITIES OF THE PHOTODETECTORS	124
D	DERIVATION OF THE TOTAL ABSORBED LIGHT FRACTION USED IN PL INTENSITY CORRECTION	126
E	SPACE CHARGE LIMITED CURRENT SPECTROSCOPY	129
F	BAND-TAIL HOPPING RESULTS FOR D3	133
VITA	134

LIST OF TABLES

TABLES

Table 1.1	Deposition parameters for the layers of the first a-SiN _x :H <i>pin</i> LED. After [40].	19
Table 2.1	Gas flow parameters of the a-SiN _x :H film deposition.	24
Table 2.2	Optical constants of a-SiN _x :H films deposited in this work.	29
Table 3.1	Deposition parameters and the corresponding dark resistivities of <i>p</i> -type nc-Si:H films at the center and near the edge of the reactor bottom electrode. During all deposition processes, the substrate temperature was maintained at 473 K. . . .	43
Table 4.1	Deposition parameters of <i>p</i> ⁺ nc-Si:H and a-Si:H films used in homojunction a-Si:H based <i>pin</i> diodes. The <i>n</i> ⁺ nc-Si:H film and the substrate temperature of 473 K were kept the same for all diodes. The <i>p</i> ⁺ nc-Si:H and a-Si:H films were grown under the RF power density of 160 and 22 mW/cm ² , respectively. The B ₂ H ₆ gas was 1000 ppm diluted in H ₂	51
Table 5.1	Deposition parameters of the intrinsic a-Si:H and a-SiN _x :H films used in the <i>pin</i> diodes of this work. The chamber pressure of 0.5 Torr and RF power density of 22 mW/cm ² were used during the growth of all these intrinsic layers.	65

LIST OF FIGURES

FIGURES

Figure 1.1 Radiative and non-radiative recombination processes of an optically excited EHP.	6
Figure 1.2 Band diagrams of a-Si:H based homojunction <i>pin</i> diode under various conditions (a) equilibrium, (b) forward bias and (c) reverse bias.	14
Figure 1.3 Simulation of the forward I-V curve of a <i>pin</i> diode for various (a) ideality factors, (b) temperatures ($\eta = 1.5$), (c) activation energies, (d) ohmic resistances, (e) voltage drops due to SCLC transport. In (f), the reverse I-V curve is simulated for different temperatures. Here, the parameters that are not changed in each graph are taken as $T = 300$ K, $1/\eta = 1/\eta_0 + T/(3090)$, $I_{r,SAT} = 30e^{-\frac{E_a}{kT}}$ A, $E_a = 0.83$ eV, $R_s = 25 \Omega$, $V_b = 40I^{1/2}$	17
Figure 1.4 Schematic cross sectional view of the first a-SiN _x :H LED.	19
Figure 2.1 Experimental setup for the temperature-scanned PL measurements.	26
Figure 2.2 (a) FTIR spectra of a-SiN _x :H films grown at different $r = \text{NH}_3/\text{SiH}_4$ flow ratios. (b) IR peak position of Si-N and N-H peaks versus r . (c) Bond densities as a function of r . (d) [N]/[Si] calculated from [Si-H]/[N-H] ratio and optical gap found from UV-visible spectra versus r . (e) Refractive index calculated from x and found from UV-visible spectra versus r	27
Figure 2.3 The fringing as-measured (symbols) and the fringe-free simulated (lines) PL spectra of four sets of a-SiN _x :H thin films deposited with different NH ₃ to SiH ₄ flow ratios. The ratio of the as-measured curve to the simulated one is given in the inset for the sample with $r = 4$. The transmittance spectrum of the same sample is provided for comparison.	30

Figure 2.4	Peak wavelength of the room temperature PL of a-SiN _x :H films and Stoke's shift presented with respect to the optical gap. Data at $E_{04}=1.8$ eV correspond to the usual values for a-Si:H.	31
Figure 2.5	(a) Square of the PL FWHM versus Stoke's shift for the a-SiN _x :H films. (b) The PL FWHM and (c) Stoke's shift plotted with respect to the subgap absorption tail.	34
Figure 2.6	(a) Corrected PL peak area and (b) the subgap absorption tail of a-SiN _x :H films versus r . (c) Corrected PL peak area of (a) versus $1/E_0$ of (b).	37
Figure 2.7	PL spectrum of SN3 film measured at different temperatures with the temperature dependence of the intensity provided in the inset.	38
Figure 3.1	Dark resistivity of p -type nc-Si:H films versus (a) pressure, where RF power density is 200 mW/cm ² and B ₂ H ₆ /SiH ₄ is 1.00%, (b) B ₂ H ₆ /SiH ₄ , where RF power density is 200 mW/cm ² and gas pressure is 1 Torr, (c) RF plasma power density, where the pressure is 1 Torr and B ₂ H ₆ /SiH ₄ is 0.17%.	45
Figure 3.2	(a) Optical gap, E_{04} and (b) subgap absorption tail, E_0 of p -type nc-Si:H films as a function of RF plasma power density, where the deposition pressure is 1 Torr and B ₂ H ₆ /SiH ₄ is 0.17%.	47
Figure 3.3	Distribution of dark resistivity along the reactor electrode of the film p8 and the corresponding n -type film grown using phosphine instead of diborane. . .	47
Figure 4.1	Fabrication steps of a-Si:H based homojunction pin diode.	50
Figure 4.2	Schematic of the complete homojunction pin diode used in electrical measurements with the bottom (Cr) and the top (Al) electrodes.	52
Figure 4.3	Experimental setup for the CPM measurements.	53
Figure 4.4	I-V characteristics at forward and reverse biases of homojunction a-Si:H based pin diodes: (a) #1 and #2, (b) #4, #3 and #2, (c) #5 and #2 (refer to Table 4.1).	55
Figure 4.5	I-V characteristics of homojunction a-Si:H based pin diode #5 at forward and reverse biases. The ideality factor η is found from the slope of the linear fit. The rectification ratio is indicated at 1.2 V.	57

Figure 4.6 (a) Temperature scan of the forward and reverse I-V characteristics of the diode #5 of area $7.8 \times 10^{-3} \text{ cm}^2$. (b) Arrhenius plot of the reverse saturation current. (c) Temperature dependence of the diode ideality factor.	58
Figure 4.7 Temperature scan of the forward current of diode #5 with respect to the voltage drop across the bulk of the sample, for which the series resistance is responsible. The slopes indicated by the dashed lines are guides for $J \propto V^a$ with $a=1$, 2 and 3.	60
Figure 4.8 Energy dependence of the optical absorption coefficient measured by CPM (○) and UV-visible transmittance (●) techniques from the <i>pin</i> diode #5.	61
Figure 4.9 Density of states (DOS) distribution within the forbidden gap of the intrinsic a-Si:H film determined from SCLC and CPM techniques. The dashed lines are the extrapolations of data for the exponential band tail states and the Gaussian distribution of the deep levels.	62
Figure 5.1 The schematic cross-sectional view of the complete <i>pin</i> structure used throughout EL and I-V experiments with the bottom (Cr) and the window (ITO) electrodes.	66
Figure 5.2 Experimental setup for temperature scanned EL and I-V measurements. . .	67
Figure 5.3 (a) Forward and (b) reverse I-V characteristics of a-Si:H based homojunction <i>pin</i> diode (D0) before and after the forming process. The numbers and the arrows represent the measurement sequence and the direction of the measurement, respectively. ΔI_f and ΔI_r indicate the difference between the currents at low voltage region before and after the forming process for the forward and reverse cases, respectively.	68
Figure 5.4 (a) The I-V characteristics and (b) the corrected EL spectrum of the diode D1 measured before and after the forming process. Inset shows the fitting of the noisy data of the fresh diode.	70
Figure 5.5 The current density versus time plot of D2 under a constant forward voltage stress of 12 V. Arrows at the beginning of the measurement and at about 400 s indicate the times at which the forming process starts and mostly ends, respectively. 72	

Figure 5.6 XRD spectra of (a) ITO coated a-SiN _x :H based <i>pin</i> diodes (D2) before and after the forming process, (b) glass/Cr structure to interpret the peak at 45° and (c) glass/ITO structure before and after its thermal annealing at 473 K for 30 min.	73
Figure 5.7 Possible energy band diagram of the diode D2 after the forming process. The quantum wells represent the nanocrystallites and the dashes are used for the energy levels. <i>d1</i> , <i>d2</i> and <i>d3</i> are the regions from low to high crystallization corresponding to average resistances <i>R1</i> , <i>R2</i> and <i>R3</i> respectively. The numbered arrows indicate possible recombination ways.	75
Figure 5.8 (a) Point contacts at <i>n</i> ⁺ /ITO interface due to the rough surface of <i>n</i> ⁺ nc-Si:H. (b) FP initiation at one of the point contacts followed by the formation of nc-Si islands within the intrinsic layer. (c) The resistance of the formed region, <i>R_a</i> , is less than the parallel resistances of the fresh parts of the diode, <i>R_{b#}</i>	78
Figure 5.9 Temperature dependence of the forward I-V characteristics of the diode D2 after the forming process. The inset shows the Arrhenius plot of the conductivity with two possible activation energies indicated.	80
Figure 5.10 (a) Si nanocrystallite surrounded by a-SiN _x :H matrix in D2. Dashes represent the localized states and the numbered arrows are used for the possible ways of tunneling. <i>E_{fund}</i> shows the fundamental level of the crystallite. <i>E_{C(SiN_x)}</i> and <i>E_{C(nc-Si)}</i> stand for the conduction band edge of a-SiN _x :H and that of the Si nanocrystallite, respectively. (b) Exponential band tail states with the characteristic energy of <i>E₀</i> =400 meV measured from <i>E_{C(SiN_x)}</i> . (c) Probability of thermal excitation from <i>E_{fund}</i> to higher energies at 300 K. (d) Differential conductivity versus energy plot for various temperatures. (e) Arrhenius plot of the conductivity using both the calculated and the measured data.	83
Figure 5.11 Temperature scan of the forward I-V characteristics of the formed a-SiN _x :H based <i>pin</i> diode D3. The temperature dependence of its conductivity through the Arrhenius plot is given in the inset.	85
Figure 5.12 Poole-Frenkel plot of ln(<i>J/F</i> ^{1/2}) versus <i>F</i> ^{1/2} for D2 after the forming process at different temperatures. V=0 intercept of the main plot versus 1000/ <i>T</i> with indicated energy depths of the trap level.	86

Figure 5.13 Poole-Frenkel plot of $\ln(J/F^{1/2})$ versus $F^{1/2}$ for D3 after the forming process at different temperatures. $V=0$ intercept of the main plot versus $1000/T$ with indicated energy depths of the trap level.	87
Figure 5.14 Fowler-Nordheim plot for the formed diode D2 using the I-V data measured at the lowest temperatures: 140 K, 160 K and 180 K. Inset shows the possible field-enhanced carrier transport mechanism.	88
Figure 5.15 Forward and reverse I-V characteristics of a-SiN _x :H based <i>pin</i> diode (D2) after the forming process. The measurement sequence and the directions of the measurements are indicated by the numbers and the dashed arrows, respectively. .	90
Figure 5.16 (a) Current versus time curve of a formed a-SiN _x :H based <i>pin</i> diode (D2) carrying out the charging/discharging moment under a forward bias of 5.05 V. (b) Forward biasing voltage versus charging/discharging time.	91
Figure 5.17 Proximity of <i>p/i</i> interface of a heterojunction <i>pin</i> diode. (a-1) Energy band diagram and (a-2) possible space charge under equilibrium. (b)-(c) Recombination and trapping phenomena at forward bias. (d) Schematical localized states and their carrier exchange with the relevant band edges. (e) Detrapping and (f) steady-state generation at reverse bias.	93
Figure 5.18 (a), (c), (e) Uncorrected and (b), (d), (f) corrected (for the PMT responsivity, appendix D) normalized EL spectra after the forming process of a-SiN _x :H based <i>pin</i> diodes (D1) having different window electrodes: Cr, Al, ITO, respectively. 95	95
Figure 5.19 Lateral propagation of the formed region along the ITO electrode of the sample with the highest emission energy (D3) followed in time from (a) to (h) with ~10 s intervals.	97
Figure 5.20 EL spectra at various temperatures for the diode D2. (a) As-measured EL data with their corresponding smoothing curves. (b) EL spectra corrected for the PMT responsivity using the smoothing curves of (a).	98
Figure 5.21 Corrected EL spectra of the formed diodes D0, D1, D2 and D3 produced with $r=0, 2, 4$ and 9 , respectively. Symbols are the data measured by the PMT and the lines are the fitted data taken with the Si photodiode. The fitting for the spectra of D0 is given in the inset.	99

Figure 5.22 The photographs of the formed diodes D1, D2 and D3 during their light emission under application of the forward bias of ~ 11 V.	100
Figure 5.23 Normalized full EL spectrum of the diode D1 measured with different photodetectors. The band around 2750 nm is the absorption due to CO ₂ molecules present in the air.	101
Figure 5.24 Normalized brightness versus current density plot of the diodes D0 and D2.	102
Figure B.1 Literature review chart of a-SiN _x :H based LEDs.	119
Figure B.2 Literature review chart of a-SiN _x :H based LEDs (continued).	120
Figure B.3 Literature review chart of a-SiN _x :H based LEDs (continued).	121
Figure B.4 Literature review chart of a-SiN _x :H based LEDs (continued).	122
Figure B.5 Literature review chart of a-SiN _x :H based LEDs (continued).	123
Figure C.1 The normalized spectral responsivities of the PMT, CCD, Si, Ge and PbS detectors.	124
Figure D.1 The schematic representation of the path followed by a ray of light incident on the air/film interface and the modifications in its intensity during its travel within the bulk of the film.	127
Figure F.1 (a) Differential conductivity of D3 versus energy measured from the conduction band edge. (b) Arrhenius plot of calculated and measured conductivity data. In the calculations, h_0^c and E_0 are taken as 7×10^{22} and 600 meV, respectively.	133

CHAPTER 1

INTRODUCTION

1.1 Review on light sources

The yearly global electricity consumption is about 30 trillion kWh, 21% of which is consumed for lighting [1–3]. Accordingly, 1% improvement of the luminous efficiency would save up to \$2 billions per year. The efficiencies of incandescence and fluorescence are not likely to be improved as the physical principles under these phenomena have already been exhausted [1]. For instance, the incandescence from a light bulb is based on the blackbody radiation of an electrically heated tungsten wire in the visible wavelengths. Contrary to the main purpose of lighting, most of the electrical energy supplied to the bulb is given out as heat. Light bulbs are still commercially available, however, they are no more the devices of choice due to their inefficient power consumption. As for a fluorescent lamp, low pressure mercury gas emits UV light via electrical excitations. The UV light is incident on the internal surface of the lamp covered with a phosphorus layer. The photoluminescence (PL) from the phosphorus layer under UV irradiance leads to the emission of visible light. Fluorescence, where the heating is almost negligible, is a much more efficient way of lighting when compared to incandescence. In consequence, fluorescent lamps, which first appeared in the market in 1930s, are today in vogue for indoor/outdoor lighting.

Another preference of lighting today is based on electroluminescence (EL), which is the direct extraction of light via radiative recombination of the artificially created electron-hole pairs (EHPs) within a semiconductor. By the end of 2008, the power efficiency of light emitting diodes (LEDs) has already reached that of the fluorescent lamps [4]. Today, LEDs are preferred in the indicators of electronic devices, car signal lights, traffic lamps and large area indoor/outdoor displays. EL, having the potential of near-unity efficiency, may be regarded as

the ultimate way of light extraction. Therefore, the next generation light sources are expected to be the electroluminescent solid-state LEDs.

EL phenomenon was first observed in 1907 during an electrical study on silicon carbide (SiC or carborundum) crystallites [5]. When a bias voltage above 10 V was applied, yellowish light was emitted from the crystallites with the intensity being directly proportional to the applied bias. At that time, the properties of the materials could not be controlled very well and no knowledge on quantum mechanics was available. Therefore, the process remained undetermined. The subject was further investigated in 1928 on whether the incandescence was the physical origin of the luminescence [6]. For this purpose, the change in the evaporation rate of a benzene droplet settled on the sample was measured before and during the luminescence. Anyhow, the experiments showed no difference in the evaporation rates. Then, it was correctly concluded that the emission source was not incandescence, but rather similar to the cold cathode rays.

The invention of the *pn* junction diodes in 1939 not only prepared the basis for bipolar junction transistors (BJTs), but also rendered high efficiency electroluminescent devices. The first *pn* junction LED, which emitted blue light with efficiency of 0.005%, was fabricated from SiC in 1969 [7]. In the early 1990s, SiC LEDs were commercially sold; however, the efficiency could not be improved beyond 0.03% due to the indirect nature of the SiC band structure [8].

In the mid-1950s, direct band GaAs was also started to be studied for *pn* junctions. In the late 1990s, III-V semiconductors of efficiencies as high as 0.2%-10% outperformed the SiC LEDs and have been regarded to be more suitable for the light extraction applications [9]. Today, GaAs, GaAsP, $(\text{Al}_x\text{Ga}_{1-x})_{0.5}\text{In}_{0.5}\text{P}$ diodes are primarily used as commercial visible LEDs. However, the fabrication of these diodes is expensive and they do not exhibit a ‘comfortable marriage’ with the conventional silicon based integrated circuit technology leading to serious limitations on the device performance.

1.2 Silicon based photonics

The complementary metal oxide semiconductor (CMOS) technology for the production of low cost very large scale integrated circuits (VLSI) or microprocessors has been developed on crystalline silicon (c-Si). Moreover, the large area electronics for the fabrication of displaying systems, solar cells and sensor arrays is based on hydrogenated amorphous silicon

(a-Si:H) thin film transistors (TFTs). Therefore, owing to its suitable electronic properties, Si is accepted to be the mature material of the electrical signal processing systems.

On the other hand, there is also the optical part of the modern technology. For instance, the global telecommunication lines have been constructed of fiber optics where the data are transmitted by the optical signals with the speed of light. In addition, the user interface of the technological devices (e.g. mobile phones, cameras, computers, televisions, etc.) is composed of light emitting optical elements driven by the Si based electronics.

Unfortunately, Si is an indirect band semiconductor whose optical properties are very poor. Therefore, the optical elements of the state-of-the-art 'optoelectronic' devices are fabricated from the direct band high-brightness III-V semiconductors queued above. These elements are integrated onto the Si based transistors by hybrid techniques (i.e. hetero-growth and flip-chip bonding) to combine the optical efficiency of the former with the electronic properties of the latter.

In the case of the direct hetero-growth, two main factors degrading the device reliability may be cited. First, the atoms of the III-V epilayer are also dopant atoms for Si, which may diffuse towards the substrate. Second, the lattice mismatch problems at the substrate/film interface result in high defect density. Consequently, this technique has not been preferred up-to-now although it promises high performance and high resolutions.

The commonly used hybrid technique is the flip-chip bonding which is the mechanical adhesion of the separately fabricated optical and electronic parts via soft metallic contacts of indium or solder bumps. However, the additional process for the production of the bumps leads to cost penalty and fabrication complexity. Moreover, these bumps are the main bottleneck on device resolutions. The dimensions of typical bumps are few micrometers, whereas the mesa structures of the pixels formed on the individual substrates by photo/electro lithography can be as small as nanometers. Then, the pixel size (pitch) of the state-of-the-art display systems is restricted to be at least few tens of micrometers. The relatively huge size of the metallic bumps also generates other problems related to performance and power consumption. In a flip-chip bonded pixel, the charge carriers spend most of their times within the metallic contacts, which delays the signal processing. Furthermore, during this travel through the contacts, the device is additionally heated due to the Joule effect.

To sum up, the hybrid approach, especially the flip-chip bonding provides the optoelectronics with practical solutions. However, pixel density, performance and power efficiency are limited. Therefore, this approach may be regarded as a temporary way for the fabrication

of the display systems. To overcome these restrictions, a CMOS compatible Si based LED technology is urgently required.

The requirement of a Si based LED is also declared for the microphotonics. The idea is similar to the replacement of the copper wires of the medium/long range telecommunication lines with the optical fibers, which enhanced the data transmission speed by a factor of $\sim 10^5$. Otherwise, the communication with electrical signals would not meet the high speed requirements due to the increasing number of the line users. Similarly, the density of transistors in a single processor doubles every two years, in agreement with the Moore's law [10]. Together with the boosted processor speeds, the exponential increase of the transistor density leads to much more power consumptions. The main source of the inefficient power usage is the copper connection wires between the cores of the processors. The problems caused by the interconnects are not only related to their length. Their architecture also gets more complex in parallel to the increasing number of metal levels which is expected to reach at least 12 by 2013 [11]. As the dimensions are reduced and the density of the interconnects is increased, some problems related to cross-talk, latency, RC coupling and RL delays are started to be pronounced. In addition, for gate length below 200 nm, the processing speed is no longer limited by the gate delay but by the wiring delay. The situation imitates the transportation problems of a fast growing city when the traffic system is not improved in accordance with the increasing number of cars. In this respect, Si based microphotonics offers a unique solution where the signals within a microprocessor would be created, modulated, transmitted and detected by Si based optical elements. Since the light waves can pass through each other without disturbing the original signal, the complications caused by the fabrication of several layers would be disposed. Actually, all the components for the Si based microphotonics have been realized except for an efficient light source [12].

The light extraction from c-Si is not an easy task because of its indirect gap nature such that the injected EHPs have very low probability of radiative recombination. Fortunately, this problem can be overcome by the production of hydrogenated amorphous or nanocrystalline silicon (a-Si:H or nc-Si:H) thin films, where the momentum conservation rule is relaxed and the radiative recombination rate is enhanced. In addition, a-Si:H based thin film technology allows very low cost deposition of LEDs over very large areas. This technology is suitable for both microphotonics and large area display systems. Consequently, the Si based thin film LEDs (TFLEDs) were fabricated by plasma enhanced chemical vapor deposition (PECVD) technique and investigated in this thesis.

1.3 Radiative recombination in amorphous semiconductors

The creation of excess charge carriers under excitation of sufficient energy is followed by their recombination either radiatively or non-radiatively. The excess charge carriers can be created in a semiconductor by several ways. In this section, their creation by photonic excitations and their radiative recombination, i.e. photoluminescence (PL), will be studied. This phenomenon is utilized in sample characterization for two main purposes:

- i) It supplies information on the density of states distribution within the forbidden gap of a semiconductor.
- ii) It gives idea on the material's potential for light emission applications.

The products of radiative recombination are photons which form the PL spectrum. On the other hand, the integrated PL intensity is reduced by the non-radiative transitions via single or multiple phonon emissions and possible Auger processes. The challenge between the radiative and non-radiative transitions decides whether a material is useful in optoelectronics applications. From the technological point of view, the former is the desired process, whereas the latter may be regarded as a loss. In order to enhance the radiative transitions beyond the non-radiative ones to a technologically acceptable level, the underlying physics needs to be well understood.

The real space wavefunctions of free electrons and holes in a crystalline semiconductor are extended throughout the whole lattice. In exchange, their momentum space wavefunctions are localized with almost zero uncertainty in the \vec{k} values. Therefore, the recombination of excess EHPs needs to obey the energy and momentum conservation rules while the information on their individual locations is ambiguous. The energy conservation is satisfied by the emission of a photon and the necessary (or excess) momentum is provided from (or released as) the lattice vibrations. In direct band photonic crystals, the energetically most favored EHPs also have the same momentum giving rise to high radiative recombination rates. In contrast, indirect band crystals are optically poor semiconductors as the lowest energy electrons and the highest energy holes are separated in the momentum space. The requirement of the absorption or emission of a suitable phonon for the momentum conservation prolongs the radiative life time of the carriers.

Rigid definitions of band structures become meaningless for amorphous semiconductors whose forbidden energy gap includes shallow (tail) and deep energy levels. The extended states are discriminated from the shallow levels by the relevant mobility edge, E_μ , such that

the charge carriers at the tail states are immobile at 0 K. Gaussian distributions of neutral and positive/negative charged deep states are located around the Fermi energy, E_F , usually obeying the defect pool model [13]. After electrons and holes are excited to the extended states of the relevant band by absorbing a photon, they start to fall through the tail states by transferring some of their energies to the phonons (see Fig. 1.1). This process is non-radiative and called thermalization. The initial thermalization steps happen very rapidly within a time interval of order 10^{-13} s [14]. As the charge carriers further lose their energies towards deeper inside the tail states, their non-radiative transitions slow down due to the exponentially decreasing density of available states. At some energy level, the life time of non-radiative transitions reach $\sim 10^{-3}$ s which is comparable to that of the radiative ones. Then, tail-to-tail radiative recombinations are favored as indicated in Fig. 1.1.

From quantum mechanical approach, the wavefunctions of the charge carriers captured by the localized states are confined in the real space and extended in the momentum space.

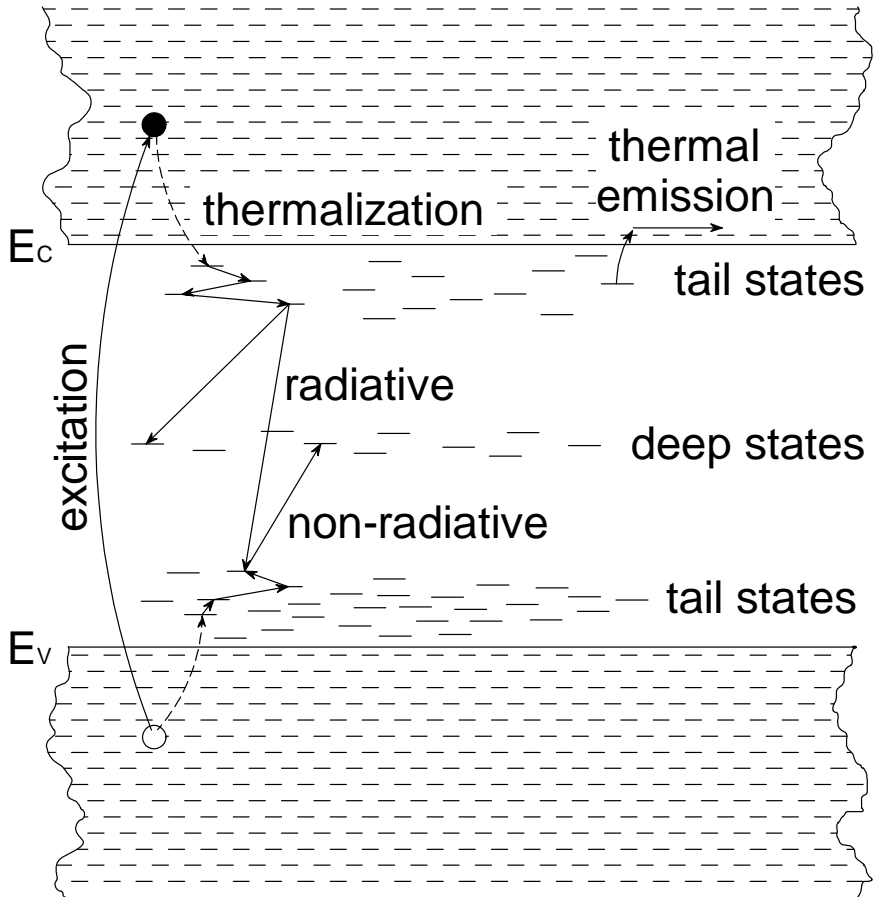


Figure 1.1: Radiative and non-radiative recombination processes of an optically excited EHP.

The huge uncertainty in the \vec{k} values releases the momentum conservation law. Therefore in amorphous semiconductors, the transition probability is determined by the spatial separation of the recombination centers. In general, the transition rate is given by the Fermi Golden Rule,

$$P = \frac{2\pi}{\hbar} M_0^2 |\langle f | i \rangle|^2 \delta(E_f - E_i \pm \hbar\omega), \quad (1.1)$$

where M_0 is a constant and $|\langle f | i \rangle|^2$ is the overlap probability of the final and initial states with energies E_f and E_i , respectively. The δ -function ensures the energy conservation by either emission (+ sign) or absorption (- sign) of a single photon. After the wavefunctions are extracted from the solution of the time independent Schrödinger equation, the overlap probability can be expressed as follows:

$$|\langle f | i \rangle|^2 \approx \exp\left(-\frac{2R}{R_0}\right), \quad (1.2)$$

where R is the distance between the localized electron and hole, and R_0 is the localization radius of the less localized state. R_0 may be roughly written as:

$$R_0 = \left(\frac{\hbar^2}{2m(E_\mu - E)} \right)^{1/2}, \quad (1.3)$$

where m is the carrier mass and E is the energy level of the trapped carrier. Then, the radiative transition rate and the radiative lifetime of the carriers are:

$$P = P_0 \exp\left(-\frac{2R}{R_0}\right) \quad (1.4)$$

$$\tau = \tau_0 \exp\left(\frac{2R}{R_0}\right).$$

Here, P_0 ($\sim 10^8 \text{ s}^{-1}$) and τ_0 ($\sim 10^{-8} \text{ s}$) are the transition rate and lifetime of completely overlapping excitonic states. For radiative recombination to occur, R should be less than a critical distance, $R_c = \frac{R_0}{2} \ln(2\pi\nu_0\tau)$, ν_0 being a typical phonon (attempt-to-escape) frequency [15]. Below R_c , the radiative transition probability between the lowest band tail states becomes superior over the non-radiative one.

The PL intensity and the shape of the PL spectrum are related to the density of band tail states according to the static disorder model [15]. As shown in Fig. 1.1, the radiative recombination occurs between the lowest band tail states, which are randomly distributed in

real space but have exponential dependence on the energy with the characteristic logarithmic slope, E_0 , usually defined as Urbach energy. The density of the deepest band tail states, available for the radiative recombination, is roughly given by [16]:

$$h^i \propto \exp\left(-\frac{E}{E_0^i}\right) \exp\left(-\frac{4}{3}\pi R_c^3 h_0^i E_0^i \exp\left(-\frac{E}{E_0^i}\right)\right), \quad (1.5)$$

where $i = c/v$ indicates conduction/valence bands, h_0 is the density of states (DOS) at the band edge and E is measured from the relevant mobility band edge, E_μ . The PL spectrum may be found from the convolution integral of h^c and h^v :

$$I_{PL}(\hbar\omega) \propto \int_{E=0}^{\infty} \exp\left(-\frac{(E_C - E) - \hbar\omega}{E_0^c}\right) \exp\left(-\frac{4}{3}\pi R_c^3 h_0^c E_0^c \exp\left(-\frac{(E_C - E) - \hbar\omega}{E_0^c}\right)\right) \exp\left(-\frac{E}{E_0^v}\right) \exp\left(-\frac{4}{3}\pi R_c^3 h_0^v E_0^v \exp\left(-\frac{E}{E_0^v}\right)\right) dE, \quad (1.6)$$

where $\hbar\omega$ is the energy difference between the conduction and valence band tail states responsible for the radiative recombination and $I_{PL}(\hbar\omega)$ is the PL intensity at a specific emission energy.

The energy difference $E_{abs} - E_{PL}$ between the maxima of the absorption (E_{abs}) and PL (E_{PL}) spectra is defined as the Stoke's shift, E_S . If the peak energy of the absorption spectrum can be imposed to coincide with the optical gap, E_{04} ; i.e. the energy at which the absorption coefficient reaches 10^4 cm^{-1} , then, the Stoke's shift becomes: $E_{04} - E_{PL}$ [17]. Taking the derivatives of Eq. 1.5 for both conduction and valence bands, equating them to zero at the energy levels between which the radiative recombination occurs and adding the final results, the following expression relating the Stoke's shift and the Urbach energy can be obtained:

$$E_{04} - E_{PL} = E_0 \ln\left(\frac{4}{3}\pi R_c^3 h_0^v E_0\right). \quad (1.7)$$

where E_0 is assumed to be dominated by the valence band tail states and may be determined by photocurrent or transmittance measurements. By this assumption, the broadness of the PL spectrum is directly related to E_0 as follows:

$$\Delta E_{PL} = \zeta E_0, \quad (1.8)$$

where ΔE_{PL} is the full width at half maximum (FWHM) of the PL spectrum and ζ is a constant between 2 and 4. ζ was numerically calculated as 2, considering the PL spectrum to be

determined mostly by the valance band tail width [18]. On the other hand, it was experimentally found as 2.6 for a-SiN_x:H alloys [17] and 3.8 for tetrahedral a-SiC:H alloys [19]. The values of $\zeta > 2$ may be qualitatively attributed to antiparallel band edge fluctuations provided that the PL excitation energy is greater than the optical gap.

In the above PL analysis, it was assumed that all the charge carriers thermalized to the band tail states recombine either radiatively or non-radiatively. However, some fraction of these carriers may be excited back to the relevant band edge after thermalization to shallow states (see Fig. 1.1). Since the mobility is enhanced within the bands, the re-excited electron and/or hole can rapidly move away, which reduces their radiative recombination probability. This re-excitation process is predicted to be thermally activated. Although the determination of a single activation energy, E_A , in a-Si:H failed, the luminescence efficiency ($y_L = p_r/(p_r + p_{nr})$ with p_r and p_{nr} being radiative and non-radiative recombination probabilities, respectively) was empirically found to obey the following rule [20]:

$$\frac{p_r}{p_{nr}} = \left(\frac{1}{y_L} - 1\right)^{-1} \propto \exp\left(-\frac{T}{T_L}\right), \quad (1.9)$$

where T_L is a parameter related to the ratio of the radiative and non-radiative recombination rates. In a-Si:H, T_L is about 25 K and it increases with alloying [14]. The temperature dependence in Eq. 1.9 comes from the exponential energy distribution of the band tail states.

At a temperature T , only the charge carriers trapped in the band tail states deeper than the energy, E_M , contribute to the radiative recombination. E_M is a temperature dependent demarcation energy, defined as $E_M(T) = kT \ln(2\pi\nu_0\tau)$, at which the thermal excitation rate equals the radiative recombination rate. The direct proportionality of E_M to T is expected since the carriers trapped at deeper states can be thermally excited to the band edges at higher temperatures. With increasing T , the PL intensity is reduced and a thermal quenching is observed. As a result, the PL efficiency can be defined by the fraction of the carriers with energies deeper than E_M . Taking into account that the band tail DOS is proportional to $\exp(-E/E_0)$, the PL quantum efficiency is written as:

$$y_L \propto \exp\left(-\frac{E_M}{E_0}\right) \propto \exp\left(-\frac{kT}{E_0} \ln(2\pi\nu_0\tau)\right). \quad (1.10)$$

In the frame of the static disorder model, Eqs. 1.5-1.10 deal with the tail-to-tail recombination characteristics of a-Si:H [16]. The PL band of a-Si:H usually gives a peak at 1.4

eV with FWHM of ~ 0.3 eV. Alloying with carbon, nitrogen and oxygen atoms shifts the PL spectra to higher energies and broadens the peak widths due to (i) larger optical band gaps, (ii) deeper band tails and (iii) higher defect density [21]. From pure a-Si:H towards its alloys, the single band character of the PL emission is preserved. Thus, the radiative recombination mechanism in a-Si:H based alloys seems to remain the same. Therefore, the above model developed for the recombinations in a-Si:H thin film can be safely adopted also for its alloys. With this conclusion, Eq. 1.10 implies that the PL efficiency should be enhanced for larger band tails at a particular high temperature, where the thermal effects dominate.

The PL technique can be used as a characterization tool for the active layer of TFLEDs since it provides information on the energy distribution and number of the luminescent centers. However, the ultimate EL spectrum depends also on the carrier injections from either side of the diode and the transport of these carriers. In the next section, the doping of a-Si:H is reviewed since the *n*-type and *p*-type doped films are grown as the electron and hole injecting layers of the TFLEDs of this work.

1.4 Doping and related defects in a-Si:H

The huge market of large area electronics has been constructed on a single and ubiquitous material, hydrogenated amorphous silicon (a-Si:H). Among its diverse applications, thin film transistors (TFTs) in active matrix liquid crystal displays (AMLCDs), image sensors and solar cells may be cited as the most important ones. The origin of this commercialization dates back to 30 years when Chittick *et al.* achieved *n*-type doping in a-Si:H for the first time [22]. They reported that the dark conductivity (σ_d) of their films deposited by the glow discharge method at various substrate temperatures ranging from room temperature to 773 K had increased from $\sim 5 \times 10^{-10} (\Omega \text{ cm})^{-1}$ to $10^{-4} (\Omega \text{ cm})^{-1}$, respectively; i.e. the activation energy of conductivity had been reduced from ~ 0.8 eV to 0.2 eV. These results proved, without doubt, that *n*-type doping of amorphous semiconductors was possible by the addition of 0.4%-4% phosphine (PH_3) to silane (SiH_4), boosting σ_d as high as 6 decades relative to its undoped value. They also recognized that the photoconductivity (σ_p) was low at room temperature deposited samples, whereas, σ_p could be enhanced for about 10^3 times under 100 mW/cm^2 illumination in the films deposited at 573 K. Another remarkable result of that work was the aging or “instability” phenomenon especially in the 473-773 K deposited films, such that the conductivity dropped down by a factor of ~ 50 in a few days - which may be regarded as the

first report on the inherent degradation in a-Si:H. The project of this group on a-Si:H was terminated at the end of 1969 by the sponsors of the research, while a group in the University of Dundee, Scotland was about to start a mission on evaporated Si [23].

After several works on the drift mobility (μ_d), DOS around E_F , and a-Si:H based field effect transistors (FETs) [24, 25], the Dundee group formulated a new strategy in 1972 with the main features of (a) both n -type and p -type doping of a-Si:H, (b) production of pn and pin junctions [26]. In 1975, Spear and LeComber published the results of the first systematic study on both n -type and p -type doping in an amorphous material [27]. Using PH_3 and diborane (B_2H_6) added to SiH_4 , σ_d of a-Si:H was improved from its intrinsic value of $\sim 10^{-9} (\Omega \text{ cm})^{-1}$ to $\sim 10^{-2} (\Omega \text{ cm})^{-1}$ in both n -type and p -type doping with respective activation energies, 0.15 eV and 0.3 eV. Their subsequent work in 1976 on the first a-Si:H based pn junction showed clear rectification [28]. Few months later, a highly photoconductive intrinsic a-Si:H was sandwiched between p and n type layers to form a pin junction solar cell with 2.4% conversion efficiency [29].

The above landmark reports created a deep impact because until then, it was theoretically predicted that doping of amorphous materials was impossible [30]. The argument follows from the overcoordinated structure of a-Si:H. In general, the silicon atom is four-fold coordinated as its electronic configuration ends with $\dots 3s^2 3p^2$. In a continuous random network (CRN) where each atom has three degrees of freedom, four-fold coordination is prohibited by the constraints attributed to the bond stretching and bending forces. The number of constraints N_C for a particular network coordination Z_n is given as [14]:

$$N_C(Z_n) = \frac{Z_n}{2} + \frac{Z_n(Z_n - 1)}{2} = \frac{Z_n^2}{2}. \quad (1.11)$$

Here, the first and the second terms stand for the bond stretching and bending, respectively. The common factor of $\frac{1}{2}$ stems from that every two atoms are connected by a single bond. The network coordination is reduced by the hydrogenation of a-Si and the average Z_n becomes:

$$Z_n = 4 - \frac{f}{1-f}, \quad (1.12)$$

where f is the hydrogen atomic concentration (i.e. $\text{Si}_{1-f}\text{H}_f$).

Good quality a-Si:H films contain hydrogen amount of at most 10% which is much less than $\sim 61\%$, required to form an ideally relaxed structure. In this overcoordinated network, it is almost impossible for the impurity atoms of phosphorus and boron to leave their lowest energy

configuration. Most of the phosphorus and boron atoms are, therefore, three-fold coordinated; only the residual small number of four-fold coordinated active donors and acceptors being responsible of doping.

Dopant atoms have lower energy four-fold coordination when they obey the 8- N rule in their charged states. For example, a negatively charged boron atom contains four valence electrons instead of the usual three. Its ideal bonding configuration becomes B_4^- with a coordination of 4. The extra charge on the boron ion is supplied by the creation of a positively charged dangling bond, Si_3^+ , around the midgap. The same argument holds also for a positively charged phosphorus atom where its excess electron is given to create a negatively charged dangling bond, Si_3^- . The following chemical reactions represent the substitutional doping of both p-type and n-type, respectively [31]:



where $U_{p,n}$ is the formation energy of ionized dopant atoms and silicon dangling bonds. These reactions may occur under thermal equilibrium during the film growth. The densities of the dopant and silicon atoms are given by the law of mass action:

$$[B_4^-] = [Si_3^+] = \sqrt{[Si_4^0][B_3^0]} \exp(-U_p/kT) \quad (1.15)$$

$$[P_4^+] = [Si_3^-] = \sqrt{[Si_4^0][P_3^0]} \exp(-U_n/kT), \quad (1.16)$$

where $[B_4^-]$ and $[P_4^+]$ are the acceptor and donor density, respectively, while $[B_3^0]$ and $[P_3^0]$ are their gas-phase concentrations. The doping efficiency is defined as the ratio of the former to the latter:

$$\xi_p = \frac{[B_4^-]}{[B_3^0]} \quad \xi_n = \frac{[P_4^+]}{[P_3^0]}. \quad (1.17)$$

The density of the four-fold active dopants and the charged dangling bonds are proportional to the square root of the gas-phase dopant concentrations (Eqs. 1.15 and 1.16). Then, the doping efficiency defined in Eq. 1.17 may be reconsidered as:

$$\xi_p = \frac{[B_3^0]^{1/2}}{[B_3^0]} = [B_3^0]^{-1/2} \quad \xi_n = \frac{[P_3^0]^{1/2}}{[P_3^0]} = [P_3^0]^{-1/2}. \quad (1.18)$$

The doping efficiency in amorphous semiconductors is low and inversely proportional to the square root of the corresponding gas-phase concentration [32]. The position of E_F is the main factor defining the doping efficiency. When E_F is around the midgap (i.e. no doping), the formation of the ionized dopant states is favored, whereas the defect creation energy is maximum. As the number of the charge compensated dopant and defect states are increased by the addition of the dopant gases, the position of E_F starts to move towards the relevant band edge. In parallel, the dopant creation energy increases and the defect creation energy is lowered [14]. In other words, as the dopant gas concentration is further increased, the defect creation becomes more favorable over the dopant formation. Therefore, E_F is prevented from reaching the extended states (i.e. metallic conductivity is never achieved). As a result, the dopant gas concentration should be at optimum level ($\sim 1\%$) to maximize the doping efficiency in amorphous semiconductors.

The doping efficiency can be enhanced if nanocrystalline silicon (nc-Si:H) structure is produced instead of the amorphous one. nc-Si:H is composed of a few nm sized nanocrystallites embedded in the amorphous tissue. This structure is obtained under the growth conditions similar to that of a-Si:H, but at higher H_2 gas dilution and RF power density [33]. The dopant atoms within the amorphous tissue are still responsible for the substitutional doping, described above. On the other hand, the dopant atoms in the nanocrystallite islands may be constrained to the four-fold configuration of Si without any defect creation, which is very similar to the doping process in c-Si. Consequently, the dopant gas concentration during the growth of the doped nc-Si:H must be kept below 1% to avoid alloying.

1.5 Hydrogenated amorphous silicon based pin diodes

The previously described doping is especially important in *pin* devices, where an intrinsic semiconductor is sandwiched between *p*- and *n*-type doped materials. The study on the I-V characteristics of these devices is motivated by their technological applications as photovoltaic cells and LEDs.

First, let us consider the energy band diagram of a-Si:H based homojunction *pin* diode in each bias condition, as shown in Fig. 1.2. After the junction is formed, the majority carriers of *p* and *n* layers (i.e. holes and electrons, respectively) diffuse through the intrinsic layer leading to a diffusion current. As a consequence, both *p* and *n* layers contain depleted space charge regions near *i* layer. That is, negative space charge is left on *p/i* region and positive

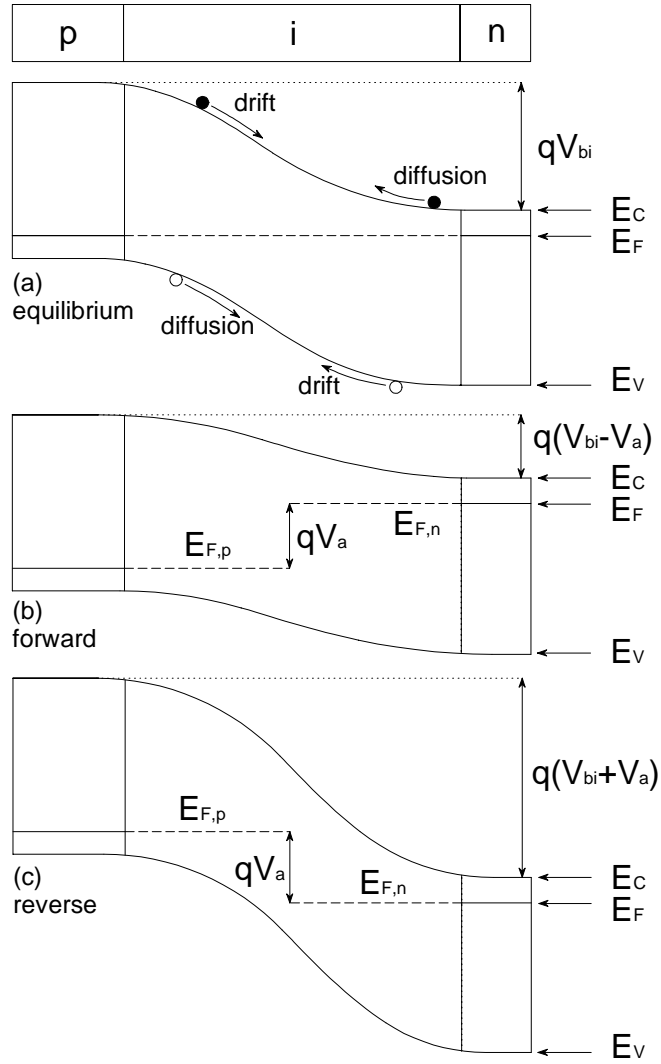


Figure 1.2: Band diagrams of a-Si:H based homojunction *pin* diode under various conditions (a) equilibrium, (b) forward bias and (c) reverse bias.

space charge is formed on *i/n* region. These depletion regions result in an electric field (F) from the positive space charge region (n layer) towards the negative space charge region (p layer). Hence, the voltage drop (i.e. built-in potential, V_{bi}) induces a drift current opposite to the diffusion current. Under thermal equilibrium, these currents balance each other and eventually, E_F is aligned along the *pin* structure (Fig. 1.2-a) [34].

When positive voltage is applied ($V_{applied}$) to the p side, i.e. forward bias, the quasi-Fermi levels ($E_{F,p}$ and $E_{F,n}$) are separated and the potential drop between the p and n layers is reduced by $V_{applied}$ (Fig. 1.2-b). Therefore, the drift current decreases and the diffusion current is enhanced. The dependence of the diffusion current on $V_{applied}$ is derived from the

minority carrier density at the depletion region boundary and may be given by [34]:

$$I = I_{r,SAT}(e^{\frac{qV}{kT}} - 1), \quad (1.19)$$

where V shortly stands for $V_{applied}$ and $I_{r,SAT}$ is the reverse saturation current. This equation does not include the recombination processes. However, for silicon based *pin* diodes, where the intrinsic carrier concentration is relatively small, the recombination current should also be considered. Then, the forward current is empirically given as [34, 35]:

$$I \propto e^{\frac{qV}{\eta kT}}, \quad (1.20)$$

where η is the ideality factor with $\eta \approx 1$ for diffusion dominant current and $\eta \approx 2$ if the recombination current dominates. If both transport mechanisms are comparable, then η takes a value between 1 and 2 [34, 35]. However, in the case of a-Si:H based *pin* diodes, this interpretation should be treated carefully. The presence of deep and shallow states causes the current transport to be dominated by recombination processes in a-Si:H intrinsic layer [36]. As found experimentally, even under the recombination dominant transport, η may decrease if dangling bond density is low and the recombination occurs via tail-to-tail states [37]. The increase in the dangling bond density enhances band-to-deep state recombination, for which η reaches 2 [35]. Therefore, any decrease in η value should not be misinterpreted as the increase in the diffusion current. Taking the above dominance of the recombination transport into account, the temperature dependence of η can be found. The related expression is derived by the integration of DOS distribution between the quasi-Fermi levels multiplied by the Shockley-Read-Hall recombination factor and is given as [36]:

$$\frac{1}{\eta} = \frac{1}{\eta_0} + \frac{T}{2T^*}, \quad (1.21)$$

where $\eta_0 = 2$, and T^* is a characteristic temperature related to the density of tail states and is typically around 1545 K for a-Si:H *pin* diode.

When negative voltage is applied to the p side, i.e. reverse bias, the quasi-Fermi levels are again separated but the potential drop between the p and n layers is now increased by $V_{applied}$ (see Fig. 1.2-c). This high potential barrier sharply decreases the diffusion current and the reverse current exponentially saturates to $I_{r,SAT}$ as it follows from Eq. 1.22. Thus, a good quality *pin* diode allows the current flow only in one direction and I_f/I_r ratio should be at least of order 10^5 at 1 V. The reverse saturation current is temperature activated as

$I_{r,SAT} \propto e^{-\frac{E_A}{kT}}$, where E_A is the activation energy [35]. For diffusion controlled transport E_A equals the energy band gap, while it is half of the gap for the recombination controlled transport.

It should be noted that in the forward bias, there is a second region at higher voltage values ($> \sim 0.8$ V), where the semi-exponential behavior of the I-V curve, given in Eq. 1.22, deviates and the current is limited by the series resistance of the sample bulk. Then, Eq. 1.22 is modified as:

$$I = I_{r,SAT} (e^{\frac{q(V-V_b)}{\eta kT}} - 1), \quad (1.22)$$

where V_b is the voltage drop across the sample bulk due to possible series resistance effects. If the resistance is ohmic, then $V_b = IR_s$, and if the current is space charge limited (SCLC), then $V_b \propto I^{1/a}$, where $a \geq 2$. Possibly, ohmic and SCLC transports can be simultaneously present.

The dependence of the I-V curves on the several parameters is demonstrated by the simulations given in Fig. 1.3. As shown in Fig. 1.3-a, the forward current at a particular voltage decreases with η increasing from 1 to 2. For the applications of *pin* diodes, η should be as low as possible to obtain the maximum output in solar cells and LEDs. However, in a-Si:H *pin* diodes, it is difficult to reduce η below ~ 1.4 [38] due to the unavoidable recombinations via dangling bonds within the forbidden gap of even good quality films. In Fig. 1.3-b, the effect of temperature (T) on the forward I-V curve is simulated, while other parameters are kept constant. With T decreasing from 440 K to 20 K, there is a shift in the I-V curve to higher voltages, especially in low level injections. This behavior stems from the decrease in $I_{r,SAT}$ together with the increase in the slope of the exponential region. The temperature dependence of η , given in Eq. 1.21, slowly attenuates the increase of this slope. The increase in E_A right shifts the I-V curve as shown in Fig. 1.3-c. Since $E_A = |E_\mu - E_F|$, the thermal emission of the charge carriers from the Fermi level to the mobility edge is more difficult at higher E_A . This is reflected in the exponential decrease of $I_{r,SAT}$ with respect to E_A . In this regard, the evenly spaced, parallel right shift of the I-V curve is expected in the semi-log plot.

The limitation of the forward current by the series resistance is simulated in Figs. 1.3-d and -e. For the ohmic series resistance, the forward current starts to deviate from the exponential dependence at a particular voltage (Fig. 1.3-d). Above this voltage, the rise of forward current is stagnated more seriously for higher R_s values. If the SCLC is the dominant transport mechanism for the voltage drop on the series resistance, the deviation of the forward current from the ideal diode curve is higher and starts at lower voltages for larger V_b exponent, a (Fig.

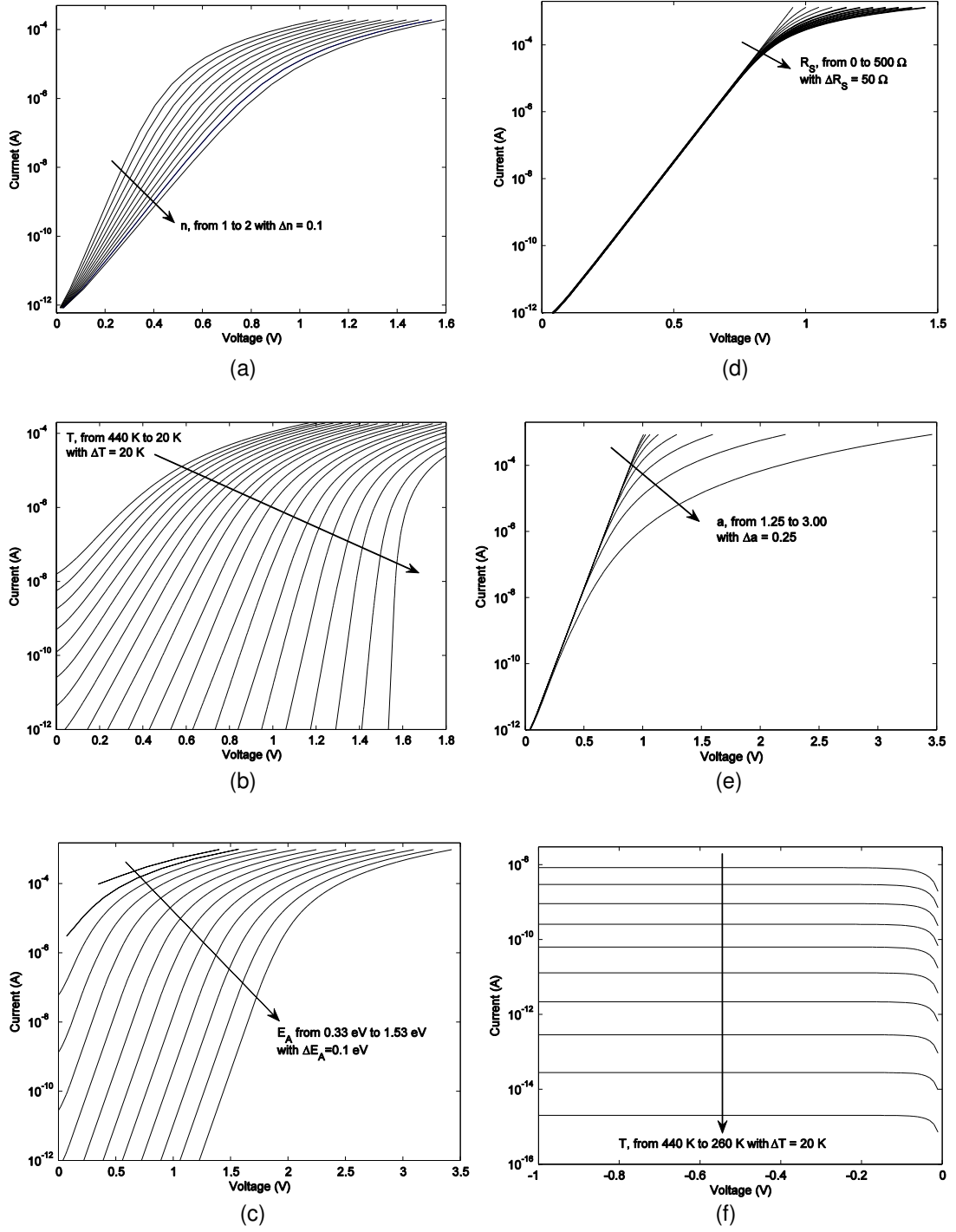


Figure 1.3: Simulation of the forward I-V curve of a *pin* diode for various (a) ideality factors, (b) temperatures ($\eta = 1.5$), (c) activation energies, (d) ohmic resistances, (e) voltage drops due to SCLC transport. In (f), the reverse I-V curve is simulated for different temperatures. Here, the parameters that are not changed in each graph are taken as $T = 300$ K, $1/\eta = 1/\eta_0 + T/(3090)$, $I_{r,SAT} = 30e^{-\frac{E_a}{kT}}$ A, $E_a = 0.83$ eV, $R_S = 25$ Ω , $V_b = 40I^{1/2}$.

1.3-e).

The reverse I-V characteristics are temperature scanned in Fig. 1.3-f. The reverse current is thermally activated, so from this temperature dependence of $I_{r,SAT}$, one can determine E_A .

1.6 Light extraction from a-SiN_x:H based diodes

In order to fabricate monolithic optoelectronic systems, Si based efficient light sources have been investigated over the decades. Indirect band of bulk c-Si and its alloys had been disgraced because of their poor optical properties. The indirect band character of these materials may be overcome by the release of the \vec{k} -selection rules at nano scales. In this respect, low dimensional Si based materials have attracted great interest. For instance, porous Si gives highly efficient PL and EL. Whereas, its poor mechanical properties avoid the fabrication of reliable LEDs with the conventional CMOS process. The short range order in the amorphous structures enhances the absorption coefficient and probably gives rise to high luminescence efficiency. Therefore, hydrogenated amorphous Si (a-Si:H) based alloys, especially silicon carbide (a-SiC_x:H) and silicon nitride (a-SiN_x:H), have also been studied for visible light sources. However, the presumed performance has not been established yet from the a-Si:H based LEDs. Another promising structure is the Si nano particles embedded in a Si oxide (SiO_x) matrix. The PL intensity obtained from the Si-in-SiO_x structure was high enough for practical LED applications [39]. On the other hand, strong enough EL has not been reported yet, mainly due to the carrier injection difficulty through the huge potential barrier of the wide gap oxide (i.e. ~9 eV). To achieve sufficiently strong EL, a lower band gap matrix, through which the carriers can tunnel easily, is indispensable. a-SiN_x:H might be a good candidate with a lower band gap of ~5 eV for efficient carrier injection, which is simultaneously wide enough for the formation of the Si-in-SiN_x quantum dot band structure for visible light emission.

a-SiN_x:H was first grown as the active layer of a *pin* TFLED by PECVD in 1993 [40]. Before the device fabrication, PL, using a sharp 365 nm Xe arc lamp as the excitation source, and optical transmittance were measured on the luminescent a-SiN_x:H layer at room temperature (300 K). The PL peak energy and optical gap of a-SiN_x:H was modified via changing the ammonia fraction in the reactant gases. Due to the poor doping efficiency of a-SiN_x:H, hydrogenated amorphous silicon carbide (a-SiC_x:H) dopant layers were deposited as the *p* side (hole source) and *n* side (electron source) of the diode (Table 1.1). The final structure of the

Table 1.1: Deposition parameters for the layers of the first a-SiN_x:H *pin* LED. After [40].

PECVD RF (13.56 MHz) power density	12.7 mW/cm ²
Substrate temperature	463 K
Total gas pressure	1.0 Torr
p-type a-SiC _x :H	CH ₄ /SiH ₄ /B ₂ H ₆ =3.5/1.5/0.03
i-type a-SiN _x :H	NH ₃ /SiH ₄ =(6-10)/(3-4)
n-type a-SiC _x :H	CH ₄ /SiH ₄ /PH ₃ =3.5/1.5/0.03
LED area	0.033-1 cm ²

diode was glass/ITO/p a-SiC_x:H/i a-SiN_x:H/n a-SiC_x:H/Al as depicted in Fig. 1.4. I-V and EL characteristics of the LEDs were measured at 300 K. The diodes, having a luminescent a-SiN_x:H of 2.5-2.9 eV band gaps, had a rectification ratio of more than 10² at about 8 V. The light emissions from the LEDs were observed when the current density exceeded ~10⁻² A/cm². Brightness (see appendix A for the details of this concept) of 0.5 cd/m² was achieved from a 0.033 cm² red LED at a current density of 2 A/cm². Besides, a power law was found between the brightness and the injected current density [41]. A semi-quantitative analysis of this behavior is provided below.

The EL emission of *pin* diodes is based on the hole injection from *p/i* side ($x=0$) and

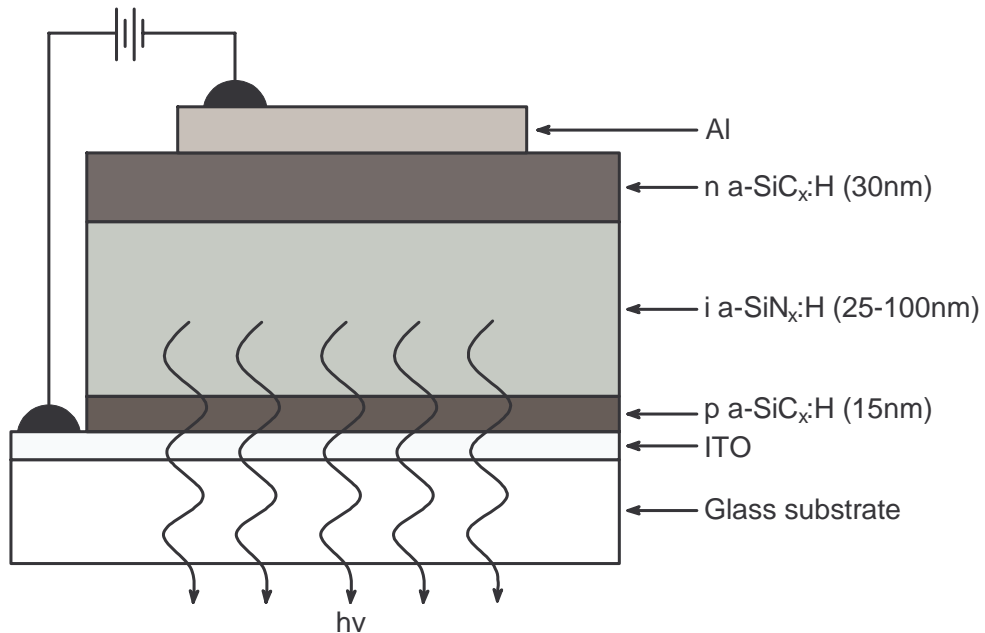


Figure 1.4: Schematic cross sectional view of the first a-SiN_x:H LED.

the electron injection from i/n side ($x=d$, where d is the intrinsic layer thickness). Their density within the luminescent active layer is related to the hole and electron currents via the continuity equation. Consider the continuity equation for the holes under uniform electric field, F :

$$\frac{\partial p(x,t)}{\partial t} = D_p \frac{\partial^2 p(x,t)}{\partial x^2} - F\mu_p \frac{\partial p(x,t)}{\partial x} + G_p - R_p, \quad (1.23)$$

where $p(x,t)$ denotes the distribution of hole density in the intrinsic layer, D_p - hole diffusion coefficient, μ_p - hole mobility, G_p - hole generation rate and R_p - hole recombination rate. It is well known that during the steady state, $\partial p(x,t)/\partial t = 0$. In parallel, assuming the intrinsic layer to be slightly n-type, all the holes should recombine with only a fraction of electrons, whose density and mobility are much higher. Besides, since the drift current dominates at high forward bias, diffusion and generation terms are neglected, i.e. $D_p \approx 0$ and $G_p \approx 0$. Thus, the above continuity equation is simplified as follows:

$$-F\mu_p \frac{\partial p(x)}{\partial x} = R_p. \quad (1.24)$$

Here, hole recombination rate can be expressed by $R_p = p(x)/\tau_p$, where τ_p is the recombination lifetime of holes. Then, Eq. 1.24 is solved for $p(x)$ and the hole density is found to decrease exponentially within the intrinsic layer:

$$p(x) = p(0) \exp\left(-\frac{x}{\mu_p \tau_p F}\right), \quad (1.25)$$

where $p(0)$ is the hole density at p/i interface and is proportional to its corresponding hole current J_p . The recombined hole density is denoted by ' $p(0) - p(x)$ ', which, at the same time, is the density of electrons that replaced the holes at the position x in the intrinsic layer. This density together with the constant density of electrons, K , which does not recombine within the intrinsic layer, results in the total electron density, $n(x) = K + p(0) - p(x)$. The constant K can be determined by the boundary condition at $x = d$:

$$\begin{aligned} n(d) = K + p(0) - p(d) &\longrightarrow K = n(d) - p(0) + p(d), \\ n(x) = n(d) - p(0) &\left(\exp\left(-\frac{x}{\mu_p \tau_p F}\right) - \exp\left(-\frac{d}{\mu_p \tau_p F}\right) \right), \end{aligned} \quad (1.26)$$

where $n(d)$ is the electron density at i/n interface and is proportional to its corresponding electron current J_n .

Since a fraction of all the recombinations lead to the radiative ones, the densities of carriers responsible for the EL intensity (or brightness) may be represented by $n(x)^{\alpha_c}$ and $p(x)^{\alpha_v}$, where α_c and α_v are parameters of the range from 0 to 1. In bimolecular recombination, $\alpha_c = \alpha_v = 1$, while in monomolecular case, the parameter corresponding to the majority carriers is zero and the other one is unity. For the recombination mechanism between the localized band tail states, these parameters corresponding to the band tail widths are smaller than unity. Since both types of carriers must be simultaneously taken into account for their radiative recombination, the brightness of EL emission may be found by their product:

$$B \propto \int_0^d n(x)^{\alpha_c} p(x)^{\alpha_v} dx. \quad (1.27)$$

To simplify this expression, the $(\mu_p \tau_p F)$ in Eq. 1.25-1.26 is assumed to be much smaller than d [41]. In other words, most of the holes recombine near p/i interface and almost all the electrons injected from n -side reach p -side. In this regard, instead of x dependent carrier densities in Eq. 1.27 one can use $n(d)^{\alpha_c}$ and $p(0)^{\alpha_v}$:

$$B \propto n(d)^{\alpha_c} p(0)^{\alpha_v}. \quad (1.28)$$

As mentioned before, these carrier densities are proportional to the electron and hole currents:

$$B \propto J_n^{\alpha_c} J_p^{\alpha_v}. \quad (1.29)$$

On the other hand, the net current, J , is proportional to $n(x) + p(x) = n(d) + p(0) \exp\left(-\frac{d}{\mu_p \tau_p F}\right)$ (from Eq. 1.25 and Eq. 1.26). As mentioned above, since the intrinsic layer is assumed to be slightly n -type, $p(0)$ is much smaller than $n(d)$. Besides, the exponential factor reduces the contribution of the hole term. Therefore, the total current is dominated by electrons, i.e. $J \approx J_n$. Taking this into account, J_n in Eq. 1.29 may be replaced by the total measured current. Also, to find the dependence of brightness on the total measured current that is affected by both α_c and α_v , Eq. 1.29 can be multiplied and divided by $J_n^{\alpha_v}$:

$$B \propto J_n^{\alpha_c} J_p^{\alpha_v} \frac{J_n^{\alpha_v}}{J_n^{\alpha_v}} = J_n^{\alpha_c + \alpha_v} \frac{J_p^{\alpha_v}}{J_n^{\alpha_v}} \approx J^{\alpha_c + \alpha_v} \frac{J_p^{\alpha_v}}{J_n^{\alpha_v}}. \quad (1.30)$$

Since the electron and hole currents at high field are found to be represented by field-enhanced current [41] or SCLC, the ratio $J_p^{\alpha_p}/J_n^{\alpha_n}$ is a constant. As a result, the brightness and the injection current are related via:

$$B \propto J^{\alpha_c + \alpha_v} = J^m \quad (1.31)$$

where the exponent $m = \alpha_c + \alpha_v$ is between 0 and 2. Now, $m = 1$ and $m = 2$ represent the monomolecular and bimolecular recombinations of EHPs, respectively; whereas other possible values correspond to tail-to-tail recombination process [40]. For example, the EL mechanism in a-SiN_x:H TFLED of [40] was claimed to be monomolecular or tail-to-tail recombination as m was found to be close to unity.

A recent literature review of the luminescent properties of PECVD grown a-SiN_x:H thin films is outlined in the form of charts in appendix B.

The brightness of PECVD grown a-SiN_x:H *pin* visible TFLEDs has been improved to 200 cd/m² at 600 mA/cm² injection current with a peak emission at 460 nm [42]. In addition, the external quantum efficiency (i.e. ξ_{ext} , see appendix A) of a few percentages has been achieved recently [43]. Although these reports are interesting, they both include additional post-deposition treatment steps, which is the main bottleneck for their application in a-Si:H based large-area optoelectronic systems. In this respect, the aim of this work is to achieve high efficiency EL from as-grown a-Si:H based TFLEDs.

1.7 Thesis outline

Chapter 2 includes the photoluminescence and other optical measurements of a-SiN_x:H thin films deposited under different NH₃/SiH₄ flow ratios.

In chapter 3, the effect of doping conditions on the optoelectronic properties of nc-Si:H thin films is analyzed to optimize *p*- and *n*-type layers for *pin* diodes.

Chapter 4 is related to electrical characteristics of homojunction *pin* diodes fabricated at different deposition conditions.

The electroluminescence and electrical characteristics of a-Si:H and a-SiN_x:H based *pin* diodes, and their formation process are presented in chapter 5. This chapter uses the optimization results of chapter 2, 3 and 4.

Finally, chapter 6 summarizes the study of this thesis on a-Si:H and a-SiN_x:H based light emitting *pin* diodes.

CHAPTER 2

ABSORPTION AND RECOMBINATION PROPERTIES OF a-SiN_x:H THIN FILMS

2.1 Introduction

Within the context of this thesis, the devices to be produced for light emission studies are p^+ nc-Si:H/*i* a-SiN_{*x*}:H/ n^+ nc-Si:H *pin* diodes. The doped p^+ and n^+ films in this trilayer structure are the hole and electron injectors, respectively; while the undoped (intrinsic) film is the so-called luminescent active layer. Before the fabrication of a *pin* LED, the physical properties of each layer must be investigated and the devices must be optimized. To start with, the optical properties of the intrinsic layer are analyzed by photoluminescence (PL) measurements to determine its light emission potential for the eventual application in LEDs. Si rich a-SiN_{*x*}:H film is a good candidate for the intrinsic layer due to its possibility of tuning the emission energy in the visible region and its lower potential barrier for the carrier injection when compared with the silicon oxide. So far, the investigations on the PL of Si rich a-SiN_{*x*}:H films have shown that the PL peak energy shifts to higher energies with increasing *x* value or $r=\text{NH}_3/\text{SiH}_4$ flow ratio [44, 45]. This increased PL peak energy is usually correlated with the quantum confinement effect (QCE) in Si quantum dots [46] or with the increased band gap, E_G , and band tail width, E_0 [47]. So, the origin of the radiative recombination in Si rich a-SiN_{*x*}:H films is still in debate.

In this chapter, after a brief optical characterization procedure of four sets of Si rich a-SiN_{*x*}:H films with different nitrogen contents, their PL results are reported in detail. Their light emission characteristics are studied in the frame of electron-phonon coupling (Stoke's shift) and static disorder (band-tail recombination) models.

2.2 Experimental details

Four sets of hydrogenated amorphous silicon nitride (a-SiN_x:H) thin films were grown by a conventional radio frequency (RF) capacitively coupled plasma system (see [48] for details) with ammonia (NH₃) to silane (SiH₄) flow ratios of $r=2, 4, 6, 9$ (see Table 2.1). Prior to the deposition, ordinary glass, quartz and silicon substrates were prepared by a standard cleaning process. After cleaning, the substrates were immediately loaded into the reactor chamber and kept under vacuum until the growth temperature of 523 K was maintained. During the film production, the power density, the chamber pressure and the total gas flow rate were set to 20 mW/cm², 0.5 Torr and 50 sccm, respectively. After the deposition, the temperature was always waited to drop below 323 K before the vacuum breaking.

Fourier transform infrared (FTIR) spectra were taken from the films deposited on high resistivity c-Si wafers ($\sim 3500 \Omega\text{cm}$) from 400 cm⁻¹ to 4000 cm⁻¹ with a resolution of 2 cm⁻¹. The transmittance was converted to the infrared absorption coefficient by taking the natural logarithm of the data and then dividing to the film thickness. The fitting of the infrared absorption peaks and their deconvolution were done using PeakFit computer program. Therefore, the main error sources in the FTIR analyses are the thickness measurements and the fitting procedure.

The optical transmittance spectra were measured on the quartz/film composite structures in the UV-visible region between 200 nm and 1100 nm (Perkin Elmer Lambda 2S spectrometer). Thickness, refractive index and absorption coefficient (α) were obtained by a computer program OptiChar where the discrepancy factors of the fits were always below 1% [49]. Thickness values were verified mechanically by a stylus profilometer by measuring the height difference between the film and the substrate through the groove masks created on the ordinary glass substrates. The optical gaps of the films (E_{04}) were determined from the energy values at which the absorption coefficient reaches 10⁴ cm⁻¹. A disorder parameter related

Table 2.1: Gas flow parameters of the a-SiN_x:H film deposition.

Film#	Gases (sccm)			$r=\text{NH}_3/\text{SiH}_4$ flow ratio
	NH ₃	SiH ₄	Total	
SN1	33	17	50	2
SN2	40	10	50	4
SN3	43	7	50	6
SN4	45	5	50	9

to the depth of the localized tail states within the forbidden optical gap, E_0 , was determined from the slope of the $\ln(\alpha\hbar\omega)$ versus $\hbar\omega$ plot.

The PL spectra of four sets of a-SiN_x:H thin films grown on highly resistive c-Si wafers were measured using the 325 nm line of a HeCd UV laser as the excitation source. The emitted light was focused on a CCD detector. The as-measured data was then corrected for the CCD responsivity, provided in appendix C.

The PL measurements were also performed at cryogenic temperatures to discriminate possible noise emissions and the actual data. For the temperature scan of the PL measurements, the sample (SN3) was placed in a closed cycle liquid He cryostat chamber (Advanced Research Systems, Inc.) as shown in Fig. 2.1. The chamber was pumped down to 1.5 mTorr and the sample temperature was maintained by the temperature controller (LakeShore 331). After passing through the band-pass filter, the 365 nm line of a Hg lamp was chopped and focused on the sample using a concave mirror (see Fig. 2.1). The emitted light was collected by a convex lens and after passing through the low-pass filter, it was focused through the 1 mm wide slit of a grating monochromator (Oriel MS 257). The light is spectrally decomposed by the grating and directed to the photomultiplier tube (PMT). Then, the detector output was amplified by a lock-in amplifier (Stanford Research Systems) which was locked to the chopper frequency of 83 Hz. The low-pass filter, grating monochromator and lock-in amplifier were controlled by a computer program (see Fig. 2.1). These PL data were also corrected by the PMT responsivity, given in appendix C.

2.3 Results and discussions

2.3.1 Optical absorption properties

The bonding configurations of a-SiN_x:H films are presented by the FTIR spectra in Fig. 2.2-a. The main peak around 830 cm⁻¹ corresponds to the Si-N stretching mode [42]. The vibration bands at 1170 cm⁻¹ and 3350 cm⁻¹ are assigned to the N-H rocking and stretching modes, respectively [50]. The peak at 660 cm⁻¹ and 2170 cm⁻¹ are attributed to the Si-H wagging and stretching bonds, respectively [50, 51]. Note that CO₂ peaks come from the changes of the sample's environment during the measurements. As can be seen in Fig. 2.2-a, the main composite peak around 830 cm⁻¹ consists of three peaks. Therefore it was deconvoluted into three Gaussian at 830 cm⁻¹, 920 cm⁻¹ and 980 cm⁻¹. Since all of these peaks are associated with Si-N bonds in different configurations [51], they were named as Si-N (ν_1 , ν_2 , ν_3).

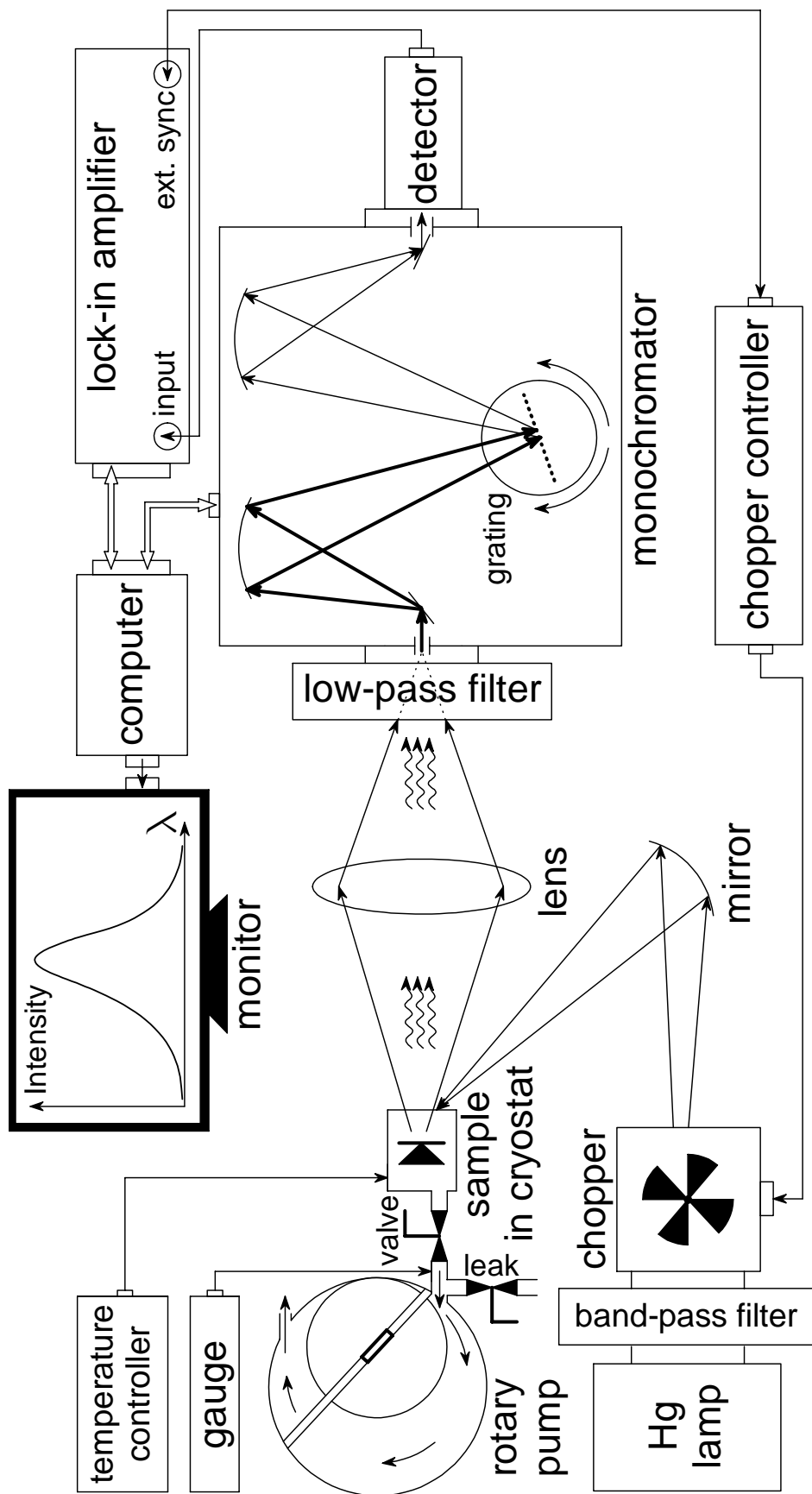


Figure 2.1: Experimental setup for the temperature-scanned PL measurements.

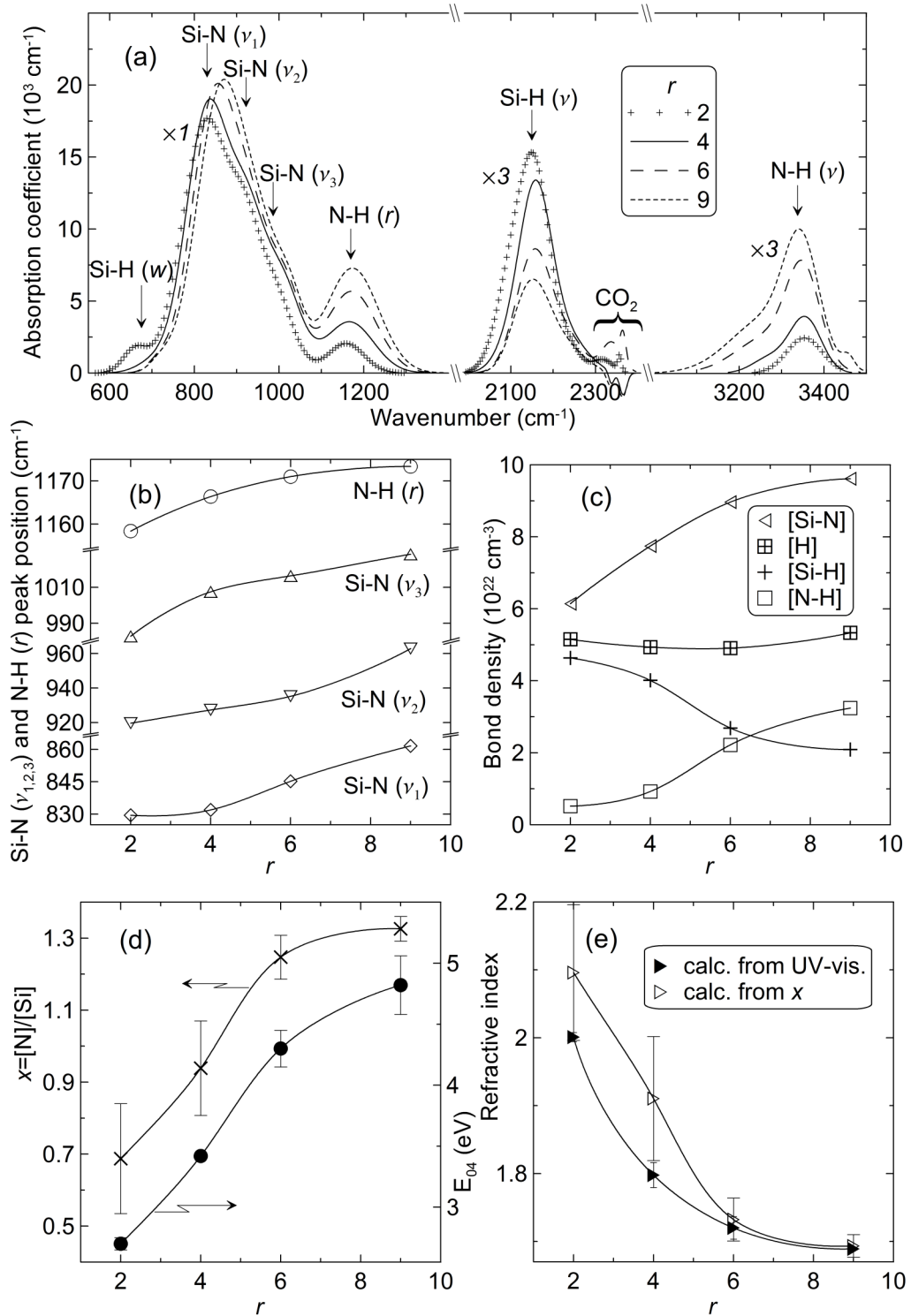


Figure 2.2: (a) FTIR spectra of $a\text{-SiN}_x\text{:H}$ films grown at different $r=\text{NH}_3/\text{SiH}_4$ flow ratios. (b) IR peak position of Si-N and N-H peaks versus r . (c) Bond densities as a function of r . (d) $[\text{N}]/[\text{Si}]$ calculated from $[\text{Si-H}]/[\text{N-H}]$ ratio and optical gap found from UV-visible spectra versus r . (e) Refractive index calculated from x and found from UV-visible spectra versus r .

As NH_3/SiH_4 flow ratio is increased, the peak positions of all Si-N deconvoluted peaks and N-H rocking peak shifted toward higher wavenumbers (see Fig. 2.2-b). In the present range of r (from 2 to 9) this shift is about 32 cm^{-1} , 43 cm^{-1} , 46 cm^{-1} and 15 cm^{-1} for Si-N (ν_1), Si-N (ν_2), Si-N (ν_3) and N-H (r), respectively. This high blueshift is associated with the increase in nitrogen content within the film with increasing r , since Si atoms become bonded to more N atoms, which have larger electronegativity than H and Si [52].

The Si-H and N-H bond densities of a- $\text{SiN}_x\text{:H}$ films were calculated from the integrated IR absorption peak areas multiplied by the corresponding calibration constants determined by Lanford *et al.* [53] (see Fig. 2.2-c). As expected, [Si-H] decreases and [N-H] increases with increasing r . Since $[\text{H}]=[\text{Si-H}]+[\text{N-H}]$ [54], the total hydrogen amount was also obtained and it shows almost no change with r (Fig. 2.2-c). Because the Si-N IR calibration constant was found previously to be dependent on the film composition [55], first, $x=[\text{N}]/[\text{Si}]$ ratio was determined. The correlation of a- $\text{SiN}_x\text{:H}$ film stoichiometry with [Si-H]/[N-H] IR bond density ratio was empirically obtained by Claassen *et al.* for a large variety of deposition conditions of plasma grown silicon-nitride layers [56] as following:

$$\frac{1}{x} = \frac{\text{Si}}{\text{N}} = 0.084 \frac{[\text{Si-H}]}{[\text{N-H}]} + 0.70. \quad (2.1)$$

Using this expression and the [Si-H] and [N-H] values shown in Fig. 2.2-c, [N]/[Si] ratio was calculated for each r as presented in Fig. 2.2-d. Afterwards, the calibration constant corresponding to each x value [55] was applied for [Si-N] computation. It was found that [Si-N] amount increases linearly when the ammonia fraction in the source gas is raised from $r=2$ to $r=4$ and further enhancement in the ammonia fraction up to $r=9$ only slightly increases [Si-N] (see Fig. 2.2-c). Consequently, the nitrogen content within the film increases and the volume fraction of Si-Si phase decreases with r . Besides, the value x increases with r from ~ 0.68 (i.e. Si rich) to ~ 1.32 (i.e. near-stoichiometry) and has similar behavior with the optical gap, E_{04} , that was obtained from UV-visible spectra (see Fig. 2.2-d). So, as anticipated, the nitrogen amount is directly responsible for the gap widening. The refractive indices found from UV-visible spectra were compared with the weighted average of the refractive indices of a-Si:H and a- $\text{Si}_3\text{N}_4\text{:H}$ media, which was related to x by [57]:

$$n(x) = \frac{n_{a-Si} + \frac{3}{4}x(2n_{a-SiN} - n_{a-Si})}{1 + \frac{3}{4}x}. \quad (2.2)$$

The refractive indices, determined through this relation with n_{a-Si} and n_{a-SiN} taken as 3.0 and 1.7, respectively, were very close to the experimental ones (from UV-visible transmittance spectra), as given in Fig. 2.2-e. Hence, x values computed from [Si-H]/[N-H] IR bond density ratio seem to be plausible.

The UV-visible transmittance spectra of a-SiN_x:H films exhibit well-behaved interference fringes in the transparent region whose maximum values always reach the transmission of the quartz substrates. This indicates that the films are fairly smooth and uniform along the PECVD electrode within at least 1 cm. The optical constants of the films are given in Table 2.2. As shown before (Fig. 2.2-d,e), the optical gap increases while the refractive index decreases with increasing r , which is consistent with the single oscillator model. If the relation $n^2 \approx \epsilon$, where ϵ is the dielectric permittivity, is assumed, the Coulomb interaction between the excess charge carriers is enhanced and their radiative lifetime is reduced. Remembering the optical gap of a-Si:H as ~ 1.8 eV and that of a-Si₃N₄:H as ~ 5 eV, all the films of this work may be considered more or less Si rich, since their optical gaps are always smaller than ~ 5 eV. On the other hand, the volume fraction of the Si rich regions seems to be reduced with increasing r , deduced from E_{04} and x dependencies on r .

During the extraction of Urbach energy values, it was found that the slope of the linear fit decreases with increasing r . As this slope is inversely proportional to the Urbach energy, the band tail width increases with r as given in Table 2.2. The Urbach tail values are much higher than those of a single phase a-Si:H film. Such wide Urbach tails of this work may stem from the dual phase character of the Si rich nitride films at hand, which comprise a-Si islands dispersed within a-SiN_x:H matrix. These islands should be size-distributed, each individual imposing its own absorption spectrum. The convolution of their absorption spectra possibly widens the overall localized band tails. As a result, instead of ‘Urbach tail’ concept the ‘subgap absorption tail’ is rather suitable for the present situation.

Table 2.2: Optical constants of a-SiN_x:H films deposited in this work.

Film#	E_{04} (eV)	Urbach tail (meV)	Refractive index	Deposition rate $\pm 5\%$ (nm/min)
SN1	2.70 ± 0.05	110 ± 10	2.00 ± 0.01	12
SN2	3.42 ± 0.02	180 ± 10	1.80 ± 0.02	21
SN3	4.30 ± 0.15	320 ± 12	1.72 ± 0.02	19
SN4	4.82 ± 0.24	340 ± 12	1.69 ± 0.01	18

2.3.2 Recombination properties by PL spectroscopy

The intensities of the PL spectra of four sets of a-SiN_x:H thin films, presented in Fig. 2.3, are comparable with each other since the measurements for each film were performed carefully and successively with the same focusing. The interference fringes are inevitable when the PL is measured from films of few hundreds of nanometers deposited on smooth surfaces. In order to correct the PL spectra roughly for the interference fringes, it was compared with the transmittance spectra taken from the same films deposited on quartz substrates. Here, the

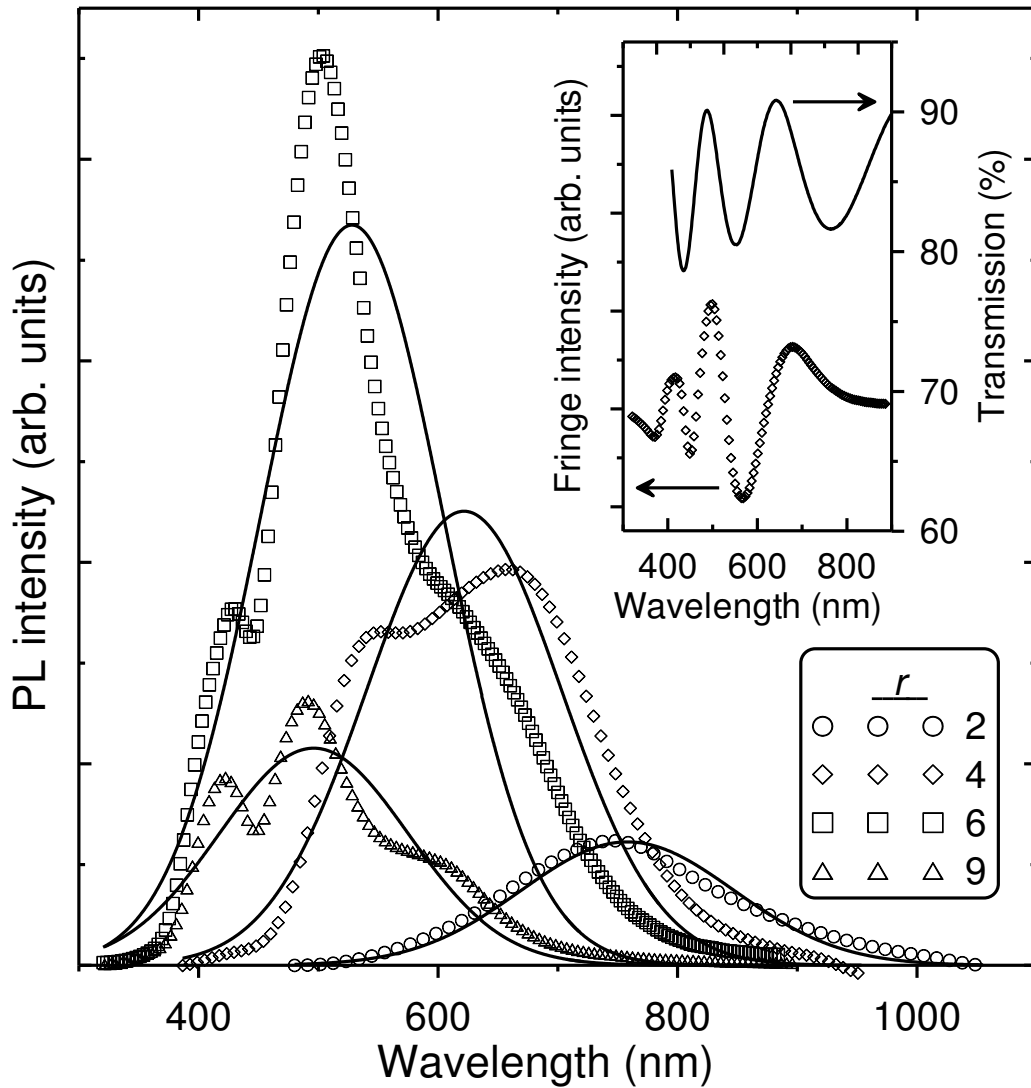


Figure 2.3: The fringing as-measured (symbols) and the fringe-free simulated (lines) PL spectra of four sets of a-SiN_x:H thin films deposited with different NH₃ to SiH₄ flow ratios. The ratio of the as-measured curve to the simulated one is given in the inset for the sample with $r = 4$. The transmittance spectrum of the same sample is provided for comparison.

deposition rates on c-Si and quartz substrates were assumed to be similar. The position and the intensity of the simulated peaks were adjusted in a way that the behavior of the $\frac{PL \text{ intensity}}{\text{simulation}}$ curves have similar fringes with those of the transmittance spectra (see inset of Fig. 2.3).

Two main results are that the PL peak wavelength blueshifts and the PL FWHM broadens with increasing r . Keeping direct proportionality between r and E_{04} in mind (Fig. 2.2-d), the blueshift of the PL band is plotted with respect to E_{04} in Fig. 2.4. In agreement with the purpose of alloying Si with N, the PL peak energy shifts from 1.6 eV (red) for $E_{04}=2.70$ eV to 2.5 eV (blue) for $E_{04}=4.82$ eV. All these emissions with their corresponding emission colors were clearly visible to the naked human eye in dark room. Fig. 2.4 also includes the dependence of the Stoke's shift, E_S , on E_{04} . It is seen that the rate of change of the Stoke's shift is higher than that of the PL peak energy. For the range of nitrogen contents in the

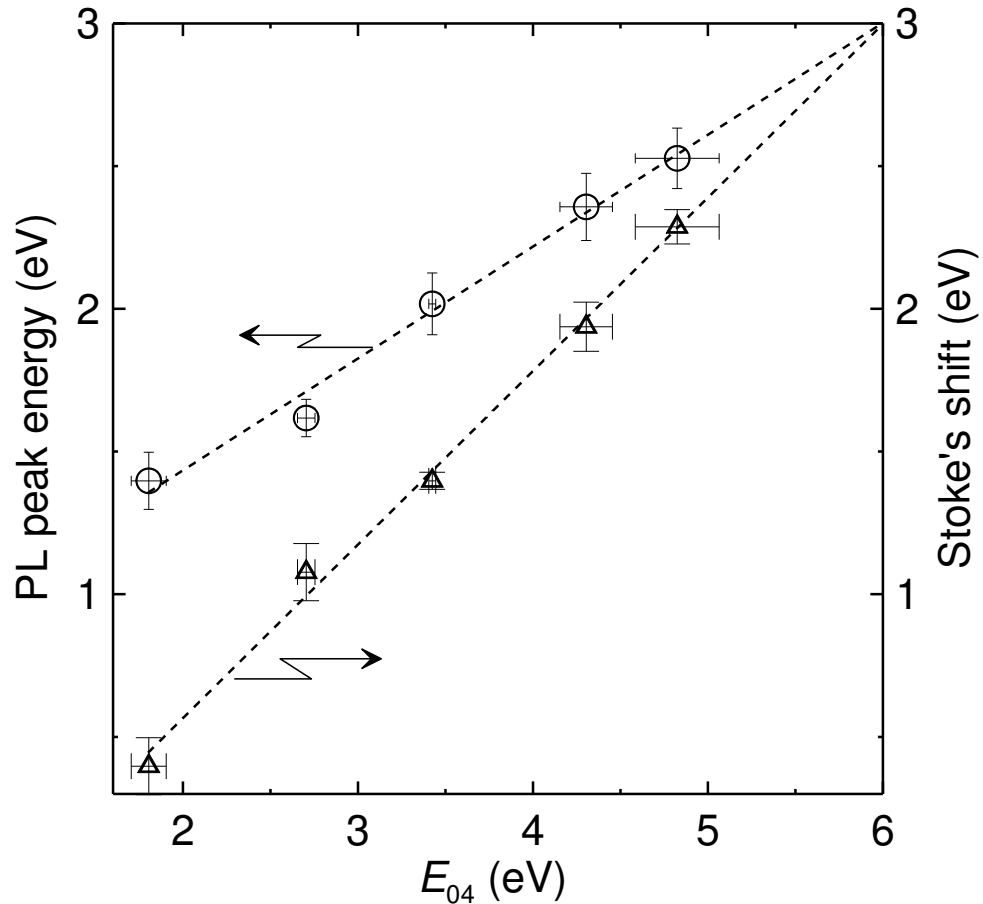


Figure 2.4: Peak wavelength of the room temperature PL of a-SiN_x:H films and Stoke's shift presented with respect to the optical gap. Data at $E_{04}=1.8$ eV correspond to the usual values for a-Si:H.

films of this work, the PL peak energy is always greater than the Stoke's shift. However, the difference $E_{PL}-E_S=0.5$ eV for SN1 reduces down to 0.2 eV for SN4. Remember that this difference for a-Si:H films is found as 1.0 eV using the widely accepted values (these values are also provided in Fig. 2.4). In this respect, while the optical gap widens with alloying, E_{PL} gets closer to the half of the optical gap. If the extrapolations of Fig. 2.4 are forced to intercept, the PL peak energy would equal the half of the gap for $E_{04}\approx 6$ eV; i.e. $E_{PL}\approx \frac{E_{04}}{2}\approx 3$ eV, corresponding to violet light emission (experimenting this hypothesis, however would require a more sophisticated set-up and may be an additional alloying atom such as oxygen). Such large Stoke's shifts are difficult to be interpreted by the electron-phonon interaction model since the electron-phonon coupling is responsible for Stoke's shift of at most 1 eV in wide gap materials [58, 59]. Instead, the following semiquantitative analysis implies that band-tail luminescence model is more successful in the interpretation of the above discussion.

In this frame, the excited carriers should, first, thermalize deep inside the gap through the band tails until the non-radiative thermalization rate becomes comparable to the radiative recombination rate. The non-radiative lifetime reaches the radiative one at some energy, below which the density of band tail states are too low for non-radiative processes to compete with the radiative transitions. For the alloys of the same kind, i.e. a-SiN_x:H here, this energy might correspond to similar density of available band tail states, h_{PL}^i with $i=c$ or v standing for the conduction or valence bands. Considering $E_0=E_0^v\approx 2E_0^c$ as usually reported for a-Si:H and its alloys [60, 61], the ratio of this band tail DOS, h_{PL}^i to the relevant band edge DOS may be roughly given as:

$$\frac{h_{PL}^c}{h_0^c} \approx \frac{h_{PL}^v}{h_0^v} \approx \exp\left[-\frac{2E_S}{3E_0}\right]. \quad (2.3)$$

Taking E_0 from Table 2.2 and E_S from Fig. 2.4, h_{PL}^c/h_0^c was calculated to be in the range 7.4×10^{-3} - 1.5×10^{-2} for different r values. In addition, this ratio can be found for a-Si:H as 1.2×10^{-2} , using $E_0\approx 60$ meV and $E_S\approx 0.4$ eV. The discrepancies, although not so serious, may arise from differences in the band edge DOS of each sample. Consequently, the radiative recombinations are favored when the carriers thermalize to the energy, at which the band tail DOS is $\sim 1\%$ of the relevant band edge DOS. Eq. 2.3 probably requires more attention for more accurate results. For instance, the assumption of similar radiative lifetimes of each sample may be wrong. However, this simple approach at least qualitatively implies a relation between E_{PL} , E_S and E_0 . It also predicts that if E_0 is further increased in parallel to E_{04} by

alloying, E_{PL} may equal $E_{04}/2$ at a specific optical gap. A more detailed analysis about the relation of PL to the electron-phonon coupling and band-tail recombination is conducted in the following.

For the crystalline semiconductors, the lattice relaxations prior to the radiative recombination of excited electron lead to an energy loss proportional to its interaction strength with phonons [14, 59]. This loss results in an energy difference between the absorption and emission band maxima of the material; i.e. Stoke's shift. In parallel, if the electron-phonon coupling is the dominant mechanism determining the PL spectrum, the PL FWHM (ΔE_{PL}) should be related to the average phonon energy ($2\pi\hbar\nu_0$) by [17, 58]:

$$(\Delta E_{PL})^2 = 8\pi \ln(2) E_S \hbar\nu_0, \quad (2.4)$$

where $E_S = E_{abs} - E_{PL}$, E_{abs} and E_{PL} being the absorption and PL peak energies; respectively. E_{abs} may be roughly taken as E_{04} , to simplify the experimental procedure.

In amorphous semiconductors, thermalization through the band tails should limit electron's freedom and attenuate the effects of phonons. Moreover, additional broadening (ΔE_{PL}^{dis}) may arise from other disorders, such as possible band edge fluctuations due to structural inhomogeneities. Thus, Eq. 2.4 may be modified as [58]:

$$(\Delta E_{PL})^2 = 8\pi \ln(2) [E_S - E_{th}] \hbar\nu_0 + (\Delta E_{PL}^{dis})^2, \quad (2.5)$$

where E_{th} is the thermalization energy. Fig. 2.5-a shows a fairly well linear relation in accordance with Eq. 2.5. The slope of the linear fit is ~ 0.5 eV corresponding to $2\pi\hbar\nu_0 \approx 180$ meV, which is much higher than a typical phonon energy of ~ 60 meV. In addition, the zero intercept of the linear fit is ~ -200 (meV)², which corresponds to a thermalization through ~ 400 meV if the disorder broadening is neglected. This value may account for both PL band width and Stoke's shift in a-Si:H. In this regard, electron-phonon interactions do not seem to be sufficient to create the observed PL spectra particularly in the wide gap amorphous Si alloys.

As briefly introduced in section 1.3, another possible mechanism to interpret the measured PL band is suggested by the static disorder model [15, 16]. In this model, the PL band shape is associated with the exponential localized states. In Fig. 2.5-b, the data of PL band width versus subgap absorption tail, E_0 was fitted by a straight line of slope ~ 2 in accordance with

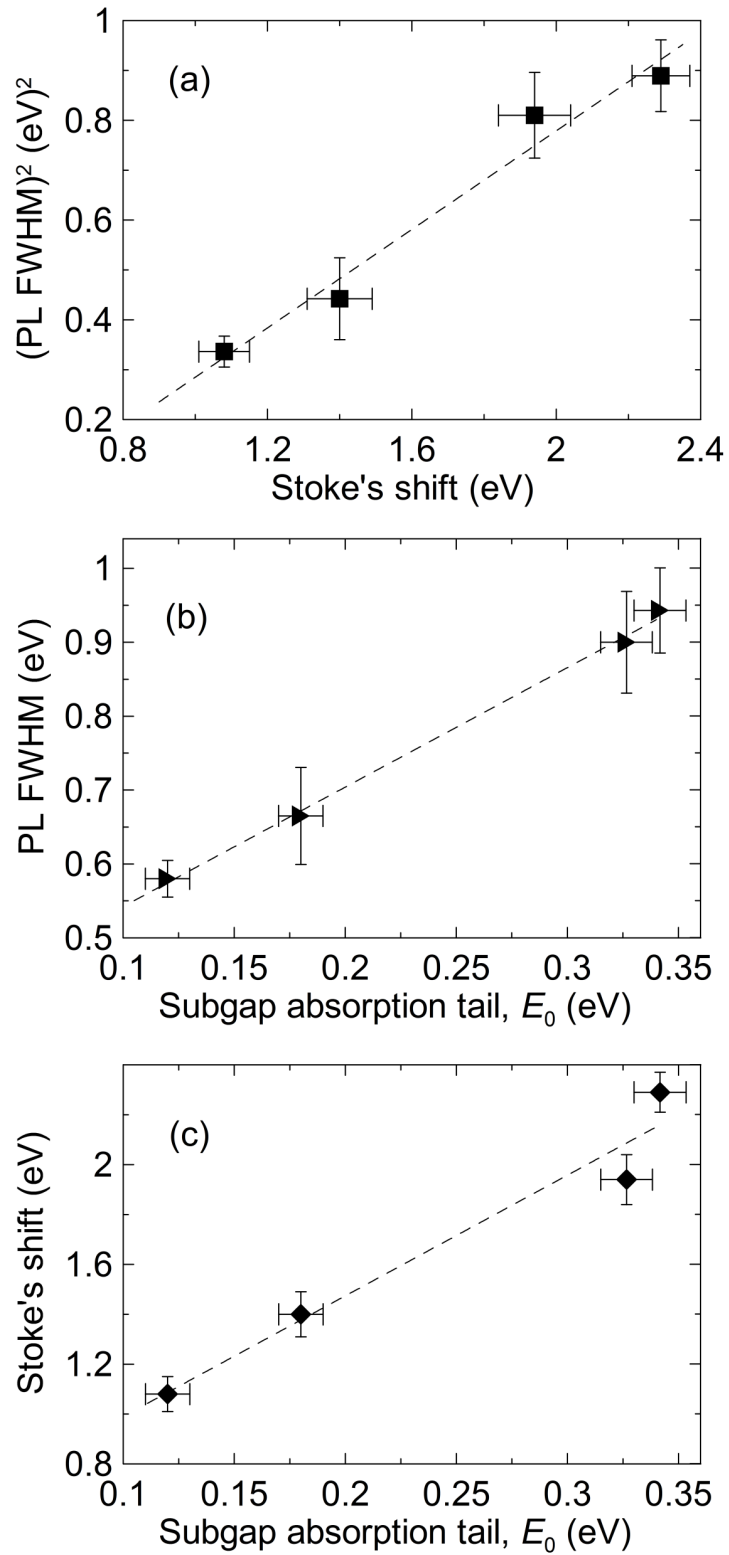


Figure 2.5: (a) Square of the PL FWHM versus Stoke's shift for the $a\text{-SiN}_x\text{:H}$ films. (b) The PL FWHM and (c) Stoke's shift plotted with respect to the subgap absorption tail.

Eq. 1.8. Although this slope is within the acceptable limit implied by the numerical calculation [18], it is slightly lower than the experimental value of 2.6, previously found for a-SiN_x:H alloys [17]. This difference is probably related to the PL excitation energy of this work. In the previous work [17] where $\zeta=2.6$, the PL excitation source had an energy of 3.4 eV, which was intentionally coincided with the optical gap of their most nitrogen rich film. In other words, the PL excitation energy was kept greater than the optical gap of each film. However, in this work, the optical gaps of the films SN3 and SN4 were 4.30 ± 0.15 eV and 4.82 ± 0.24 eV, respectively (see Table 2.2), which are above the maximum available PL excitation energy present in our laboratory, i.e. 3.82 eV. Consequently, the subgap excitation of SN3 and SN4 would prevent the recombinations between the shallower conduction and valence band tails, and would lead to PL band width smaller than expected. With this consideration, it is safe to declare that the band-tail recombination PL mechanism, concluded in the previous works on a-SiN_x:H alloys [17, 58, 62], is also valid for the films at hand. However, further blueshift of the PL peak energy from ~ 2.0 eV of the previous works [17, 58] to ~ 2.5 eV may be cited as a contribution of this work. Although it is known that subgap excitation reduces the PL FWHM and redshifts the PL band, it is worth demonstrating that blue PL can be obtained from a-SiN_x:H with higher nitrogen contents.

In the static disorder model, the main reason for the difference between the optical gap and the PL peak energy, namely the Stoke's shift, is attributed to the carrier thermalization to the lowest band tails before radiative recombination. The Stoke's shift was analytically related to the subgap absorption tail in Eq. 1.7. R_c , appeared in the logarithmic factor of this equation, depends on the energy depth of the recombination center and the radiative lifetime via Eqs. 1.3 and 1.5. While the characteristic energy depth of the localized states, E_0 , increases with alloying, R_c decreases. In parallel, alloying Si with N is known to reduce the radiative lifetime mainly due to the enhanced Coulomb interaction, which in turn decreases R_c . Moreover, h_0^v in Eq. 1.7 may also differ for samples with different nitrogen contents. Therefore, the dependence of the Stoke's shift on E_0 can not be easily determined. However, a linear dependence can be roughly expected if the effect of the logarithmic function is assumed to be minor (this argument is directly compatible with Eq. 2.3). Fig. 2.5-c exhibits this linearity. The slope of the fit is 5, which equals the logarithmic factor in Eq. 1.7 when plausible values of $E_0=200$ meV, $R_c=7$ nm [63] and $h_0^v=6\times 10^{20}$ eV⁻¹cm⁻³ are used.

2.3.3 Analyses on PL efficiency

The as-measured PL intensity can be analyzed as a function of r , but it should be corrected before its quantitative analysis due to the following reason. The excitation light incident on the film is partially reflected and partially transmitted. Some fraction of the transmitted light is absorbed by the film bulk during its travel towards the substrate. The remaining fraction of the light is partially reflected from the substrate and experiences the internal reflections within the film. This process continues until the light in the film is exhausted. Therefore, the number of photons absorbed within the film depends on the absorption coefficient at the PL excitation energy, film thickness, reflection and transmission coefficients at the air/film and film/substrate interfaces. The absorbed fraction of the incident light should be known to compare the PL efficiencies quantitatively. In this respect, the PL intensities were divided by the fraction of the absorbed intensity, which was derived in appendix D. In Fig. 2.6-a, the integrated intensity of PL spectra measured at room temperature is given with respect to r in the semilog plot after the correction procedure given in appendix D. The PL efficiency increases more than two orders of magnitude when r is increased from 2 to 6, and it saturates for greater r values. This saturation may be explained by two possible reasons. First, the optical gap 4.82 ± 0.24 eV of SN4 is above the PL excitation energy of 3.82 eV. Therefore, PL spectrum of SN4 must be regarded as a product of subgap excitations. If compared with above-gap excitations, the number of excited electrons that are candidates for radiative recombination should be smaller by a factor ~ 0.1 since the excitation energy is not sufficient for band-to-band transitions (here, the factor ~ 0.1 is the ratio of conduction band tail DOS at 3.82 eV above the valance band edge to the conduction band edge DOS). The Stoke's shift for SN4 is 2.3 eV, which means that the radiative recombinations occur well below the both band edges where the number of available band tail states is comparable to the number of excited candidate charge carriers. In this respect, the subgap excitation would have a minor role in the saturation of the PL intensity for $r > 6$. Second possibility for this saturation is predicted by Eq. 1.10. Accordingly, the PL efficiency at a particular temperature should increase with increasing E_0 and shortening τ , provided that the main PL mechanism remain the same with alloying, i.e. band tail recombination. When the nitrogen content in a-SiN_x:H is increased, both requirements on E_0 and τ are satisfied. The effect of τ might be assumed negligible since it appears in the logarithmic factor. With this assumption, the PL efficiency can be directly related to E_0 . In Fig. 2.6-b, the linear plot of E_0 versus r is supplied. The shape of the curve

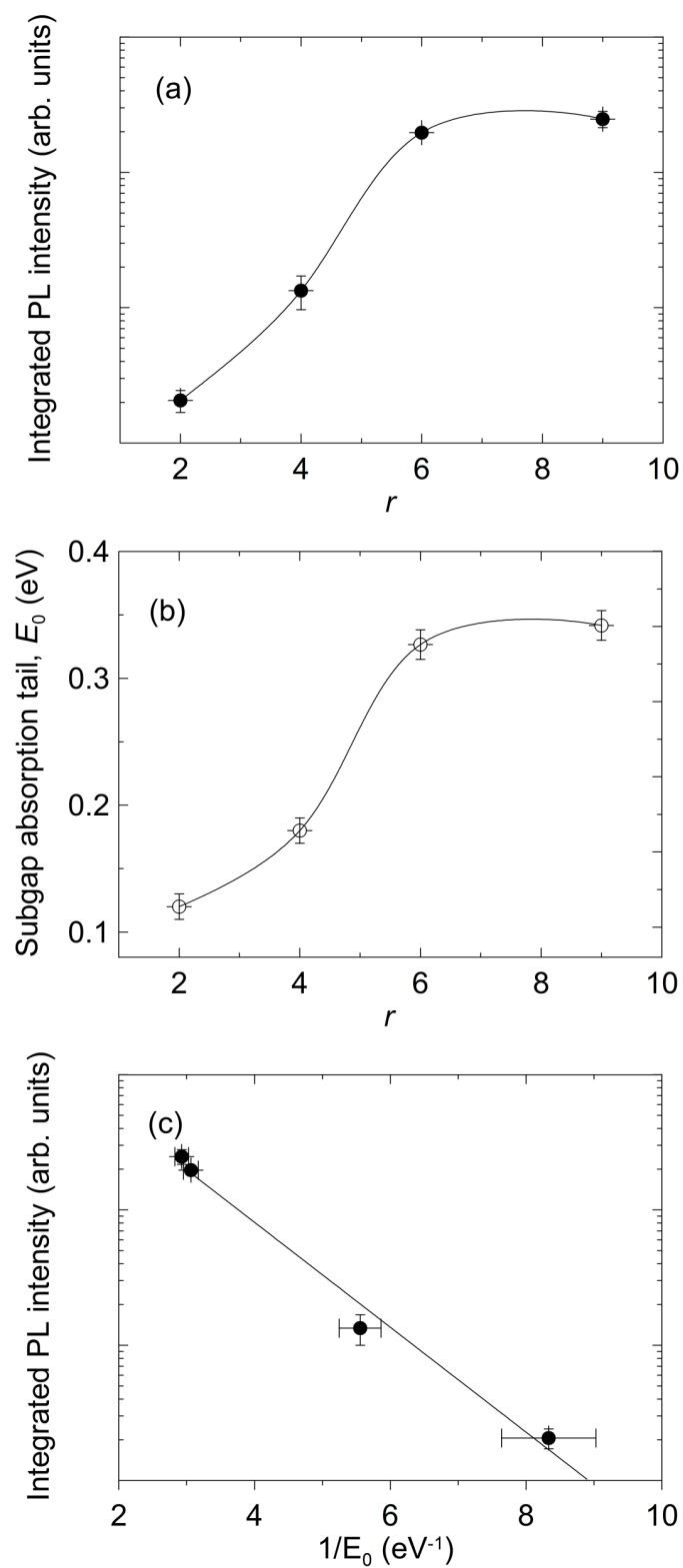


Figure 2.6: (a) Corrected PL peak area and (b) the subgap absorption tail of a-SiN_x:H films versus r . (c) Corrected PL peak area of (a) versus $1/E_0$ of (b).

resembles that of Fig. 2.6-a; the subgap absorption tail width increases almost linearly until $r=6$ and it saturates for $r>6$. This saturation may be a result of the change in the main role of nitrogen in the structure with its increasing content to form nearly stoichiometric films. For more or less Si rich samples, the nitrogen atoms break the long Si-Si chains and causes strained a-Si:H grain boundaries [58]. The volume of such distorted regions should be proportional to the nitrogen content. However, as the near-stoichiometry is reached, most of the Si-Si chains are already broken and the Si-N bonds become numerous than the Si-Si bonds. In Fig. 2.6-c, the correlation between the PL efficiency and E_0 is provided with $\ln(y_L) \propto -1/E_0$ as predicted by Eq. 1.10.

It is known that alloying a-Si:H with C, N or O for wide gap applications reduces the PL thermal quenching as a result of the deepening of the subgap absorption tail. This improvement stems from the change in the demarcation energy, E_M , which tends to move away from the relevant band edges with alloying, in parallel to the behavior of E_0 . As for a-Si_xN_x:H, increasing N content in the films increases both E_0 and the depth of E_M . Then, the thermal

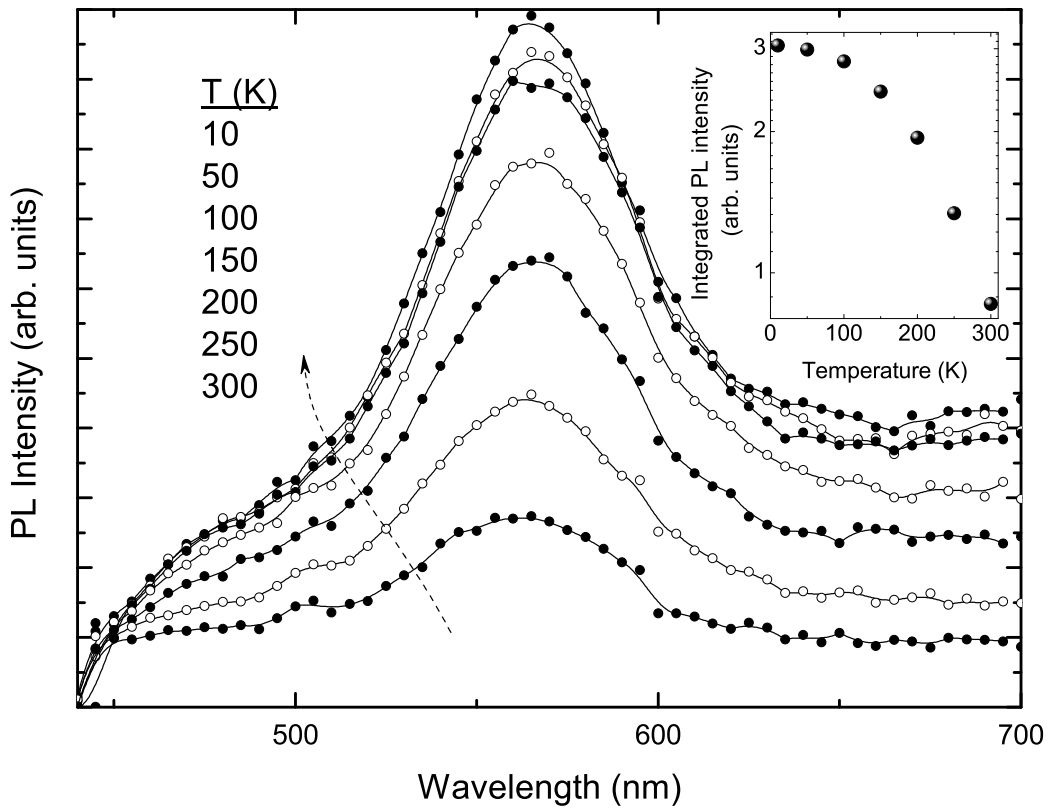


Figure 2.7: PL spectrum of SN3 film measured at different temperatures with the temperature dependence of the intensity provided in the inset.

re-emission of a charge carrier thermalized deeper through the radiative recombination centers becomes more difficult. Consequently, higher the nitrogen content, lower the thermal quenching. Otherwise, the PL temperature dependence of the a-SiN_x:H alloys used in this work are similar, therefore, it is enough to supply the temperature scan of one of the films here as a representative. In this respect, the temperature dependence of the PL spectrum of SN3 is given from 10 K to 300 K in Fig. 2.7. The PL peak energy and the PL band shape do not change with temperature. The slight redshift of the peak energy, when compared with the peak of SN3 in Fig. 2.3, arises from the difference between the PL excitation energies used in each experiment: temperature scan of the PL spectrum was performed using 3.4 eV band of a Hg lamp. The intensity distribution of the interference fringes was re-arranged accordingly. In comparison to the many orders of magnitude thermal quenching of pure a-Si:H [62], about 3-fold quenching of PL intensity observed for SN3 should not be surprising since $E_0=310$ meV of SN3 is much larger than $E_0\approx 60$ meV of a-Si:H.

2.4 Conclusion

The a-SiN_x:H films of this work were determined to be Si rich until $r=\text{NH}_3/\text{SiH}_4$ gas flow ratio reaches 9. For $r=9$, the films were nearly stoichiometric. The behavior of the optical gap, increasing from 2.70 eV for $r=2$ to 4.82 eV for $r=9$, was shown to be directly related to that of x , increasing from 0.68 to 1.32.

The PL light emissions from all the samples were easily perceivable at dark room conditions and at room temperature by the naked eye. The PL peak energy blueshifts and the PL FWHM broadens when the nitrogen content within the film is increased. The relation between the PL peak energy with respect to the optical gap was found as linear. In addition, the optical gap dependence of the Stoke's shift was also linear with a higher slope. From the intersection of these linear fits, it was concluded that the PL peak energy may reach even half of the optical gap if r is further increased. This behavior was correlated to the deepening of the subgap absorption tail with alloying. In this frame, it was shown by a semiquantitative approach that the radiative transitions are favored as the carriers thermalize to the energy at which the band tail DOS is about 1% of the relevant band edge DOS. More detailed analyses indicated that the Stoke's shift and the PL band broadening are difficult to be explained by the electron-phonon interactions, but they are rather related to the carrier thermalization deep through the band tails prior to radiative recombination.

In order to compare the PL intensities of samples having different optical constants, a simple method was introduced to correct the PL intensities for the absorbed light fraction of the PL excitation source. After the correction procedure, the PL efficiency was verified to increase exponentially as the subgap absorption tail gets wider, in agreement with the static disorder model. The thermal quenching of the PL efficiency is also reduced with alloying: only a 3-fold reduction in PL intensity is presented for the film grown with $r=6$. In comparison to a pure a-Si:H film, such low thermal quenching in the amorphous films of this work is another indicator of the band tail recombination mechanism.

CHAPTER 3

DOPING OF HYDROGENATED NANOCRYSTALLINE SILICON

3.1 Introduction

The previous chapter deals with the photoluminescence study on hydrogenated amorphous silicon nitride (a-SiN_x:H) alloys. Since the light output of these films spans the whole visible region of the spectrum and the emission intensity is high enough to be seen by naked eye, a-SiN_x:H alloys have the potential of fabrication as silicon based high efficiency thin film light emitting diodes (TFLEDs).

The working principle of a TFLED is based on the injection of electrons and holes from either side of the diode and their radiative recombination within the luminescent active layer. The most efficient way of the opposite charge carrier injections is to sandwich the active layer between *p*- and *n*-type materials. In this purpose, the deposition of highly conductive doped layers is indispensable. However, the doping efficiency of amorphous silicon is very low since high doping concentrations induce high defect density around the midgap and the doping efficiency decreases with increasing dopant gas flow rate. Consequently, the resistivity of doped a-Si:H cannot be lowered below $\sim 10^3$ Ωcm. Instead, use of high hydrogen dilution at high power regimes during PECVD process suggests a solution. During the film growth under excess hydrogen, the surface dangling bonds are saturated by hydrogen [64]. Then, since the plasma radicals have more time to survey for their ideal sites, the structural ordering is assisted. Hydrogen ions also preferentially etch away disordered and weak bonds [65]. As it is more difficult to break stable bonds, crystalline phase is rather promoted. In this regard, excess hydrogen in the reactant gas induces the formation of nanocrystalline islands dispersed randomly throughout the whole amorphous tissue.

These nanocrystallites are also distributed in size, each having its own optical absorption spectrum. Although the overall structure is more ordered when compared to the low-hydrogen amorphous counterpart, the subgap absorption tail, E_0 (a disorder parameter) of hydrogenated nanocrystalline silicon (nc-Si:H) is usually wider probably due to the convolution of the absorption spectra of all nanocrystallites. In this regard, $E_0 > 150$ meV in highly hydrogen diluted films simply implies crystallization [33].

The doping mechanism within the nanocrystalline islands should be similar to that within a single crystal bulk Si, such that the neutral dopant atoms may be forced by the lattice to have 4-fold configuration. In this case, the defect creation process experienced in substitutional doping of a-Si:H is eliminated. On the other hand, since a-Si:H is present in nc-Si:H as a surrounding matrix of the crystallites, the defect creation assisted doping would still work. Consequently, the doping efficiency would be only partially enhanced.

The light emission originated within the luminescent active region of *pin* diode needs to pass through the doped top layer and the window electrode before reaching the target, i.e. human eye, detector, etc. Therefore, the films deposited above the intrinsic layer should be transparent to the output light. The doped bottom layer is also preferred to be transparent to the emitted light for efficient back-reflection from the bottom electrode. In this regard, the optical gap of the doped layers must be wider than a critical value. For visible TFLEDs, this value has to be larger than ~ 2 eV corresponding to orange, which means that at least half of the emitted light intensity of energy greater than ~ 2 eV would be re-absorbed by the doped layers. The desired optical gap for the doped layers is about ~ 2.3 eV corresponding to green color. However, it is not an easy task to deposit amorphous silicon based highly conductive films having optical gaps above ~ 2 eV, since the doping efficiency decreases with alloying. As a solution, the band gap of nc-Si:H can be increased to as much as ~ 2.2 eV, since the eventual void formation enhances the quantum confinement effect (QCE) [33]. If high enough doping efficiency can be achieved, the use of doped nc-Si:H carrier injection layers seems to be a good idea. In addition, the doped layers may be deposited thin enough to reduce the re-absorbed light fraction further. On the other hand, since the first few tens of nanometers are known to be in highly disordered amorphous phase, the doping efficiency is very low in the films deposited thinner than ~ 50 nm [66]. Therefore, the deposition of highly conductive doped nc-Si:H films of optical gaps ≥ 2 eV and thicknesses $\gtrsim 50$ nm may be aimed for visible TFLED applications.

This work focuses on the optimization of *p*-type doping conditions of nc-Si:H. It was

assumed and experimentally verified that once the optimum conditions for p -type doping is obtained, the corresponding n -type doping would be achieved by replacing diborane with phosphine in the source gas since the n -type doping efficiency is higher.

3.2 Experimental details

Nine sets of p -type nc-Si:H were grown on glass substrates in the PECVD system with the deposition parameters summarized in Table 3.1. One can follow the time order in which the parameters were changed systematically. To study also the large area film uniformity, the films were deposited on the ‘center’ and on the ‘edge’ of the circular PECVD system, whose gas supply was located at the central region of the top electrode [33,67].

I-V characteristics of p -type nc-Si:H were measured by the computer controlled electrometer (Keithley 617) with the use of Al planar electrodes thermally evaporated above glass/film structures. The dark resistivities were obtained from the ohmic region of the corresponding I-V curves.

UV-visible transmittance spectra were measured by Perkin Elmer Lambda 2S spectrometer from glass/film composites in 200-1100 nm region. The values of optical gap, E_{04} and subgap absorption tail, E_0 were derived from these spectra by the procedure described in chapter 2.

Table 3.1: Deposition parameters and the corresponding dark resistivities of p -type nc-Si:H films at the center and near the edge of the reactor bottom electrode. During all deposition processes, the substrate temperature was maintained at 473 K.

Film#	Pressure (Torr)	B ₂ H ₆ /SiH ₄ (%)	RF power density (mW/cm ²)	ρ (Ω cm)	
				center	edge
p1	1	1.00	200	4.5×10^8	8.0×10^0
p2	2	1.00	200	1.6×10^6	6.3×10^3
p3	0.5	1.00	200	3.5×10^6	4.0×10^6
p4	1.5	1.00	200	7.1×10^6	2.4×10^3
p5	1	0.34	200	4.4×10^6	7.2×10^1
p6	1	0.17	200	3.2×10^3	1.4×10^2
p7	1	0.17	300	3.1×10^8	1.3×10^3
p8	1	0.17	160	1.2×10^3	2.6×10^1
p9	1	0.17	100	1.3×10^7	1.5×10^2

3.3 Results and discussions

The resulting dark resistivities of *p*-type nc-Si:H films are provided in Table 3.1. The change of dark resistivity with respect to the deposition parameters are plotted in Fig. 3.1 to see the tendency better. In all sets of the films, the doping efficiency is always greater at the edge of the electrode. This is consistent with our recent results [33], where the crystallinity of the films was found to increase towards the electrode edge. However, some of the films possess high degrees of nonuniformities in the dark resistivity. For instance, in the sets p1-p4, in which the effects of the pressure on the film properties were studied, the doping efficiency difference between the films grown at the center and at the edge is more than 7 orders for p1 (Fig. 3.1-a). Although the resistivity of p1 is as low as 8 Ωcm at the edge, it increases up to 4.5×10^8 Ωcm at the center. In the subsequent depositions, the resistivity of the central films could be reduced only by 2 orders. On the other hand, the resistivity of the edge films increased by 6 orders for lower pressure and by 3 orders for higher pressures (Fig. 3.1-a). In this respect, 1 Torr seems to be the optimum deposition pressure if other parameters can be adjusted to improve the doping efficiency at the center of the electrode without worsening that at the edge.

Keeping the pressure at 1 Torr, the diborane to silane flow ratio (B_2H_6/SiH_4) was reduced from 1% to 0.34% and then to 0.17% in the sets p1, p5 and p6, respectively (see Table 3.1). In contrast to a slight decrease of 1 order in the doping efficiency of the samples deposited at the edge, that of the samples at the center was gradually improved by more than 5 orders with decreasing B_2H_6/SiH_4 (Fig. 3.1-b). In parallel, the nonuniformity in the resistivity decreases from almost 8 orders to about 1 order. The B_2H_6/SiH_4 flow ratio of 0.17% (corresponding to the lowest possible diborane flow rate in the present system) may be considered as the optimum value for both fair uniformity and low resistivity. Note that this value is about 1 order of magnitude lower than the usual flow ratio (~1%) used in the doping of a-Si:H [27]. This difference may stem from the fact that the doping mechanism in nc-Si:H is mainly the activation of the dopant atoms within the nanocrystallites instead of the defect creation assisted doping of a-Si:H.

It was studied in our previous work on boron nitride (BN) [67] that the decomposition rate of diborane in the plasma was high to cause serious nonuniformities in the physical/chemical properties of the grown films. For example, the boron content of the films deposited at the center was always greater than that of the films deposited at the edge. In consequence, the

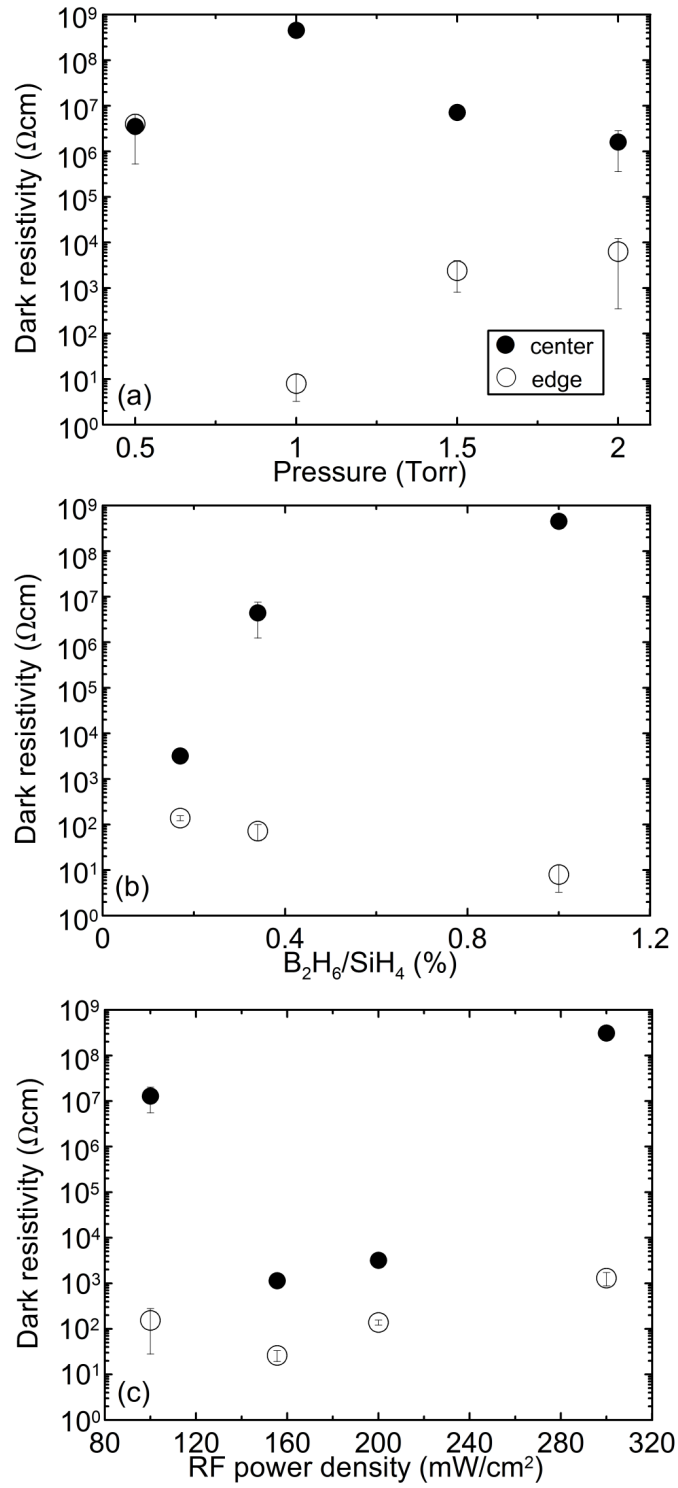


Figure 3.1: Dark resistivity of *p*-type nc-Si:H films versus (a) pressure, where RF power density is 200 mW/cm^2 and $\text{B}_2\text{H}_6/\text{SiH}_4$ is 1.00%, (b) $\text{B}_2\text{H}_6/\text{SiH}_4$, where RF power density is 200 mW/cm^2 and gas pressure is 1 Torr, (c) RF plasma power density, where the pressure is 1 Torr and $\text{B}_2\text{H}_6/\text{SiH}_4$ is 0.17%.

optical gap and the structural ordering gradually increased towards the edge of the reactor electrode. Since the diborane flow rate used within the frame of this thesis is much lower than that used in the previous work, the possible boron related nonuniformities are not likely to be detectable by the optical measurement methods, such as UV-visible and FTIR spectroscopies. However, it is known that the dark resistivity of the films is very sensitive to the flow rate of the dopant gas [27]. In this regard, the high resistivity of the central films should be related to the boron plasma species rather concentrated around the center of the PECVD electrode. At higher B_2H_6/SiH_4 flow ratio, most of the diborane seems to be decomposed as it enters the plasma leading to a high defect density film at the center of the reactor. In this region, the films may be more properly defined as an alloy. Possibly, high B_2H_6 concentration may decrease the crystallinity and form electrically inactive B-H-Si complexes [68] in the films at the center of the electrode. The residual fraction of diborane should be deposited towards the electrode edge, where its low concentration does not affect the film crystallinity and results in highly conductive p-type nc-Si:H films.

Finally, keeping the pressure at 1 Torr and B_2H_6/SiH_4 flow ratio at 0.17%, the RF power density of deposition was surveyed to check if it is possible to reduce the dark resistivity further. The first attempt as increasing the power density from 200 mW/cm^2 for the set p6 to 300 mW/cm^2 for p7 increased the resistivity by 5 orders in the central films and by 1 order in the edge films. In the sets p8 and p9, the power density was decreased down to 160 mW/cm^2 and 100 mW/cm^2 , respectively. In p8, the optimum resistivity was obtained with the nonuniformity along the reactor being lowered to 2 orders.

After determination of the optimum pressure and B_2H_6/SiH_4 flow ratio, the optical constants of the films were also followed during the power density scan. As can be seen from Fig. 3.2-a, E_{04} is above 2 eV for all power regimes. The highest optical gap values were achieved at 300 mW/cm^2 , but these films exhibit very high resistivity (see Fig. 3.1-c). Therefore, the use of RF power density of 160 mW/cm^2 is rather preferred, since these films are highly conductive and at the same time, their optical gap is suitable as a window for the output light. On the other hand, the subgap absorption tail behavior with power density is correlated with that of the resistivity (see Fig. 3.2-b and Fig. 3.1-c, respectively). The increase of E_0 was previously found to be associated to the crystallinity improvement [33]. Therefore, the lower resistivities obtained for the films with $E_0 \geq 0.17$ eV seem to be due to the increased nanocrystalline volume fraction, as it was implied above.

As a result, the optimum power, pressure and B_2H_6/SiH_4 , that yield low resistivity and

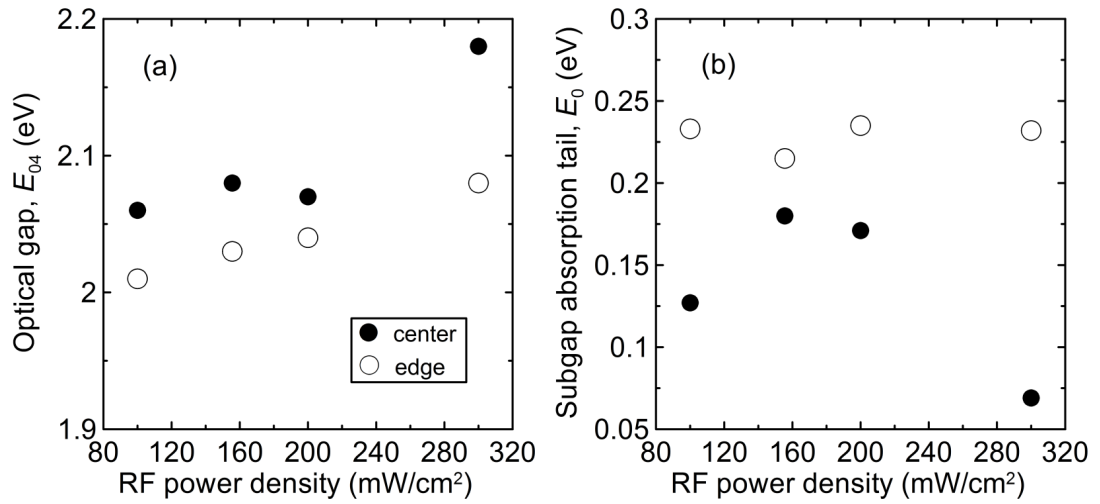


Figure 3.2: (a) Optical gap, E_{04} and (b) subgap absorption tail, E_0 of *p*-type nc-Si:H films as a function of RF plasma power density, where the deposition pressure is 1 Torr and B_2H_6/SiH_4 is 0.17%.

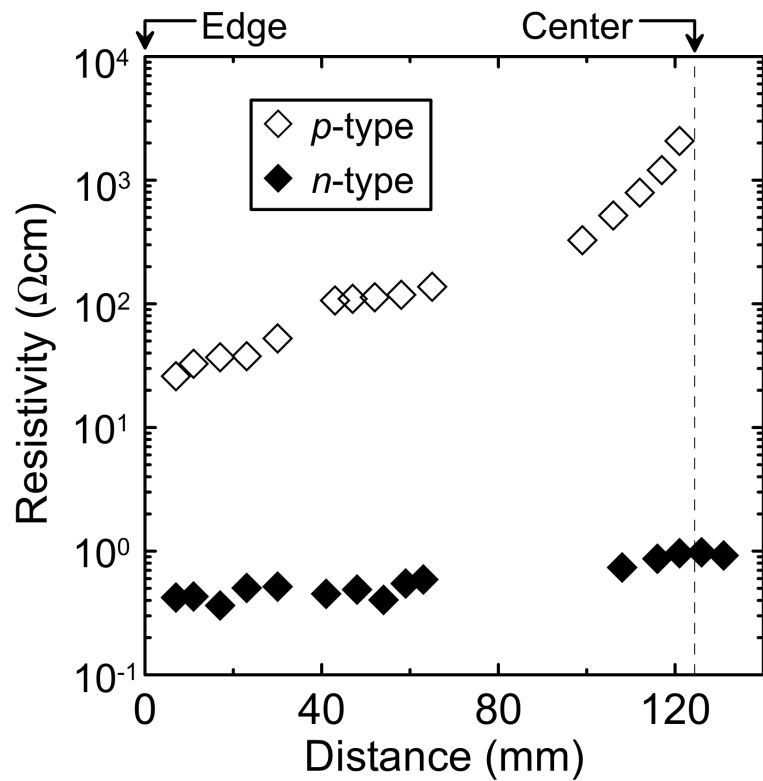


Figure 3.3: Distribution of dark resistivity along the reactor electrode of the film p8 and the corresponding *n*-type film grown using phosphine instead of diborane.

fair uniformity, were determined to be 160 mW/cm², 1 Torr and 0.17%, respectively. The *n*-type nc-Si:H films were grown under these optimized conditions by only replacing PH₃ for the dopant gas. The recent work on the dependence of dark resistivity of *n*-type nc-Si:H films on the RF power density, reported in [66], supported that 160 mW/cm² grown samples exhibit the highest conductivity. Therefore, for both *p*- and *n*-type nc-Si:H films, used in this study, the optimized growth parameters are the same, except for the dopant gases.

The uniformity of the *p*-type film grown via the optimized conditions and that of the corresponding *n*-type film are given in Fig. 3.3. The dark resistivity of the *p*-type film is below 1.5×10² Ωcm until 80 mm from the edge of the electrode while it exceeds 10³ Ωcm within the 40 mm central radius of the reactor. The resistivity of the *n*-type film is around 0.5 Ωcm and can be assumed to be uniform along the reactor. Since the only difference between these two depositions is the type of the doping gas, the nonuniformity in the resistivity of the *p*-type film along the reactor should be related to the above discussed nonuniformity in the boron concentration within the plasma.

3.4 Conclusion

The *p*-type doping parameters of nc-Si:H were optimized by a systematic study. Gas pressure, diborane to silane flow ratio and plasma power were scanned to obtain low dark resistivity, large band gap energy and good film uniformity along the reactor. The lowest dark resistivity of the films is 8 Ωcm with a large nonuniformity. But, when the optimum deposition parameters are used, they yield fairly uniform films with dark resistivity in the order of 10¹-10³ Ωcm and optical band gap energy above 2 eV. The resistivity values decrease with increasing subgap absorption tail, implying that the nanocrystallinity improvement enhances the doping efficiency. The *n*-type nc-Si:H deposited using phosphine instead of diborane with the same optimized growth conditions, exhibits dark resistivity of as low as 0.5 Ωcm. In the following chapter, *pin* diodes were fabricated with these doped layers and *p*-type layer was further optimized for better *pin* junction I-V characteristics.

CHAPTER 4

FABRICATION OF HYDROGENATED AMORPHOUS SILICON HOMOJUNCTION PIN DIODE

4.1 Introduction

After the optimization procedure of the doped layers in chapter 3, the quality of the junction formation was tested via the fabrication of *pin* diodes using a-Si:H film as the intrinsic layer. In this chapter, the B₂H₆/SiH₄ flow ratio of *p*⁺ nc-Si:H layer deposited during the *pin* production was again optimized for better diode characteristics. The rest of the optimizations was done by changing the intrinsic layer (a-Si:H) growth conditions, such as PECVD chamber pressure and hydrogen dilution. It was found that these intrinsic layer deposition parameters strongly affected the *pin* diode I-V characteristics. The optimized *pin* device was analyzed by temperature scanned I-V and constant photocurrent measurements (CPM). The I-V curves and CPM were used to compute the energy distribution of density of states (DOS). The results were compared with those of the device-grade intrinsic a-Si:H film.

4.2 Experimental details

Five a-Si:H based homojunction *pin* diode sets were deposited on Cr coated glass substrates, each produced in a single PECVD cycle. The fabrication steps are demonstrated in Fig. 4.1: first, the glass substrates were cleaned by a standard cleaning procedure and placed in the e-beam evaporation system for Cr coating. After the deposition of 100 nm Cr bottom contact, the Cr coated glass substrates were stocked in a dust- and mild-free case to be used when necessary. For the growth of *p*, *i* and *n* layers, the glass/Cr structure was gently submerged into alcohol and then rinsed in deionized water. After they were dried with a nitrogen gun,

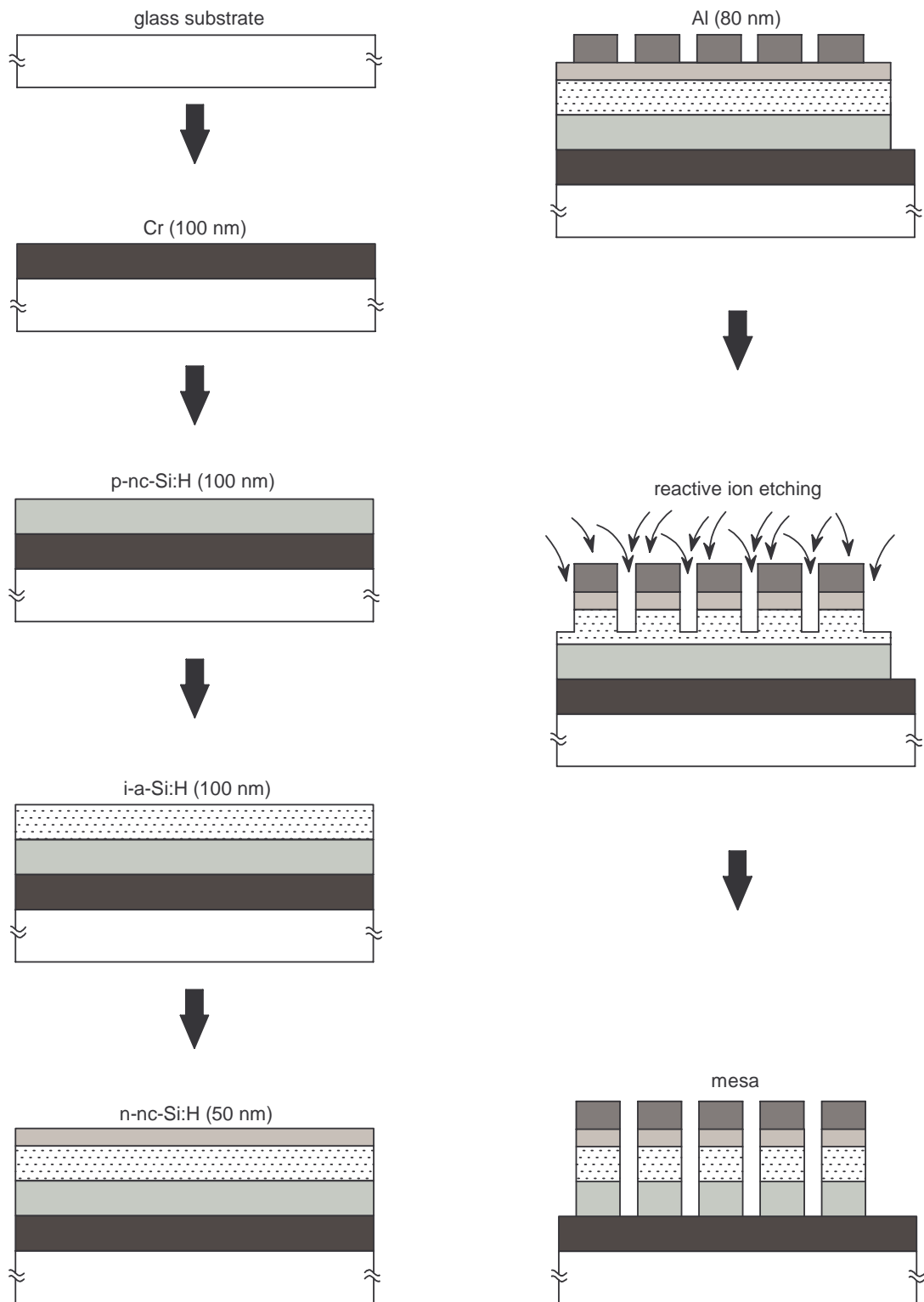


Figure 4.1: Fabrication steps of a-Si:H based homojunction *pin* diode.

the Cr coated glass substrates were immediately placed on the PECVD bottom electrode. At this step, the reactor was waited for about 2 hours to reach the temperature of 473 K and the vacuum of 1 mTorr. Then, 100 nm p^+ nc-Si:H was deposited on the glass/Cr structure. It was followed by the growth of 100 nm a-Si:H and 50 nm n^+ nc-Si:H layers successively. The growth conditions of p^+ nc-Si:H and a-Si:H films are given in Table 4.1. For n -type layer, the previously optimized parameters of n^+ nc-Si:H film were used in all diode sets (see section 3.3). When the PECVD process was over, the system was closed and the samples were kept in vacuum until the temperature was dropped down to 323 K. Next, the glass/Cr/ pin structure was taken out of the PECVD chamber and the dust, possibly present on the diode surface, was swept away by the nitrogen gun. Then, the samples were placed on the dot contact masks with 1 mm dot diameter. Subsequently, the sample holder was screwed into the thermal evaporation system for the coating of 80 nm Al. Finally, glass/Cr/ pin /Al structure was put into the reactive ion etching system and the 1 mm diameter diodes were isolated from each other to form the mesa as shown in Fig. 4.1. The obtained homojunction pin structure is shown in detail in Fig. 4.2.

The I-V characteristics of the produced diodes were firstly measured at room temperature in forward and reverse bias regimes. For this purpose, the data was collected by an electrometer (Keithley 595 Quasistatic CV meter) controlled by a computer program. The optimized diode was then chosen for the temperature scanned I-V analysis. These experiments were performed using the cryostat system, mentioned in section 2.2, in addition to the above elec-

Table 4.1: Deposition parameters of p^+ nc-Si:H and a-Si:H films used in homojunction a-Si:H based pin diodes. The n^+ nc-Si:H film and the substrate temperature of 473 K were kept the same for all diodes. The p^+ nc-Si:H and a-Si:H films were grown under the RF power density of 160 and 22 mW/cm², respectively. The B₂H₆ gas was 1000 ppm diluted in H₂.

Diode#	Film	Gases (sccm)				Pressure (Torr)
		SiH ₄	H ₂	B ₂ H ₆	Total	
#1	p^+ nc-Si:H	3	190	5	198	1
	a-Si:H	10	200	0	210	0.5
#2	p^+ nc-Si:H	3	190	10	203	1
	a-Si:H	10	200	0	210	0.5
#3	p^+ nc-Si:H	3	190	10	203	1
	a-Si:H	10	200	0	210	1 → 0.5
#4	p^+ nc-Si:H	3	190	10	203	1
	a-Si:H	10	200	0	210	1
#5	p^+ nc-Si:H	3	190	10	203	1
	a-Si:H	10	50	0	60	0.5

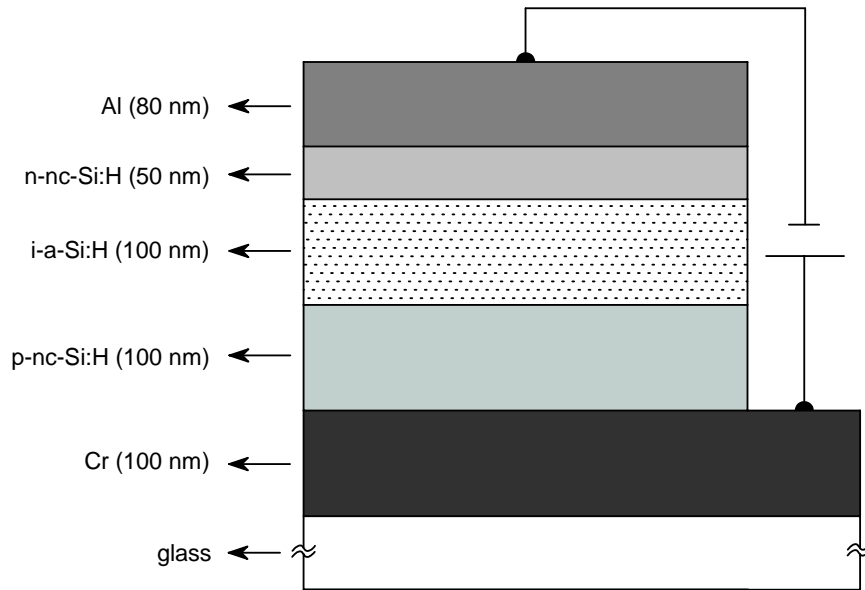


Figure 4.2: Schematic of the complete homojunction *pin* diode used in electrical measurements with the bottom (Cr) and the top (Al) electrodes.

trometer.

Very sensitive measurements of the optical absorption coefficient were performed by the constant photocurrent method (CPM). Using a Si photodiode, the energy dependence of the absorption coefficient of a semiconductor was determined at energies as low as 1.2 eV. The photocurrent was measured with the setup depicted in Fig. 4.3. The excitation light was produced by a tungsten halogen lamp (Oriel 7340) operating at 120 W, supplied from a stabilized dc power supply (HP 6642A). A shutter was placed just in front of the outlet of the lamp to determine the photocurrent accurately for each wavelength. After passing through the low-pass filter for the elimination of the higher orders of the radiation (2λ , 3λ , etc.), the lamp light was decomposed into single wavelength by the grating monochromator. The wavelength was automatically scanned by the computer program. The monochromatic light was then incident on a beam splitter, where it was separated into transmitted and reflected parts. The former fell onto the detector after being chopped at 83 Hz and the output signal was amplified by the lock-in amplifier. The latter was focused on the sample (e.g. *pin* diode and a-Si:H thin film). The sample had Cr as bottom and ITO as top electrodes. The use of the transparent ITO electrode was crucial to maximize the photocurrent which in exchange minimizes the noise during the experiment. The dark current and the total current under illumination were measured by an electrometer (Keithley 595 Quasistatic CV meter) and their difference (i.e.

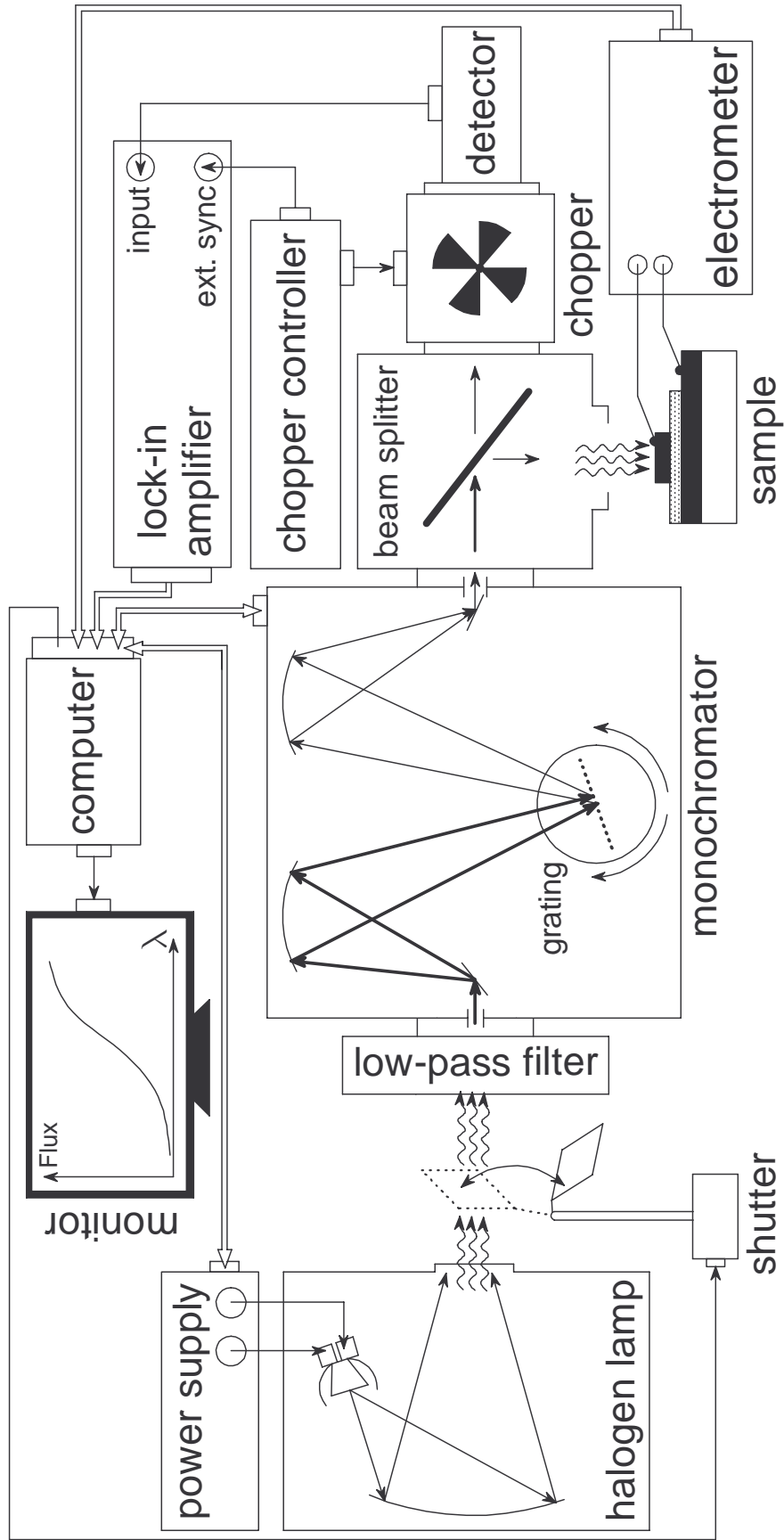


Figure 4.3: Experimental setup for the CPM measurements.

photocurrent) was kept constant via the computer program by adjusting the intensity of the incident light. It is well known that, the photocurrent at a particular wavelength is related to the absorbed fraction of the incident photon flux as follows:

$$J(h\nu) = \alpha(h\nu)\Phi(h\nu), \quad (4.1)$$

where $\alpha(h\nu)$ is the absorption coefficient of the sample and $\Phi(h\nu)$ is the total photon flux incident on the sample. Thus, in this experiment, by keeping $J(h\nu)$ constant, the inverse of the photon flux gave out the absorption coefficient dependence on the energy. However, these $\alpha(h\nu)$ are relative values of arbitrary units. Therefore, another technique, such as the UV-visible transmittance spectroscopy, is required to extract the actual absorption coefficient especially at higher energies. Then, the low energy part of the CPM data can be matched to the actual data at higher energies. As a result, the energy dependence of the absorption coefficient can be obtained from the midgap towards deep inside the valence band. The more detailed derivation on the principles of CPM can be found in [69].

4.3 Results and discussions

4.3.1 Deposition parameters for optimum pin diode

The I-V characteristics of five *pin* diodes are presented in Fig. 4.4. Increase in diborane flow rate of p^+ nc-Si:H film resulted in higher carrier injection into the intrinsic region from the p -side (see diodes #1 and #2 in Fig. 4.4-a). As shown in Fig. 3.1-b, the doping efficiency of p -type layer used in these diodes is higher at $B_2H_6/SiH_4=0.34\%$ than at 0.17% for the films grown around the edge of the PECVD electrode. Consequently, the rest of the *pin* diodes were grown with B_2H_6/SiH_4 of 0.34% .

Next, the variation of the deposition pressure of the intrinsic layer (a-Si:H) from 0.5 Torr to 1 Torr improved the diode properties as shown in Fig. 4.4-b. This may be associated with the decrease of ion energy of the plasma species, which can reduce the ion bombardment damage on the growing film surface. Besides, use of 1 Torr during the intrinsic layer deposition provides the same deposition pressure for all three layers, so that the transition between p/i and i/n interfaces becomes smoother. In diode #3, the pressure did not change from p to i growth but was reduced to 0.5 Torr at the mid of i layer deposition. Since the I-V curves of diode #2 and #3 are similar (Fig. 4.4-b), the I-V characteristics seems to be affected rather by the i/n interface. Despite the successful carrier injection into the intrinsic layer, the I-V characteristics of diode #4 still experience some junction problems, obvious from the large ideality

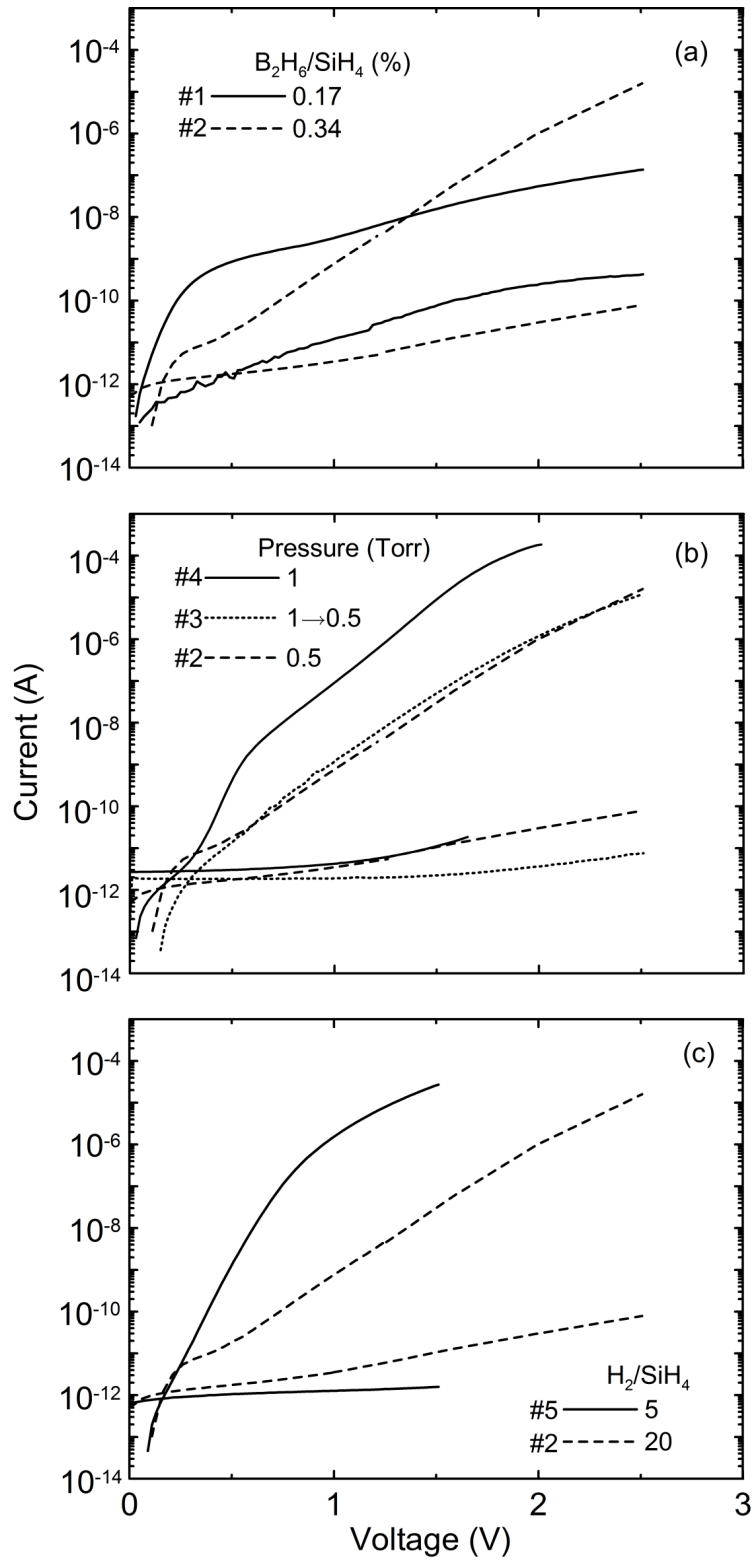


Figure 4.4: I-V characteristics at forward and reverse biases of homojunction a-Si:H based *pin* diodes: (a) #1 and #2, (b) #4, #3 and #2, (c) #5 and #2 (refer to Table 4.1).

factor above 0.5 V (Fig. 4.4-b). The resulted $\eta > 4$ may stem from the effective junctions of few diodes within the whole *pin* structure [70].

In order to further improve the junction properties, the hydrogen dilution ratio of a-Si:H layer was changed and the rest of the parameters were as in diode #2. In diode #5, the H_2/SiH_4 flow ratio was decreased from 20 to 5 and this drastically enhanced the diode properties (Fig. 4.4-c). The optical absorption spectra of both diodes #2 and #5 are very similar, such that E_{04} and E_0 of these diodes are nearly the same. In this regard, this enhancement, observable only in I-V characteristics, should arise from the reduced hydrogen ion bombardment on the *p/i* interface and/or from the improved quality of the intrinsic a-Si:H layer. When compared to diode #4, the #5 one has lower I_r and higher I_f with a single ideality factor (see Fig. 4.4-b and -c). As a result, the diode #5 is considered to be the optimized structure, which is analyzed below in detail.

4.3.2 I-V measurements of the optimized pin diode

The I-V characteristics of the diode #5 are given in Fig. 4.5. The linear fit of $\log I_f$ versus V results in ideality factor of ~ 1.7 . This linear region lasts over 5 decades in current implying high built-in potential. The rectification ratio is above 4×10^6 at 1.2 V, which indicates good junction formation. The reverse saturation current is almost voltage independent.

The I-V characteristics of the optimized a-Si:H based homojunction *pin* diode #5 were also measured at various temperatures (Fig. 4.6-a). The temperature was scanned between 40 K and 440 K during both cooling and heating processes. Below 270 K, the current is stuck at around 1 pA at low voltage biases and does not decrease further. Therefore, the reverse I-V data could not be taken below 270 K. It seems to be a surface leakage which would prevent the measurement of the actual diode current at low current levels. A possible reason for that is the condensation of the water vapor residual within the cryostat chamber on the sample surface.

Both forward and reverse currents at a particular voltage increase with the measurement temperature. The corresponding activation energy (E_A) can be found from the Arrhenius plot for the reverse saturation current ($I_{r,SAT}$) as shown in Fig. 4.6-b. $I_{r,SAT}$ was estimated from both the experimental reverse current at -0.8 V and the theoretical fit of the forward I-V curves using the Eq. 1.22. Two distinct linear regions can be recognized for the determination of E_A . From 440 K to 240 K, the Arrhenius plot exhibits an activation energy E_A of 830 meV. This value is slightly lower than half of the optical gap of a-Si:H which is compatible

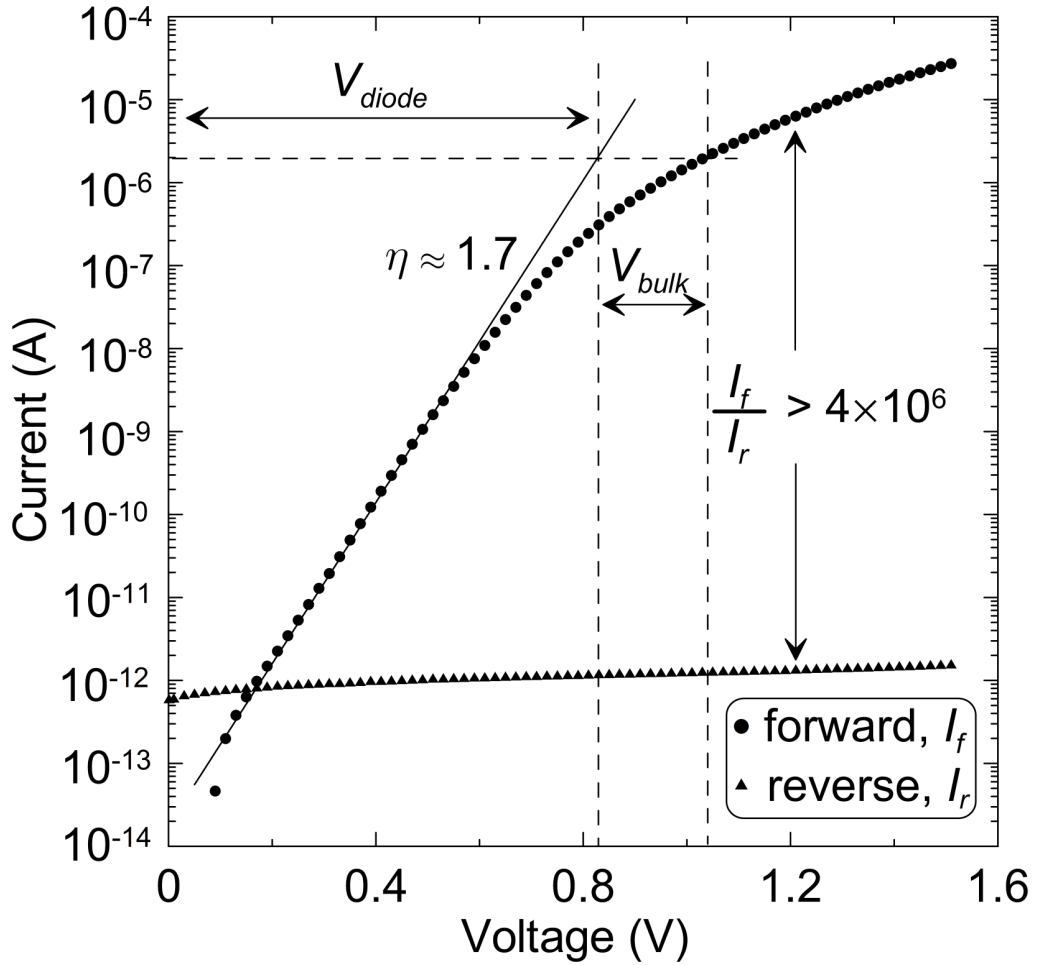


Figure 4.5: I-V characteristics of homojunction a-Si:H based *pin* diode #5 at forward and reverse biases. The ideality factor η is found from the slope of the linear fit. The rectification ratio is indicated at 1.2 V.

with the slightly *n*-type nature of the intrinsic a-Si:H. The low temperature part of Fig. 4.6-b shows very weak temperature dependence with activation energy as low as 55 meV. Such sharp reduction in the activation energy from 830 meV to 55 meV is due to the change in the transport mechanism from the band transport of thermally excited carriers to the hopping around the midgap at very low temperatures.

The diode ideality factor, η , has been calculated from the theoretical fit of the forward I-V data (Eq. 1.22), which was also applied above to determine $I_{r,SAT}$. The temperature dependence of η is provided in Fig. 4.6-c. At high temperatures from 240 K to 440 K, η slightly decreases from 2.1 to 1.7. This behavior is in agreement with the theoretical expectation (Eq. 1.21), where the transport is dominated by tail-to-tail recombinations within the exponential

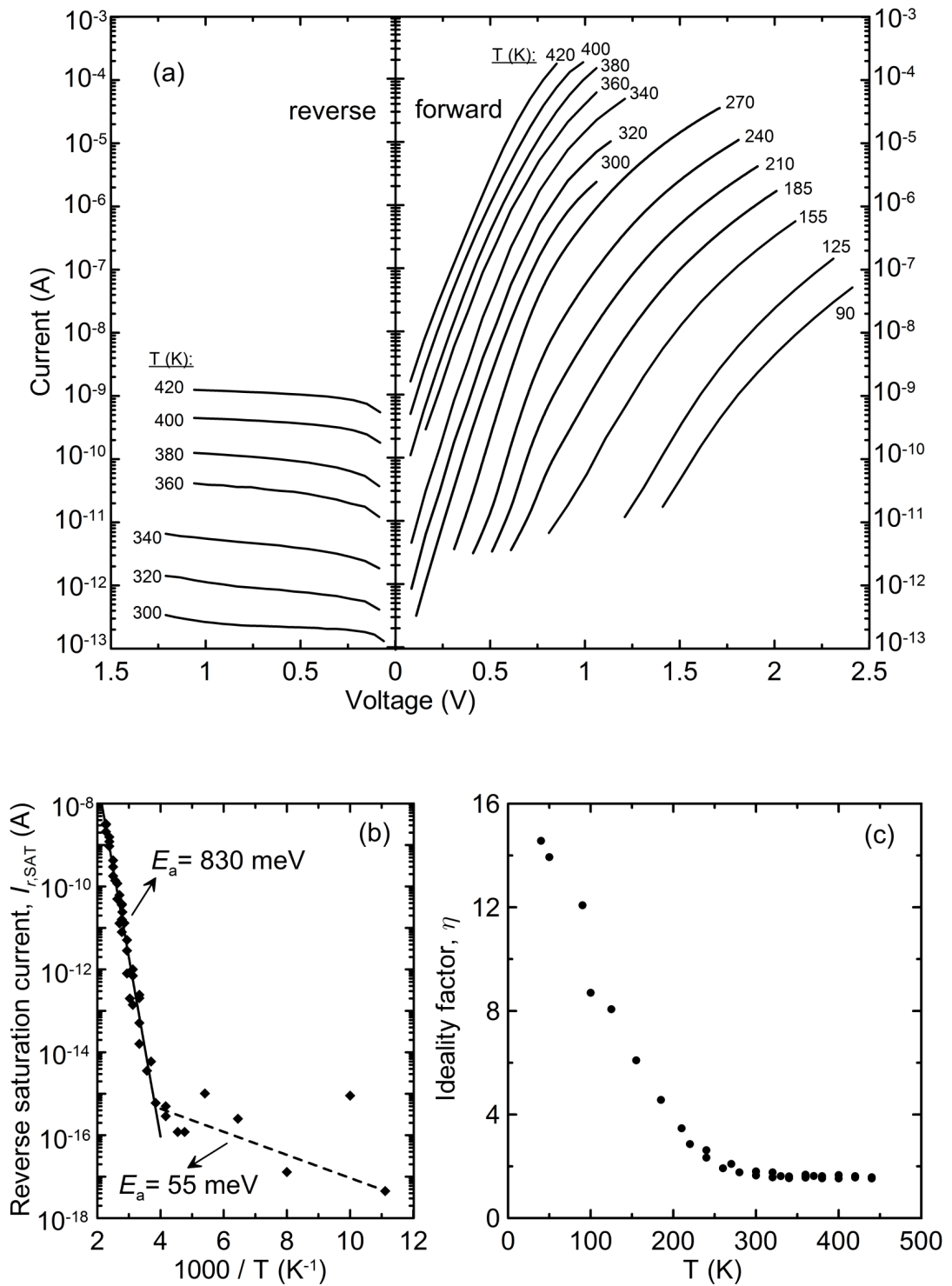


Figure 4.6: (a) Temperature scan of the forward and reverse I-V characteristics of the diode #5 of area $7.8 \times 10^{-3} \text{ cm}^2$. (b) Arrhenius plot of the reverse saturation current. (c) Temperature dependence of the diode ideality factor.

band tails energetically lying between the quasi-Fermi levels of the p and n layers, E_{Fp} and E_{Fn} , respectively. At low temperatures from 40 K to 240 K, η sharply decreases from 14.7 to 2.1. Similar to the above argument, such high ideality factor, i.e. $\eta > 2$ can be explained by means of the addition of the individual ideality factors of each junction possibly present in the device. The effects of these junctions on the I-V curves are likely to be less pronounced at high temperatures, since the thermionic emission of the carriers may be expected over the barriers of imperfect junctions. On the other hand, the imperfections in the metal/semiconductor (quality of the ohmic contacts), p/i and i/n interfaces can impose their own diode characteristics more distinctively at lower temperatures.

It is seen in Fig. 4.6-a that there are two main regions in the forward I-V curve of a pin diode. In the first part, the current exhibits an exponential dependence on the voltage, i.e. it is linear in the semi-log plot. This exponential behavior stems from the reduction of the barrier between the p and n layers with applied forward bias. The lower the barrier height, the smaller the voltage drop across the diode. At some voltage, the separation between E_{Fp} and E_{Fn} becomes comparable to the built-in potential energy of the diode (i.e. $E_{Fn} - E_{Fp} \approx qV_{bi}$, see Fig. 1.2). Beyond this voltage value, the bands become flat and the voltage drop is dominated not by the diode but by the sample bulk. In this respect, the pin structure can be regarded as a diode series connected to a resistor. The limitation of the current by the series resistance is reflected in the second region of the forward I-V curve where the increase in the current deviates from the exponential behavior. The voltage drop across the sample bulk (V_{bulk}) can be determined quantitatively at a particular current from the difference between the applied voltage ($V_{applied}$) and the diode voltage of the linear region (V_{diode}) in the semi-log plot (see Fig. 4.5 for demonstration).

In Fig. 4.7, the current versus the voltage drop across the sample bulk ($V_{bulk} = V_{applied} - V_{diode}$) is given in log-log plot for various temperatures. The series resistance seems to be ohmic (i.e. slope 1) until about 0.01 V at all temperatures. Above this voltage, the current becomes space charge limited with slope > 1 . The slope increases gradually up to 3 at 0.2 V at 220 K, whereas at higher temperatures, the slope increases up to at most 2. In other words, the rate of change of the differential voltage exponent, a , during a single I-V measurement decreases with increasing temperature (see ref. [71] for similar data measured from n^+in^+ and n^+nn^+ devices). This behavior should be related to the change in the density of trapped carriers at particular voltage and temperature. Since the thermal re-emission of a trapped carrier is more difficult at lower temperatures, the trapped carrier density at a particular voltage would

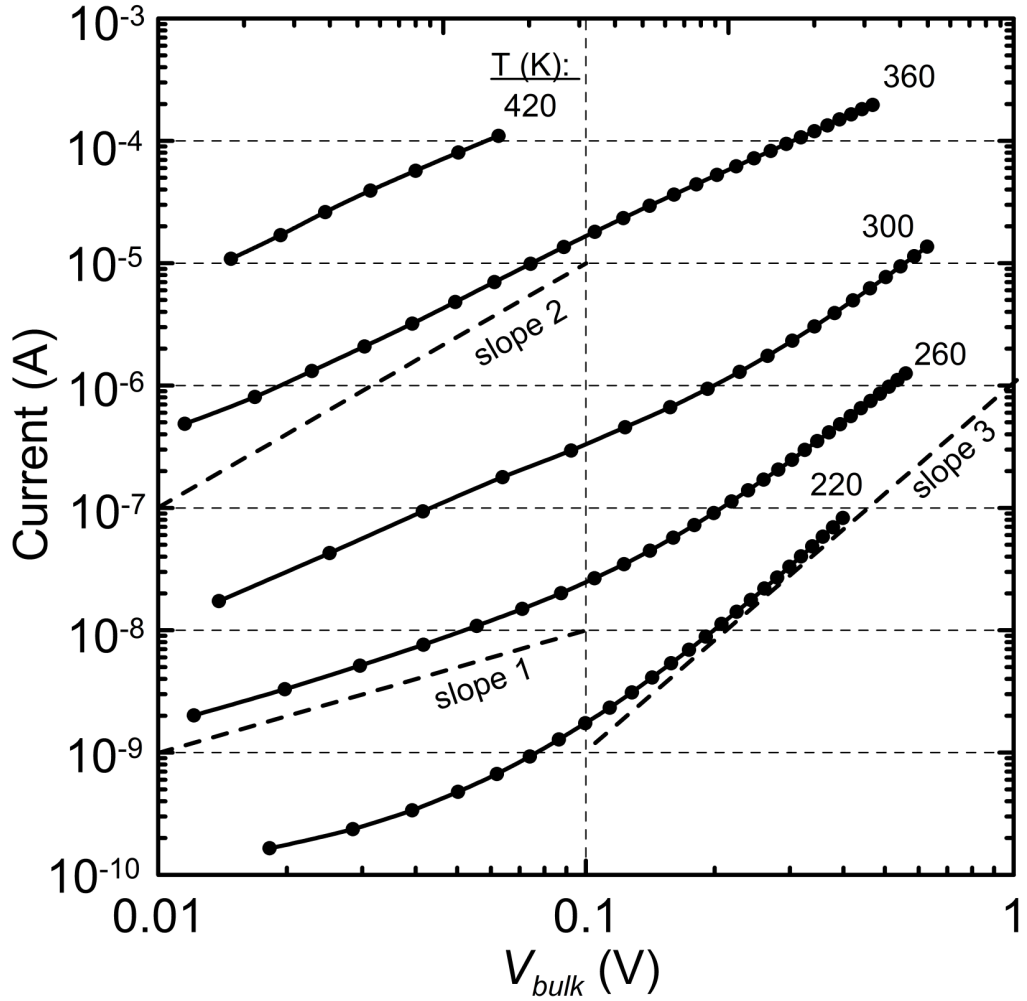


Figure 4.7: Temperature scan of the forward current of diode #5 with respect to the voltage drop across the bulk of the sample, for which the series resistance is responsible. The slopes indicated by the dashed lines are guides for $J \propto V^a$ with $a=1, 2$ and 3 .

be higher. The slope of the $\log I$ vs. $\log V$ curve would exceed 2 if the space charge is large enough to reflect the exponential energy distribution of the band tails. This case becomes more probable as the temperature is reduced. At higher temperatures, the current would be controlled by the localized states lying around the quasi-Fermi levels [71], and the voltage exponent would be around 2, as observed in Fig. 4.7.

4.3.3 DOS calculation from SCLC and CPM results

In Fig. 4.8, the CPM results are reported for the intrinsic layer of the diode #5. With the assumption that the energy bands of the doped layers are flat, the measurement was performed directly from the *pin* diode #5 under reverse bias of 0.3 V. The optical gap, E_{04} , was found to

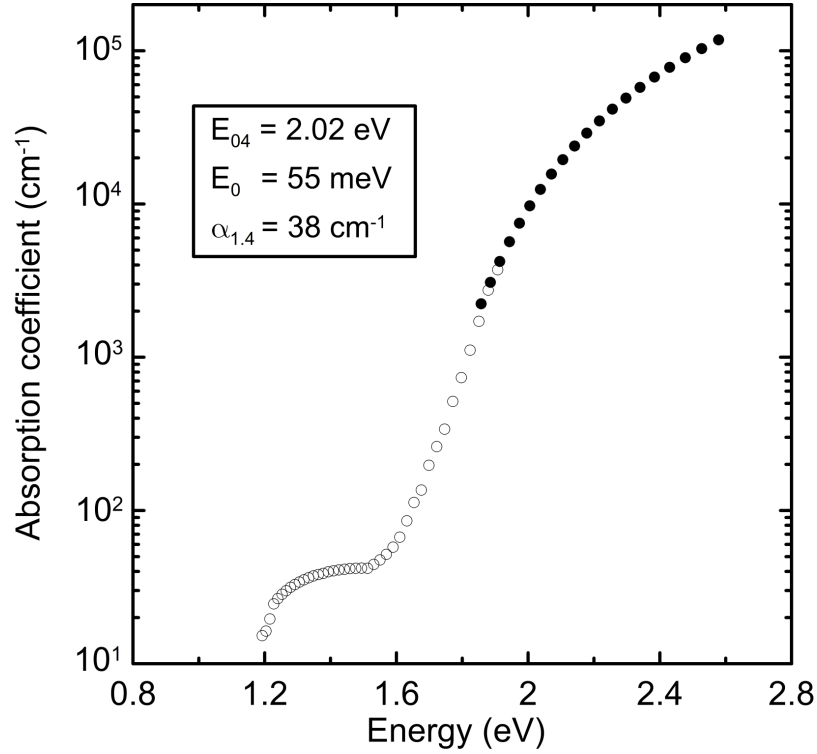


Figure 4.8: Energy dependence of the optical absorption coefficient measured by CPM (\circ) and UV-visible transmittance (\bullet) techniques from the *pin* diode #5.

be 2.02 eV, which is slightly larger than the usually reported value of 1.80 eV. The subgap absorption tail (or Urbach energy, E_0) was estimated as 55 meV in agreement with the literature. The value of the absorption coefficient at 1.4 eV ($\alpha_{1.4}$) gives an idea about the density of deep energy levels within the forbidden gap of a-Si:H. For the device quality a-Si:H films, $\alpha_{1.4} \approx 1 \text{ cm}^{-1}$ [72]. $\alpha_{1.4}$ of a-Si:H in this *pin* device is 38 cm^{-1} , which is about 1 order of magnitude higher. This difference is probably due to the effects of the doped layers, whose larger density of deep states may absorb low energy photons and contribute to the photocurrent.

The distribution of the energy levels within the forbidden gap of a semiconductor is the main factor that affects its electro-optical properties. The knowledge of this distribution not only gives an idea about the quality of the film, but also helps to explain some other experimental results, such as the I-V characteristics. In Fig. 4.9, the energy dependence of density of states (DOS) was deduced from the space charge limited current (SCLC) measurement (see Fig. 4.7) and the optical absorption spectrum at room temperature.

The SCLC technique supplies the state density above the Fermi level provided that the conduction is dominated by the electrons over the holes [71, 73]. This is the case in the a-

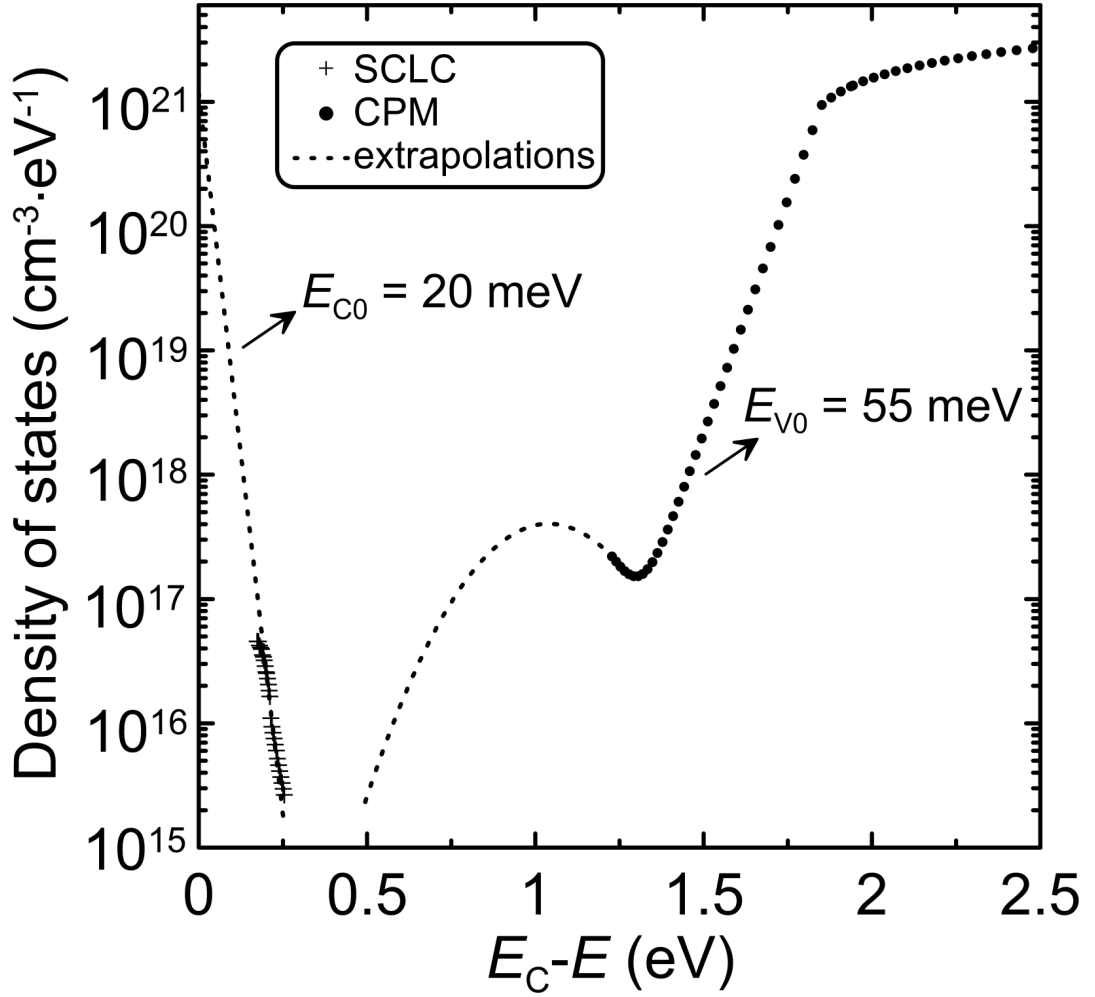


Figure 4.9: Density of states (DOS) distribution within the forbidden gap of the intrinsic a-Si:H film determined from SCLC and CPM techniques. The dashed lines are the extrapolations of data for the exponential band tail states and the Gaussian distribution of the deep levels.

Si:H based *pin* diode where the doping efficiency and the majority carrier mobility in the *n*-layer are much higher than those of the *p*-layer (see appendix E). The Fermi level at the Cr electrode (electrode under the *p*-layer) is related to the voltage drop across the sample bulk via Eq. E.8. Assuming that the traps below the Fermi energy are filled at steady state, the DOS below the conduction band edge can be calculated using Eq. E.20, which depends on the differential slope of the I-V curve in the SCLC region of Fig. 4.7.

On the other hand, the valence band extended and localized states were determined from the experimentally found $\alpha(h\nu)$ using the MATLAB fitting program. With the assumption for low temperatures, where the energy states below the Fermi level are filled and those above are

empty, $\alpha(h\nu)$ can be written as:

$$\alpha(h\nu) = \frac{c}{E} \int_{E_c-E}^{\infty} h(\epsilon) g_c(E + \epsilon) d\epsilon, \quad (4.2)$$

where $h(\epsilon)$ is the energy distribution of DOS below the Fermi level and g_c is the conduction band extended state density with the $E^{1/2}$ dependence. The measured absorption spectra was fitted according to the procedure defined by Kocka *et al.* [74,75], where the function $h(\epsilon)$ was adjusted using the minimization feature of MATLAB through:

$$\Sigma(\alpha_{measured}(E) - \alpha_{calculated}(E))^2 = 0. \quad (4.3)$$

Consequently, both techniques complement each other to reveal DOS within the whole forbidden gap starting from the conduction band edge towards deep inside the valence band (Fig. 4.9). The characteristic energy of the conduction band tail states was found to be 20 meV which is very similar to our previous result deduced from time-of-flight experiments [76]. DOS at the conduction and valence band edges were taken as $1 \times 10^{21} \text{ cm}^{-3} \text{ eV}^{-1}$ and $2 \times 10^{21} \text{ cm}^{-3} \text{ eV}^{-1}$, respectively. The maximum density of the dangling bond states is $4 \times 10^{17} \text{ cm}^{-3} \text{ eV}^{-1}$ located at around 1 eV. The DOS curve exhibits a minimum between 0.4 eV and 0.5 eV below the conduction band edge, which is a characteristic property of a-Si:H where the p-like valence band tail is wider than the s-like conduction band tail [14].

4.4 Conclusion

Five sets of *pin* diodes were fabricated by PECVD and deposition parameters were optimized for high quality I-V diode characteristics. These conditions were determined as: $\text{B}_2\text{H}_6/\text{SiH}_4 \approx 0.34\%$ for *p*-type nc-Si:H layer and $\text{H}_2/\text{SiH}_4 \approx 5$ for intrinsic a-Si:H layer. The ideality factor and the rectification ratio of the optimized *pin* device were ~ 1.7 and $> 4 \times 10^6$ (at 1.2 V), respectively. The thermal activation energy of the reverse saturation current, $E_A = 830$ meV, is reasonable since the undoped a-Si:H is slightly *n*-type. The energy distribution of DOS was calculated from SCLC and CPM results, both measured directly from the *pin* structure. The obtained DOS, $E_{C0} = 20$ meV and $E_{V0} = 55$ meV are in agreement with the previous reports.

CHAPTER 5

ELECTROLUMINESCENT a-SiN_x:H BASED PIN DIODES

5.1 Introduction

It is well known that the electroluminescence (EL) of *pin* diodes with a-Si:H intrinsic layer has low intensity and its spectral energy distribution usually remains below the visible region. In order to shift the EL spectrum to higher energies, a-Si:H based alloys, such as a-SiC_x:H, a-SiO_x:H and a-SiN_x:H, are produced [40, 41, 77]. But EL intensity of these diodes is still below the detection limit of the naked eye [14]. This problem arises from the insufficient free carrier density and low carrier mobility through the band tail states. As a solution, the nanocrystalline Si islands may be created within the matrices of the diode active layer. By this way, the free carrier density is increased and their mobility is boosted, which produces intense EL. The formation of Si nanocrystallites usually requires high cost deposition such as ion implantation [78, 79] or low cost PECVD technique, both followed by post-deposition annealing treatments at high temperatures (see appendix B).

In this work, a spectacular enhancement of EL intensity has been achieved by applying high electric field (F) to both a-Si:H and a-SiN_x:H based *pin* structures. Under high field, the diode seems to undergo the so-called forming process (FP) generally involving the crystallization of the intrinsic layer [80, 81]. To investigate this phenomenon in detail, EL spectra and I-V characteristics of a-SiN_x:H based *pin* diodes before and after FP are studied. The structures of p⁺ and n⁺ injecting layers of the *pin* structure have always been kept the same as described in chapter 3. The deposition parameters of the intrinsic layer were chosen similar to those in chapter 2 with the aim of visible light emission via the recombination of the electron hole pairs (EHPs) injected in this region. In this respect, the optimization results obtained in chapters 2 and 3 have been combined.

5.2 Experimental details

Four different sets of *pin* diodes were produced and characterized. Each *pin* structure was deposited on Cr coated glasses in one PECVD cycle. The p^+ and n^+ nc-Si:H injecting layers of all diodes were kept the same. The optimized deposition conditions, given previously in chapter 3, were utilized for the growth of p^+ and n^+ nc-Si:H films. The deposition parameters of the intrinsic layers for each diode were changed as specified in Table 5.1. D0 (diode #5 in chapter 4) is the homojunction *pin* diode, while other three heterojunction *pin* diodes differ in the nitrogen content of the intrinsic layer. During the deposition process of D0 the substrate temperature (T) was kept constant at 473 K, whereas in a-SiN_x:H based diodes it was raised up to 523 K for the intrinsic layer and then lowered back to 473 K for n^+ nc-Si:H film growth. Then, window electrodes (Al, Cr and ITO) of 1 mm diameter were deposited through the shadow mask over the n^+ nc-Si:H layer of the resulted glass/Cr/*pin* structure as indicated in Fig. 5.1. Al and Cr were deposited by thermal and electron-beam evaporation techniques, respectively, while ITO was grown by sputtering at 120 W under 3×10^3 mbar using Ar as the process gas (for details of the deposition systems see [48, 66]).

Current-voltage (I-V) measurements before and after FP were done with electrometer (Keithley 617, for $I < 20$ mA) and dc power supply (HP6642A, for $I > 20$ mA). EL spectra were measured with the setup shown in Fig. 5.2. The as-measured EL spectra were corrected via dividing them by the responsivities of the corresponding photodetectors, which are provided in appendix C.

The temperature scan of EL spectra and corresponding I-V characteristics was done for the formed D2 and D3 samples (the results for D2 are presented in this work). After the diode was placed on the sample holder unit of the liquid He cooled closed-cycle cryostat (shown in Fig. 5.2), it was intentionally subjected to a voltage of 13 V until FP was completed. Then,

Table 5.1: Deposition parameters of the intrinsic a-Si:H and a-SiN_x:H films used in the *pin* diodes of this work. The chamber pressure of 0.5 Torr and RF power density of 22 mW/cm² were used during the growth of all these intrinsic layers.

Diode#	Intrinsic film	Gases (sccm)				Substrate T (K)
		SiH ₄	H ₂	NH ₃	Total	
D0	a-Si:H	10	50	0	60	473
D1	a-SiN _x :H	10	0	20	30	523
D2	a-SiN _x :H	10	0	40	50	523
D3	a-SiN _x :H	5	0	45	50	523

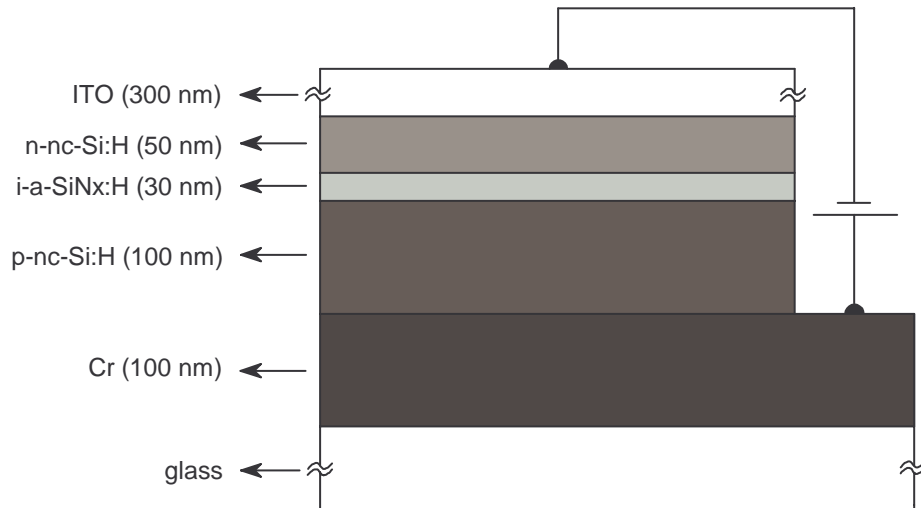


Figure 5.1: The schematic cross-sectional view of the complete *pin* structure used throughout EL and I-V experiments with the bottom (Cr) and the window (ITO) electrodes.

the rotary pump was shut to maintain vacuum inside the unit. Subsequently, the liquid helium cooled closed-cycle cryostat was operated for cooling the sample. During cooling down procedure gate valve was closed to prevent back flow of oil and pump was shut when the pressure reduced to 1.5 mTorr, since vacuum generated by solidification of residual vapor overcomes that of mechanical pump. T was followed by the computerized temperature controller. Second, the cryostat compressor of the cryostat was also shut down after T was lowered to 10 K for avoiding any mechanical disturbances from the rotary pump and the compressor during the measurements of EL spectra and I-V characteristics. Moreover, the diodes under vacuum were found to be very vulnerable to thermal destruction. Actually, the previously reported electron emission from the formed dielectric films [82] could be clearly observed by naked eye in the present experiment. The risk of destruction also limits the highest possible applied voltage, since the thermal destruction was inevitable above 11 V under vacuum. The EL spectra were started to be measured around 9 V at a constant current density of 3.2 A/cm^2 for increasing temperatures from 160 K to 424 K. The detection of the emitted light is similar to that in the PL measurement, which was explained in detail in section 2.2.

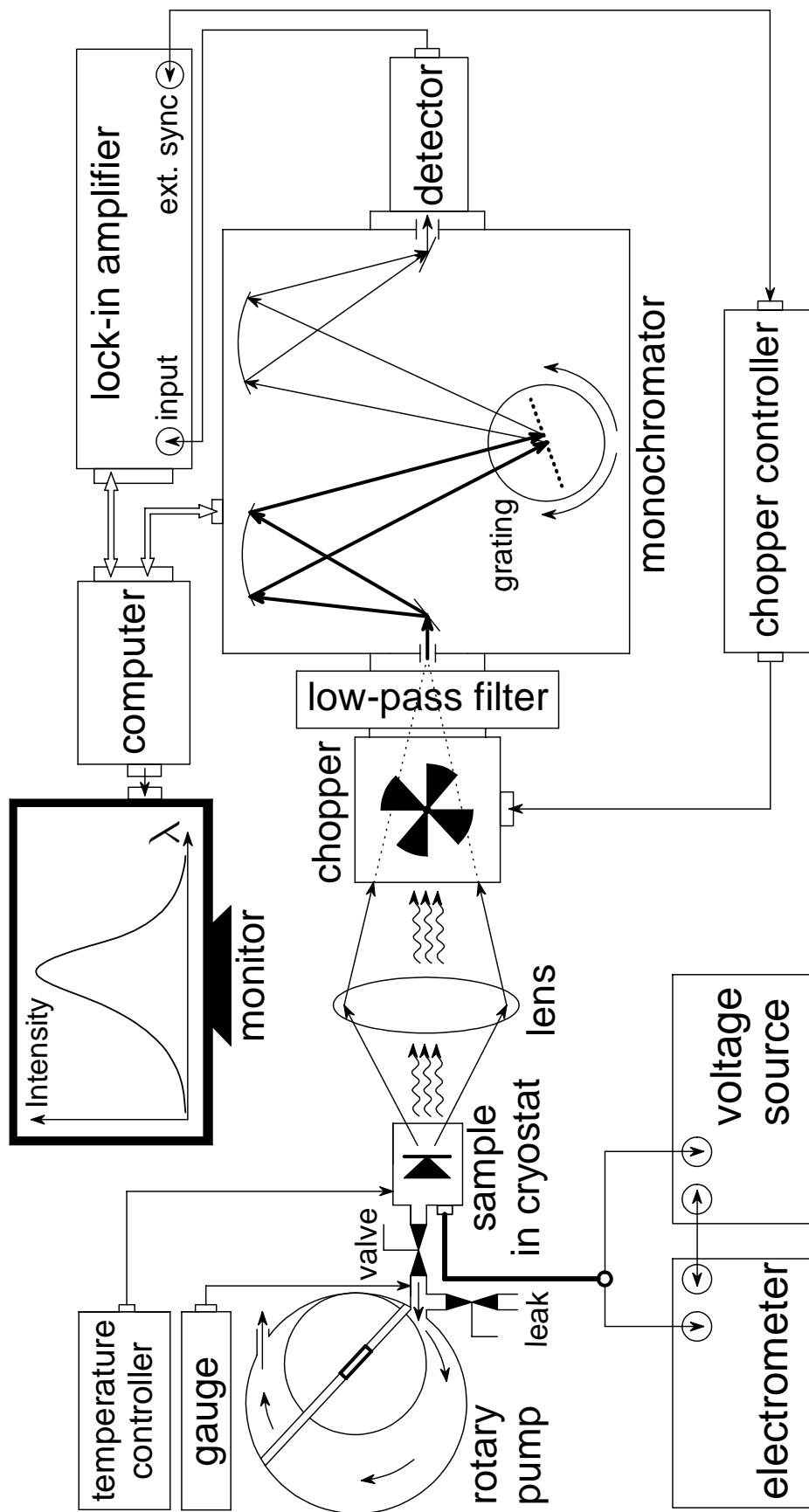


Figure 5.2: Experimental setup for temperature scanned EL and I-V measurements.

5.3 Results and discussions

5.3.1 Forming process of pin diodes

After the application of high voltage, a forming process (FP) of *pin* diodes resulted in structural modifications, which led to drastic increase in the current density. In Fig. 5.3, I-V curves of a-Si:H based homojunction *pin* diode (D0) are plotted before and after FP. Both forward and reverse I-V measurements of the fresh diode are repeatable unless the maximum voltage exceeds about 3 V. In order to observe the ultimate deviation in the I-V curve after FP relative to the original one, the measurements were taken several times up to 12 V. The deviation in the I-V curves together with the macroscopically observable structural changes depends on whether high voltage is applied in the forward or reverse direction. For the forward case, I-V curve measured from 0 to 12 V is reported in Fig. 5.3-a as the forward-before(1). The cycle

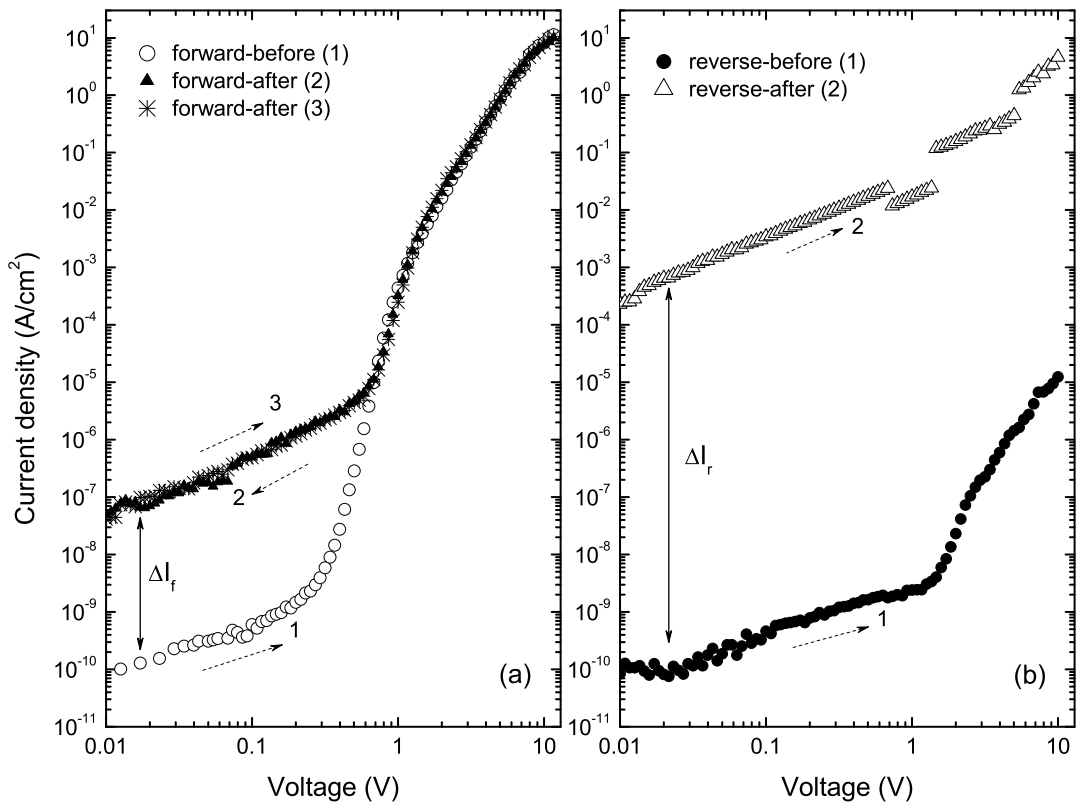


Figure 5.3: (a) Forward and (b) reverse I-V characteristics of a-Si:H based homojunction *pin* diode (D0) before and after the forming process. The numbers and the arrows represent the measurement sequence and the direction of the measurement, respectively. ΔI_f and ΔI_r indicate the difference between the currents at low voltage region before and after the forming process for the forward and reverse cases, respectively.

is completed by measuring I-V from 12 V to 0. This second half, reported in Fig. 5.3-a as the forward-after (2), exhibits an increased current density of about 3 orders of magnitude along the lower voltage region (below 0.7 V) compared to the first half of the cycle, although the current density remains identical beyond 0.7 V. The extra current at low voltage region seems a parallel leakage current where the eventual shunt resistance of the diode would be seriously reduced under high electric field during the first half. A subsequent measurement, namely forward-after (3) resulted in the same curve with that of forward-after (2), which indicates that the ultimate deviation is reached, i.e. the final structure was stable when forward bias measurements were further repeated. The deviation of the I-V curve from the original one might be related to some changes in the diode structure. The structural changes within the diode were also accompanied by a permanent color change of the whole ITO electrode. The reverse bias current density curve after FP (not shown here) corresponding to Fig. 5.3-a is ohmic and about 1 order of magnitude higher than that of forward-after (2) and (3) curves. As for the application of high voltage under the reverse case, the reverse I-V curve in Fig. 5.3-b was taken up to 10 V from a neighboring fresh diode (reverse-before (1)). In the subsequent reverse measurement, reverse-after (2), the I-V curve is ohmic and about 6 orders of magnitude higher than that of reverse-before (1). This ratio, ΔI_r , is 3 orders of magnitude higher than that of forward case, ΔI_f (Fig. 5.3). The macroscopic change in the diode structure was more severe when high reverse voltage was applied to the fresh diode: the point where the measurement probe touches the ITO top electrode was thermally destroyed. Therefore the FP of all the diodes in this work was performed under the forward bias.

FP also depends on deposition conditions of the intrinsic layer. For example, the I-V characteristics of the fresh and the formed structures are shown for the heterojunction diode D1 in Fig. 5.4-a. The rectification ratio of about 10^4 at 8 V indicates good injection efficiency of the fresh diode, i.e. the electrons and holes are successfully injected from either side of the a-SiN_x:H layer. When compared with an a-Si:H homojunction *pin* diode D0, the reverse biased heterojunction diode has higher leakage. This is in parallel to the expectation of higher localized state density in a-SiN_x:H films. After FP is triggered by the application of a sufficiently high voltage above 8 V, the current density at low voltage region increases drastically, qualitatively similar to the homojunction D0 in Fig. 5.3, but this increase is higher for the heterojunction D1. It should be noted here that the threshold voltage to trigger FP of D1 (>8 V) is higher than that of D0 (>3 V), which can be related to the increase of the dielectric breakdown field with the addition of nitrogen (N), in the intrinsic layer [83]. Actually, this

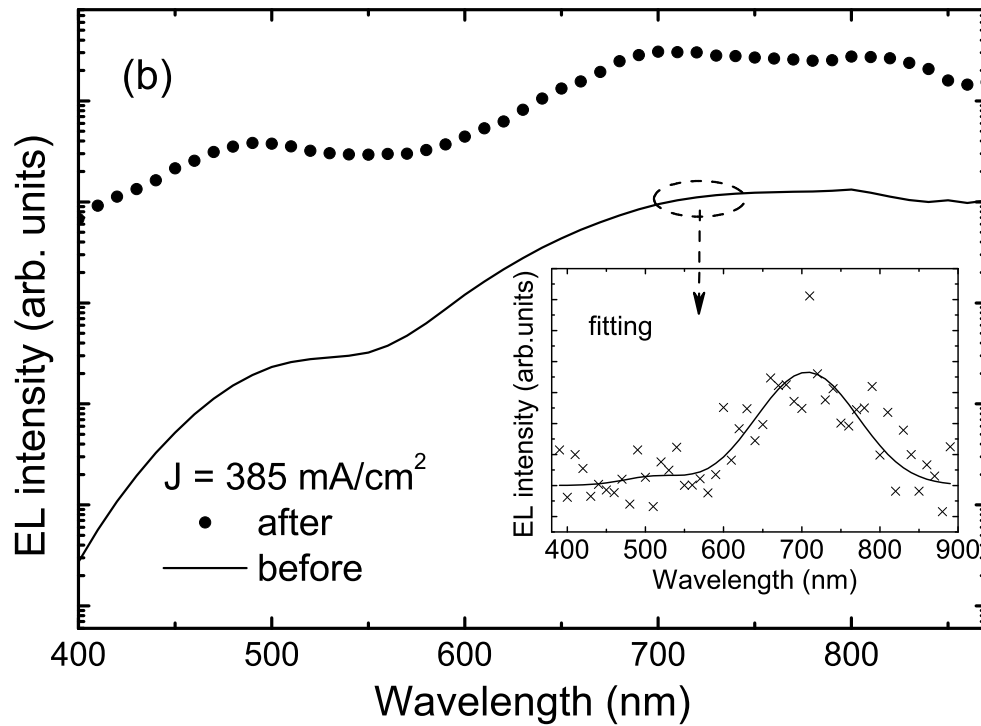
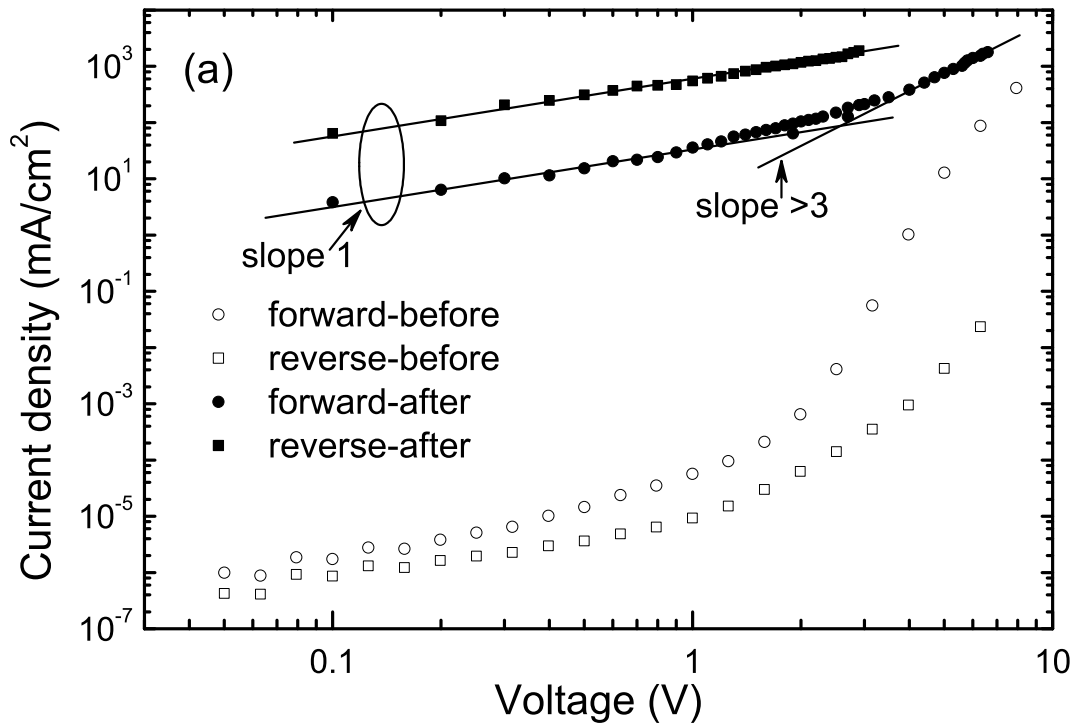


Figure 5.4: (a) The I-V characteristics and (b) the corrected EL spectrum of the diode D1 measured before and after the forming process. Inset shows the fitting of the noisy data of the fresh diode.

threshold voltage was found to rise with the increasing N content of the diodes D0, D1, D2 and D3. If it was possible to measure the behavior of the I-V curve at higher voltages without FP, the current densities of the fresh and the formed diodes would coincide at some voltage around 20 V. In this regard, the physical properties of the fresh diode at these voltages may partially remain unchanged during FP. This idea is supported by Fig. 5.3 of D0 where the low voltage current density was drastically increased after FP, whereas the current density of the formed diode D0 followed that of the fresh diode at higher voltages. Besides, the reverse current, which is ~ 1 order of magnitude higher than that of forward current, seems to be a common factor of all diodes after FP (see Fig. 5.4-a). FP affected seriously the luminescent properties of the diodes too. The EL spectrum of the diode D1 was measured at current density of 385 mA/cm^2 by the PMT before and after FP (see Fig. 5.4-b). The diode D1 emitted very weak light in the red-near infrared region before FP while the emission intensity increased more than one order of magnitude and its energy distribution remain almost the same after FP. When FP was completed, the light was uniformly emitted from the whole diode area and could be easily perceived by the naked eye in the dark room.

The ultimate forming of D0 is achieved by the application of high enough forward voltage (Fig. 5.3), which ensures the formation of the whole diode area within less than 2 seconds. However, in the case of relatively lower forward stresses, the propagation of the formation along the whole diode area may take a few minutes. For example in sample D2, the slow formation process could be observed as shown in Fig. 5.5. In this figure, the evolution of the current density (here measured current/whole diode area) with time is observed when a forward voltage stress of 12 V is applied to a fresh diode. FP of the fresh diode begins just after the bias stress application. At this time, the current density drastically increases up to 6 A/cm^2 and the formed region is easily recognizable via the self-roughening of some portion of the ITO top electrode surface. The initial area of the formed diode portion depends on both the fabrication parameters and the applied voltage stress. For this diode, it is usually more than half of the total diode area of $7.8 \times 10^{-3} \text{ cm}^2$ for voltages around 12 V. This phenomenon is accompanied with visible light emission from the formed region. As time passes, the current density slightly increases together with the lateral propagation of the formed diode portion. Finally, the whole diode is formed at about 400 s and the current density saturates at about 9 A/cm^2 . Then, the visible light is uniformly emitted from the whole surface of the diode.

The structural modifications of the diodes due to FP was investigated by the XRD measurements. As an example, the XRD spectra of *glass/Cr/pin(D2)/ITO* composite structure

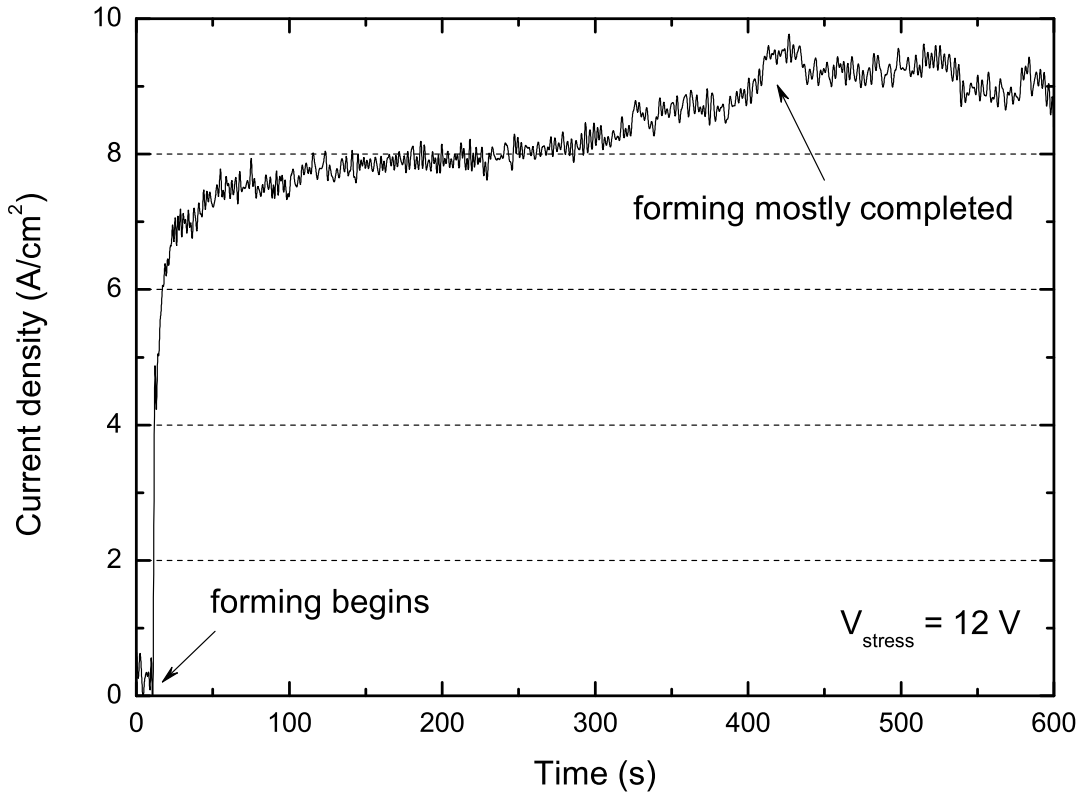


Figure 5.5: The current density versus time plot of D2 under a constant forward voltage stress of 12 V. Arrows at the beginning of the measurement and at about 400 s indicate the times at which the forming process starts and mostly ends, respectively.

before and after FP are provided in Fig. 5.6-(a). The intensity and position of the peak at 45° does not change after FP. In order to interpret this behavior the XRD spectrum of a glass/Cr structure alone was also taken (see Fig. 5.6-(b)). This spectrum has a single peak at 45° corresponding to the (110) peak of e-beam deposited Cr film [84]. Therefore, it is evident that the peak located at 45° in the spectra of the ITO coated *pin* devices actually belongs to the signal coming from the Cr film lying under the *pin* structure. After this determination, the difference between the XRD spectra of the ITO coated *pin* devices before and after FP may be more easily interpreted. The XRD measurement before FP was taken from a region of 1 cm^2 area comprising of about 30 fresh diodes of 1 mm diameter each. In the XRD spectrum of the fresh diodes, only the (400) peak of ITO can be clearly distinguished while the other peaks are almost absent. In order to see the structural differences caused by FP, these 30 fresh diodes were intentionally exposed to high forward voltage stress of 12 V until FP of each diode is completed. As mentioned above, the completion of FP was verified by the macroscopic self-

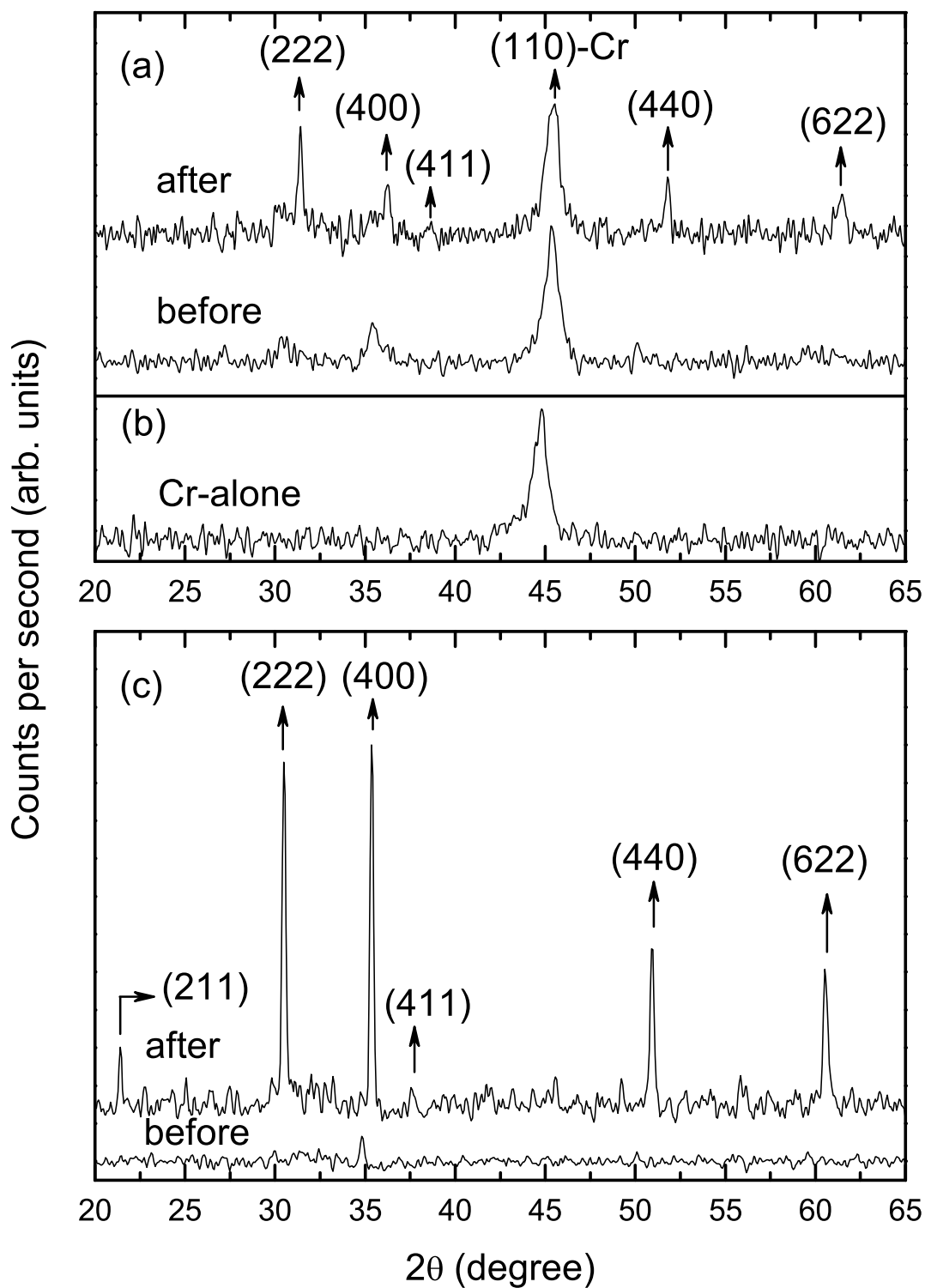


Figure 5.6: XRD spectra of (a) ITO coated a-SiN_x:H based *pin* diodes (D2) before and after the forming process, (b) glass/Cr structure to interpret the peak at 45° and (c) glass/ITO structure before and after its thermal annealing at 473 K for 30 min.

roughening of the whole surface of ITO. The XRD spectrum of these formed diodes exhibit better crystallinity compared to that of the fresh diodes. The ITO XRD peaks (222), (411), (440) and (622) have become easily discernable. The contribution of annealing treatment on the crystallization of ITO is given in Fig. 5.6-(c) where the spectra were measured from an glass/ITO structure. The as-deposited ITO film is mostly amorphous whereas, the transformation from the amorphous to the crystalline phase is experienced when the film is annealed at 473 K for 30 min. In this respect, the improvement of the ITO crystallinity during FP is likely to stem from the thermal effects induced by Joule heating. The determination of the temperature requires a high quality rapid thermal annealing system since FP lasts for few seconds. However, it is safe to consider that the temperature rise is much higher than 473 K since the crystallinity improvement during the thermal annealing at 473 K for 30 min is comparable to that obtained after FP which is completed in much shorter time duration.

Considering the fact that the thermal conductivity of ITO (11 W/K·m) is lower than that of Cr (94 W/K·m), the heat during FP may be stored at the ITO side and rather dissipated at the Cr side in glass/Cr/*pin*/ITO structure. As a consequence, the temperature rise at the n^+ /ITO interface is likely to be maximum and gradually decrease towards the Cr/ p^+ interface. Similar to the crystallinity improvement of ITO during FP, the crystallization of the layers below it may be expected [80, 81, 85, 86]. In parallel to the gradual temperature decrease, the crystallite grain size must also reduce from n^+ towards p^+ layer. Since n^+ and p^+ layers were already of nanocrystalline nature before FP, their crystallinity should just be enhanced during FP. However, the more or less silicon rich intrinsic a-SiN_x:H layer contained a-Si:H islands before FP. Under high local temperature during FP, these amorphous islands must transform to nanocrystalline grains by both several atomic rearrangements and release of H₂ to the surroundings. The free carrier density and their mobility within the nc-Si clusters should be increased by several orders of magnitude when compared to those within the amorphous phase [85]. Moreover, some inactive fraction of the dopant atoms present in the doping layers may diffuse into the intrinsic film and result in diffusion doping. These phenomena seems to be the main factors behind the drastic increase of the current density after FP in the low injection (ohmic) region of Fig. 5.3-a and Fig. 5.4-a. In these figures, the matching of the I-V curves before and after FP at high forward voltages indicates that the current limiting bulk series resistance effects remain almost unchanged during FP. Since the silicon rich portions are interpreted to become highly conductive after FP, the structure of the residual highly resistive a-SiN_x:H matrix should be preserved. In Fig. 5.4-b, the energy distribution of EL after FP

almost does not change, which implies that the luminescent centers are not seriously modified during FP. Therefore, EL emission both before and after FP seems to be related mostly to a-SiN_x:H matrix. The enhancement of EL intensity after FP can be attributed to the efficient carrier injection by nc-Si clusters towards a-SiN_x:H matrix.

Taking all the above observations into account, the band diagram of the formed *pin* structure may be given as in Fig. 5.7. Here, the band diagram for the applied forward bias of 7 V is scaled using the electron affinities together with the energy gaps of the doping layers, a-SiN_x:H film and nc-Si clusters. The nc-Si grain size is shown to decrease from *n*⁺ side towards *p*⁺ side; i.e. in the region *d*₁, the nc-Si size is expected to be the largest due to the highest local heating. The nc-Si grain size may be considered to be moderate in *d*₂, while

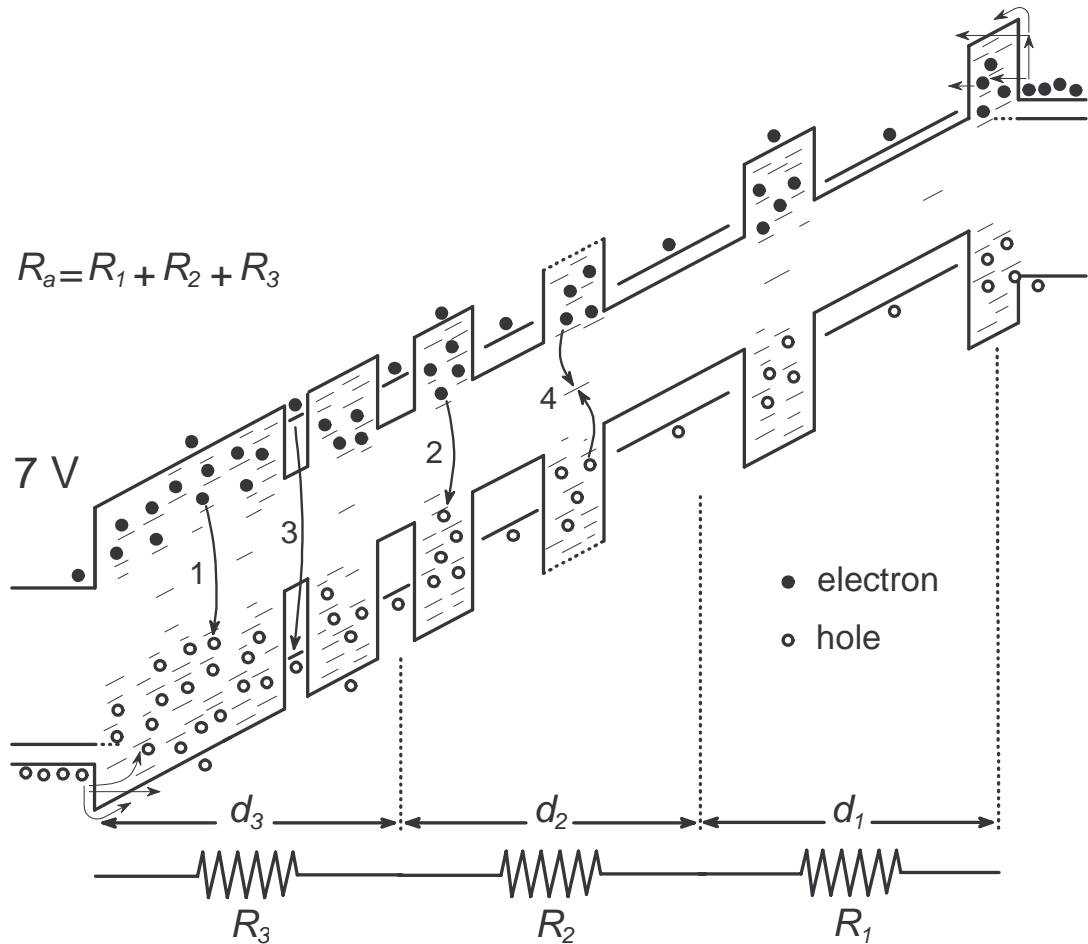


Figure 5.7: Possible energy band diagram of the diode D2 after the forming process. The quantum wells represent the nanocrystallites and the dashes are used for the energy levels. *d*₁, *d*₂ and *d*₃ are the regions from low to high crystallization corresponding to average resistances *R*₁, *R*₂ and *R*₃ respectively. The numbered arrows indicate possible recombination ways.

their size in d_3 should be relatively small or even negligible depending on the gradient of the heat from n^+ to p^+ side (Fig. 5.7). The ground state energy level of the nanocrystallites, ΔE_{nc} , is determined by their sizes according to the quantum confinement effect, QCE. Possible recombination mechanisms are indicated by numbers in Fig. 5.7 with the order of decreasing probability and are described as follows:

1. Since the volume of the amorphous tissue is the largest in d_3 , the charge carriers, mainly the holes, should have the lowest mobility close to p^+ layer. The holes injected from p^+ layer may recombine radiatively with the electrons that are injected from n^+ layer and transported with high mobility through the nanocrystallites toward d_3 .

2. Although the majority of the holes is expected to be accumulated at the p^+/i interface, some portion of them is transported towards n^+ layer. Similar to the electrons, the hole mobility is enhanced during their transport within the nanocrystallites. Therefore, the holes also spend most of their transport times within the resistive a-SiN_x:H matrix and recombination of EHPs occurs whenever electrons and holes come across in the real space.

3. Even if the charge carriers spend much less time in the nanocrystallites during their transport across the bulk of the intrinsic layer, the radiative recombination is also probable in these islands. However, the indirect nature of c-Si must be kept in mind as another factor increasing the radiative life time and decreasing the probability of the radiative recombination therein despite the relaxation of the momentum conservation law by QCE.

4. The charge carriers may also recombine through the deep states of both a-SiN_x:H and nc-Si.

Indeed, the source(s) of luminescence in nanostructured materials like porous silicon (PS) and nc-Si/dielectric is (are) in debate [44, 47, 87–91]. The main controversy is whether the luminescence originates from the radiative recombinations within the nanocrystallites. Since the charge carriers are confined in a finite volume, particle-in-a-box phenomenon suggests that their band gap widens inversely proportional to the size of the nanocrystallite due to the energy quantization. In relation to the confinement in real space, the momentum space eigenvalues become uncertain. However, this real space confinement in the nanocrystallites of size >1.5 nm does not seem enough to cause sufficient momentum uncertainty that would break the indirect nature of c-Si [90]. In addition, the radiative lifetime within nc-Si approaches to that within c-Si (ms) when their size exceeds ~ 2 nm [92]. The observation of visible luminescence from PS even with 200 nm thick Si walls contradicts with the expectation of luminescence from the Si crystallites due to QCE [88]. On the other hand, many researchers verified by

TEM, Raman, ESR, X-ray diffraction and XPS measurements that the luminescing PS also contains amorphous phase (see [88] and references therein). Heath *et al.* reported visible PL from various samples containing 10-30 nm c-Si and/or a-Si nanoparticles and found that the PL energy was independent of their size but depended on the crystalline/amorphous volume ratio of the particles [93]. Furthermore, the Raman spectra of luminescing PS indicated the existences of both amorphous and crystalline phases, and Perez *et al.* concluded that the source of PL was the amorphous layer [94]. Milewski *et al.* also observed a dual phase character in nc-Si/a-SiO_x systems [89]. High resolution TEM photograph of the Si nanoparticles exhibit 1.5 nm a-Si coating around the highly crystalline cores. They reported that the PL energy was independent of the particle size. In order to investigate further, they dropped concentric nitric acid on their samples. Nitric acid is known to react with the siloxene (Si₆H₆O₃) species while it does not react with Si. The unchanged PL spectra indicated that siloxene, which was suggested to be a possible PL source, was not responsible for the emission. In the light of their experiments, they believed that a-Si layer covering the nc-Si cores might be the suspect.

The above discussion implies that radiative recombination would be most probable in the amorphous matrix considering the possible distribution and mobility of the charge carriers. Since the refractive index decreases with increasing N content, the Coulomb interaction is also enhanced between the electrons and holes in the amorphous matrix. This was shown to reduce the radiative lifetime for the samples with higher N/Si ratio [44,47]. Moreover, density functional theory (DFT) calculations showed that the lowest radiative lifetime and the highest radiative recombination probability were reached when N bridges two Si atoms at the surface of the clusters, replacing the Si-H bonds in silicon rich silicon nitride films [87].

The above interpretations deal with the measurements observed after FP. However, the instant at which FP starts should also be considered for better understanding of the phenomenon. Due to the well known columnar growth of the PECVD nc-Si:H films [95], the surface of the 50 nm n^+ nc-Si:H should be rather rough. Since the multiatomic sputtered species of ITO at room temperature have very weak surface migration, their step coverage on the rough n^+ nc-Si:H is not likely to be efficient. Therefore, the n^+ /ITO interface may be regarded as consisting of many point contacts indicated by arrows in Fig. 5.8-a [96]. In addition, possible lateral nonuniformity along the *pin* structure may render some regions of the film more defective. The actual current density through the point contacts is not uniform. This microscopically nonuniform current density may cause nonuniform heating of the diode. At some voltage level (e.g. forward stress of 8 V), the local temperature at some of these regions rises so

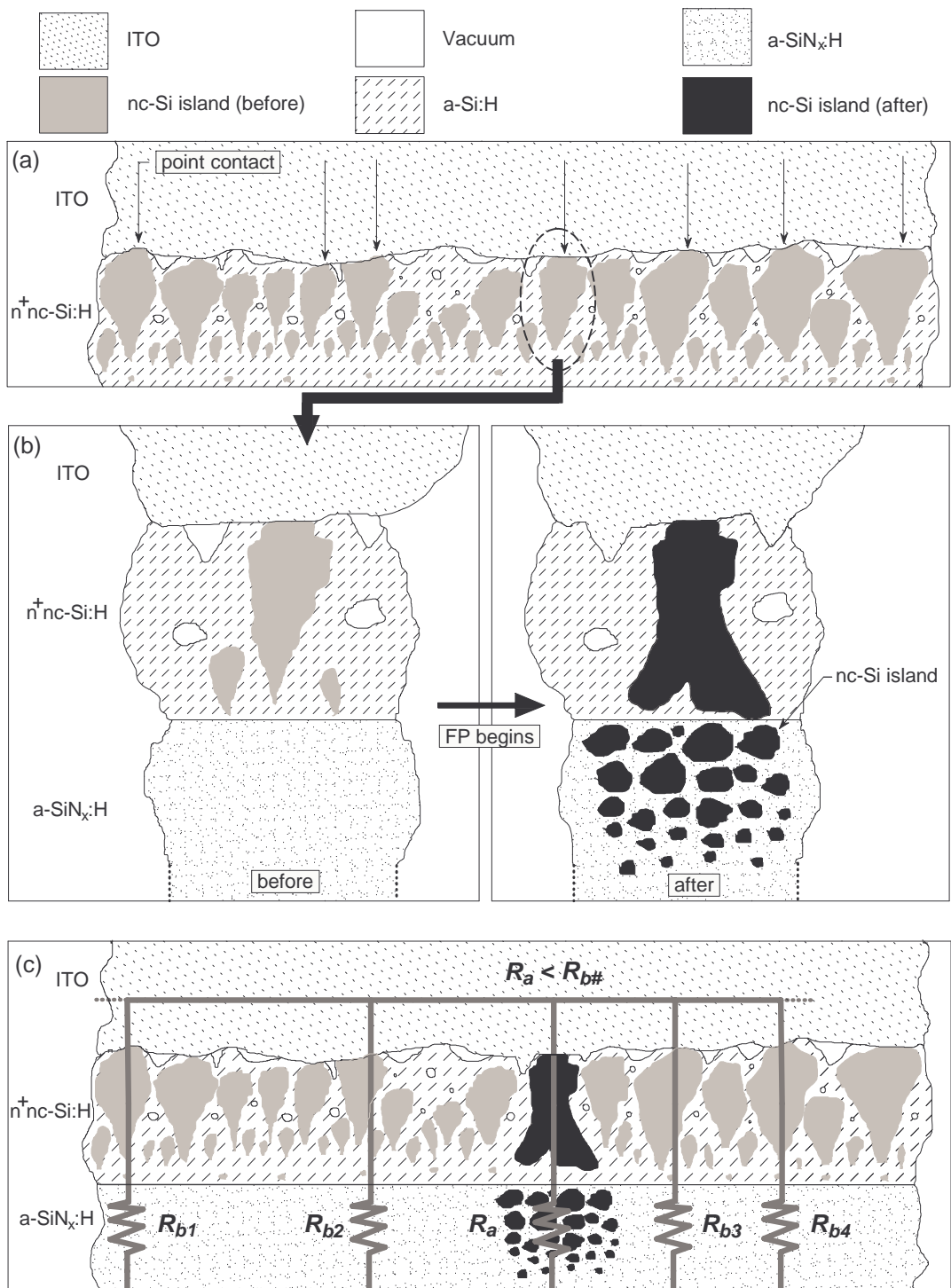


Figure 5.8: (a) Point contacts at n^+ /ITO interface due to the rough surface of n^+ nc-Si:H. (b) FP initiation at one of the point contacts followed by the formation of nc-Si islands within the intrinsic layer. (c) The resistance of the formed region, R_a , is less than the parallel resistances of the fresh parts of the diode, $R_{b\#}$.

much to allow possible transformation from amorphous (higher energy) to crystalline (lower energy) phase of the a-Si:H islands present in the intrinsic layer (Fig. 5.8-b). The eventual temperature rise in this work during FP was verified by the XRD measurements (Fig. 5.6). The formation of nc-Si:H grains enhances both the mobility and the density of charge carriers when compared to those within a-Si:H islands. Consequently, the conductivity of the formed region increases by several orders of magnitude. Considering the formed filamentary conductive region and the residual fresh part of the diode as parallel resistors, the main portion of the current would prefer to flow through the conductive line (Fig. 5.8-c). Then, the current density at this region (R_a) would be drastically higher especially at low voltages where Ohm's law is valid (see forward I-V curves in Fig. 5.4-a). However, since the current flow through the formed region (R_a) is space charge limited above ~ 2 V, some fraction of the injected carriers would be prevented from flowing through this conductive line. Instead, the current density at high voltages would be distributed throughout the whole diode area (R_a and $R_{b\#}$). Still, the current flow would rather be concentrated around the initially formed region as the improvement of the n^+ /ITO contact quality is prospective thereabouts (R_{b3}). When the applied forward voltage stress exceeds ~ 12 V, the current density close to the initially formed region (R_{b3}) is high enough to induce sufficiently high temperatures and to create new nanocrystalline conductive regions. Holding the high forward voltage stress on, the current flow would again be concentrated around the previously formed regions (R_{b4}) due to the same reasons. If the voltage stress is high enough, the process would continue until all the resistive portions of the diode is transformed into the conductive nanocrystallites. Moreover, the heat produced during FP propagates laterally to the surrounding regions and well contributes to transform them since ITO is a relatively heat resistive material.

5.3.2 Electrical characteristics of formed pin diodes

5.3.2.1 Low field regime

The temperature scan of the forward bias I-V characteristics of a formed a-SiN_x:H based *pin* diode D2 between 140 K and 300 K is given in Fig. 5.9. Since the I-V curves are very sensitive to any mechanical vibrations, the measurements were taken after the rotary pump and the compressor of the cryostat were shut. Each temperature was always stabilized before the measurements were started. The current transport is ohmic below 0.2 V. For each T , the conductivity of the formed diode was found from the ohmic region of the I-V curves and its

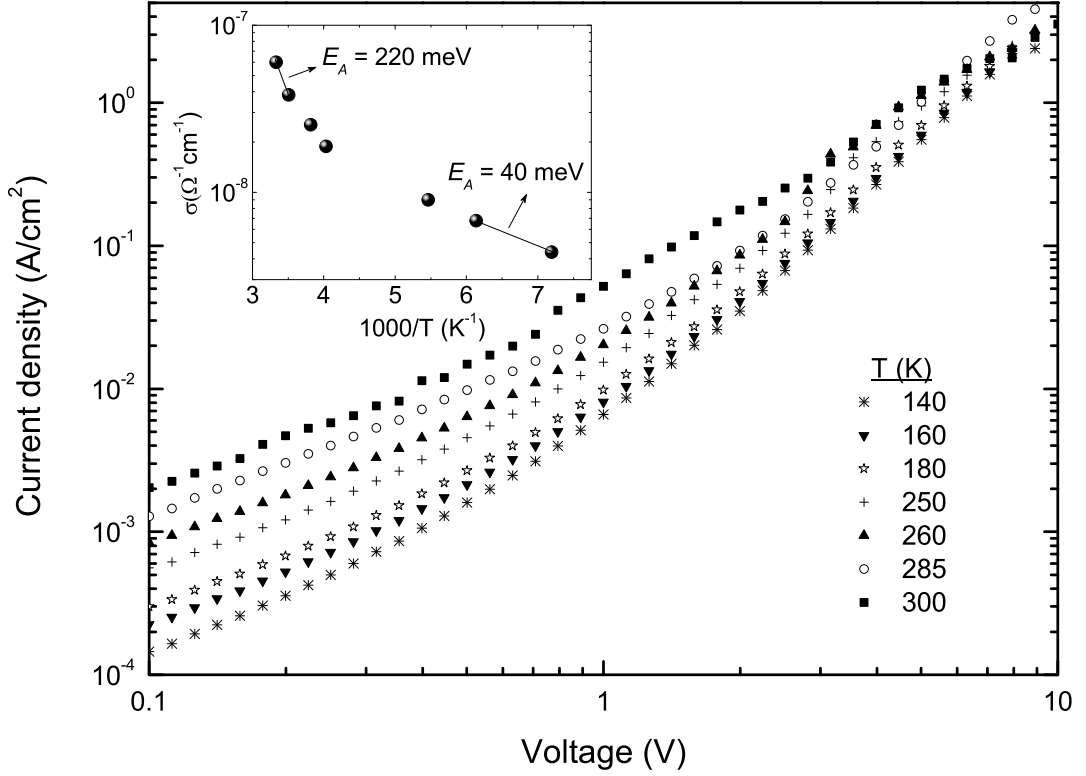


Figure 5.9: Temperature dependence of the forward I-V characteristics of the diode D2 after the forming process. The inset shows the Arrhenius plot of the conductivity with two possible activation energies indicated.

T dependence is given in the inset of Fig. 5.9 through the Arrhenius plot. The conductivity is slightly temperature activated and the activation energy is temperature dependent. If linear fits are imposed for this plot, the activation energy would be around 40 meV at low temperatures and around 220 meV at higher temperatures. At the first glance, on one hand, these activation energies are too low for a wide gap a-SiN_x:H. On the other hand, they are too high for the consideration of hopping transport through the deep levels around the midgap. However, it should be noted that the energy gap of a-SiN_x:H is invaded by tail and deep states. Besides, new electronic states inside the forbidden gap might be introduced during FP due to the formation of nanocrystalline silicon islands. A more generalized model for the hopping transport, taking the occupation of the whole intraband states into account, can recover the contradiction [97, 98]. In this respect, a charge carrier may tunnel from an initial localized state E_i to an empty localized state E_j with the transition rate r_{ij} given as:

$$r_{ij} = \nu_0 \exp\left(-\frac{2\alpha R_{ij}}{R_0}\right) \exp\left(\frac{(E_j - E_i)}{kT}\right) \quad \text{if } E_i < E_j \quad (\uparrow) \quad (5.1)$$

$$r_{ij} = \nu_0 \exp\left(-\frac{2\alpha R_{ij}}{R_0}\right) \quad \text{if } E_i > E_j \quad (\downarrow), \quad (5.2)$$

where ν_0 is the attempt-to-escape frequency, R_{ij} is the distance between the aforementioned localized sites, R_0 is the characteristic localization length of the wavefunction around the trap site as provided in Eq. 1.3. Together with the Fermi-Dirac statistics, the transition probability is $P_{ij}=f(E_i)[1 - f(E_j)]r_{ij}$. The detailed balance requires downward and upward hopping probabilities between any pair of localized states above E_F to be equal at steady state. Therefore, the equilibrium conductivity can be determined within a factor of 2 by the consideration of only the downward transitions. In this regard, a charge carrier is thermally excited from an occupied state around E_F to an empty level of energy E . Then, it creates a current flux in the direction of the applied field F by hopping downward to a nearest level of energy E' such that $E_F < E' < E < E_\mu$. The average concentration of such states available for transition is:

$$\bar{N} = \int_{E_F}^E N(E') [1 - f(E')] dE', \quad (5.3)$$

where $N(E')$ is the total density of energy states inside the forbidden gap: sum of the exponential tail states and gaussian deep levels above E_F . The differential current density with respect to energy can be expressed as:

$$\left. \frac{\delta J}{\delta E} \right|_E = qR \left. \frac{dr}{dE} \right|_E \Delta n \quad \text{with} \quad \Delta n = N(E) f(E) \Delta E. \quad (5.4)$$

Here, $\Delta E = qFR$ is the increase in the carrier energy due to the applied field and $R = [\frac{4\pi}{3}\bar{N}]^{-1/3}$.

The differential transition rate $\left. \frac{dr}{dE} \right|_E$ is derived from Eq. 5.2 and Eq. 1.3 as:

$$\left. \frac{dr}{dE} \right|_E = r \ln\left(\frac{r}{\nu_0}\right) \left[\frac{4\sqrt{4\pi}}{9} R^3(E) N(E) - \frac{R_0^2 m}{\hbar^2} \right] \quad \text{if } R_0 = R_0(E) \quad (5.5)$$

$$\left. \frac{dr}{dE} \right|_E = r \ln\left(\frac{r}{\nu_0}\right) \frac{4\sqrt{4\pi}}{9} R^3(E) N(E) \quad \text{if } R_0 = \text{constant}. \quad (5.6)$$

Finally, the differential conductivity follows from Ohm's law as:

$$\left. \frac{\delta \sigma}{\delta E} \right|_E = q^2 R^2 N(E) f(E) \left. \frac{dr}{dE} \right|_E. \quad (5.7)$$

The above model may be applied to amorphous semiconductors, particularly of wide gaps, in order to explain (or assess) the activation energies possibly lower than expected. The current across these semiconductors may be transported through all the possible localized [97] and/or deep states [98] with the probability defined by their density and occupancy. In the case of the formed *pin* diodes, this model should be slightly modified.

The quasi-Fermi levels of *p* and *n* sides are, respectively, located closer to the valence and conduction band tails of the intrinsic layer (Fig. 5.7). Also, considering QCE, the quasi-Fermi levels should be in the proximity of the nanocrystallite fundamental levels. Therefore, holes from *p* side and electrons from *n* side might be easily injected, respectively onto the valence and conduction band fundamental levels of the crystallites. Once the carrier enters the quantum well (QW), its mobility is enhanced and its real space wavefunction is more or less delocalized. Then, by the effect of the applied field, this carrier may be assumed to reach the QW/amorphous tissue boundary immediately, with very low probability of recombination. Next, its transport through the localized states of the amorphous matrix is to be considered with the hopping mechanism introduced above. This modified model is schematically depicted in Fig. 5.10-a for the electron transport of D2 (similar mechanism for holes should be simultaneously present). The carrier may be directly injected to a deeper localized level via step #1. It may be also injected to a moderately shallow level subsequent to a thermal excitation, i.e. step #2. Furthermore, its thermal excitation to reach very shallow levels or even the band edge is also possible, i.e. step #3.

The density of localized states in the case of formed diodes may consist of several kinds, since all the bonds within the a-SiN_x:H tissue should be affected due to the crystallization of the Si rich regions at high local temperatures. Still, the exponential behavior may be assumed as a convolution of all possible bond distortions from the band edge (most probable) through deeper energies (less probable) (see Fig. 5.10-b).

The thermal excitation probability from the nanocrystallite to an empty localized state reaches unity at deeper energy levels (Fig. 5.10-c). However, the tunneling between these deeper localized states is very low as the hopping rate decreases exponentially with increasing separation (Eq. 5.2). With a similar argument, although the hopping rate is higher at shallower states, the probability of thermal excitation to these levels is very low since their occupancy decreases exponentially with increasing energy difference from the occupied initial state. In this regard, the differential conductivity is expected to give a maximum slightly above the fundamental level of the nanocrystallite.

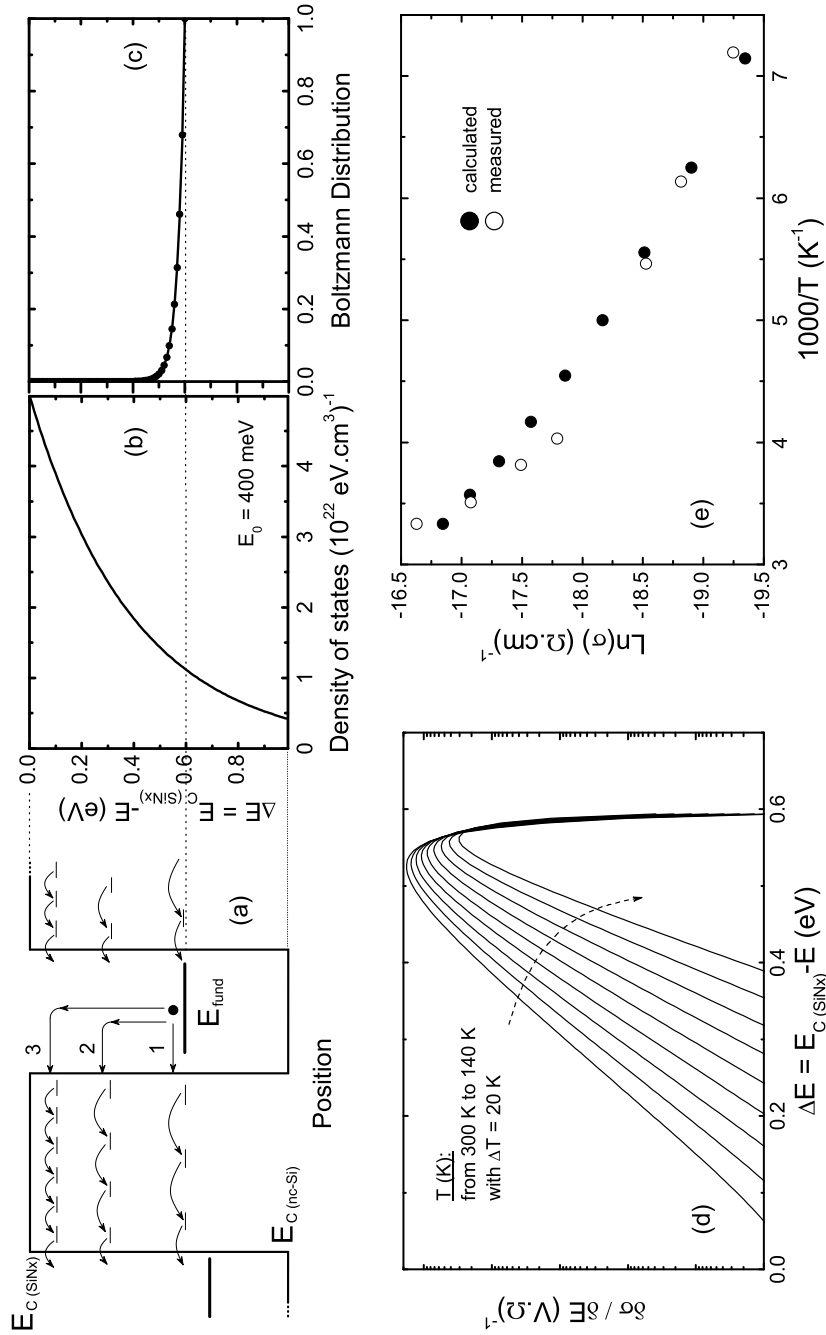


Figure 5.10: (a) Si nanocrystallite surrounded by a-SiN_x:H matrix in D2. Dashes represent the localized states and the numbered arrows are used for the possible ways of tunneling. E_{fund} shows the fundamental level of the crystallite. $E_{C(SiNx)}$ and $E_{C(nc-Si)}$ stand for the conduction band edge of a-SiN_x:H and that of the Si nanocrystallite, respectively. (b) Exponential band tail states with the characteristic energy of $E_0=400 \text{ meV}$ measured from $E_{C(SiNx)}$. (c) Probability of thermal excitation from E_{fund} to higher energies at 300 K. (d) Differential conductivity versus energy plot for various temperatures. (e) Arrhenius plot of the conductivity using both the calculated and the measured data.

With plausible values of conduction band edge DOS (h_0^c), subgap absorption tail (E_0) and fundamental level energy (E_{fund}), the model was applied to the diode D2 for various temperatures (Fig. 5.10-d). Instead of Fermi-Dirac distribution, Boltzmann factor was used for occupancy in Eq. 5.7, since the energy levels of interest are well above the intrinsic E_F of the sample. At low T , the Boltzmann factor decays so fast that the carrier is not likely to be excited to the higher levels. At elevated temperatures, the decay of the Boltzmann factor weakens and the occupancy of the higher energy levels increases.

The conductivity can be found by the integration of the differential conductivity with respect to energy, i.e. the area under the curves of Fig. 5.10-d. The calculated conductivity is given in Fig. 5.10-e via the Arrhenius plot. The good agreement of the calculation with the measurement implies that such low and temperature dependent E_A may be explained by this band-tail hopping model.

The same calculation procedure was applied to the diode D3 whose I-V characteristics are provided in Fig. 5.11. The T dependent behavior of the I-V curve is similar to that of D2, where the thermally activated ohmic transport at low bias gradually transforms into field enhanced carrier emission mechanism(s) and finally, almost T independent SCLC becomes dominant. The ohmic region of D3 is valid until higher bias (≤ 0.5 V) than that of D2 (≤ 0.2 V). The current density at a particular voltage is higher when compared with D2. The T dependence of the activation energy of D3 seems to be weaker with a value $E_A \approx 45$ meV, which almost coincides with the lowest E_A of D2.

Since the nitrogen amount in the intrinsic layer of D3 is greater than that of D2 (see Table 5.1), the resistivity of D3 is expected and was verified experimentally to be higher than that of D2 before FP. Therefore, the local Joule heating during FP should be higher in D3. This induces nanocrystallites of larger sizes especially near the n side of the D3 intrinsic layer when compared with D2. Hence, contrary to the situation before FP, the Ohmic resistivity of D3 after FP would be lower than that of D2 as measured. Taking the slightly T dependent low E_A of D3 into account, DOS induced during FP might be larger in D3. The result of the band-tail hopping calculations for D3, where slightly greater h_0^c and E_0 were used, is given in appendix F.

5.3.2.2 Intermediate field regime

The I-V characteristics of the diode D2 in Fig. 5.9, deviating from the ohmic behavior, were tested by several conduction mechanisms (e.g. Poole-Frenkel emission, Fowler-Nordheim

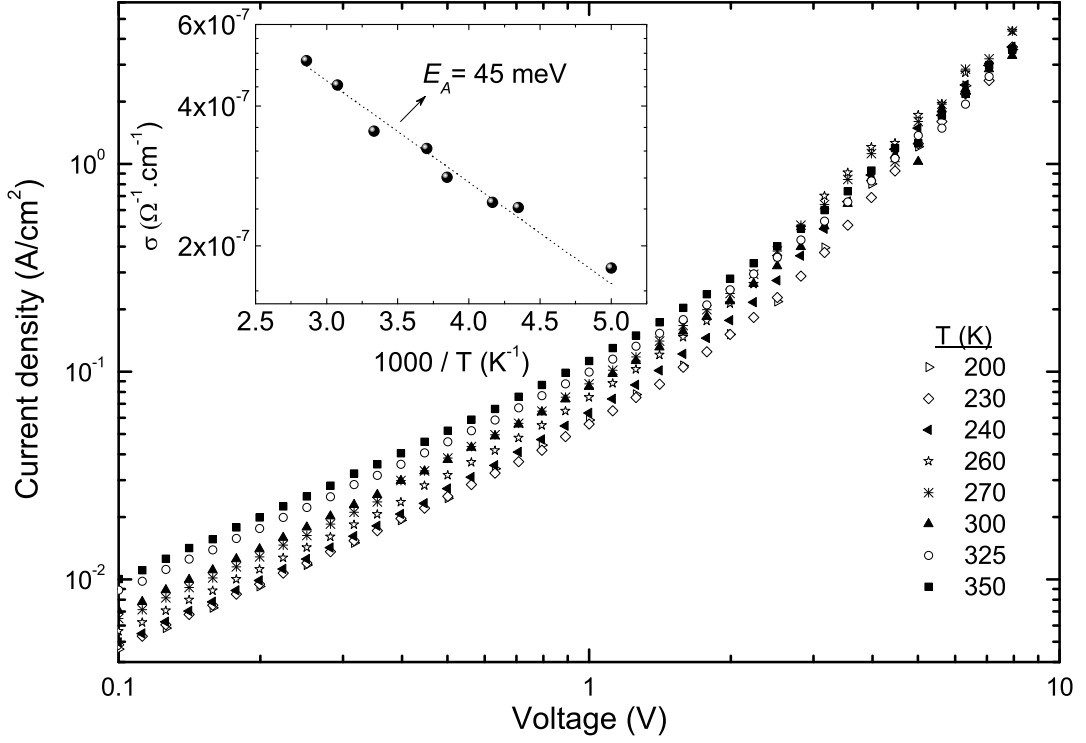


Figure 5.11: Temperature scan of the forward I-V characteristics of the formed a-SiN_x:H based *pin* diode D3. The temperature dependence of its conductivity through the Arrhenius plot is given in the inset.

tunneling, space charge limited current (SCLC), etc.). In the region between 0.2 V and 5 V, the following field enhanced conduction, which is usually referred to as Poole-Frenkel emission, seems dominant [99]:

$$J \propto F^a \exp\left(-\frac{q\left[\Phi_b - \sqrt{(qF/\pi\epsilon)}\right]}{kT}\right), \quad (5.8)$$

where $a = \pm\frac{1}{2}$ or 1, Φ_b is the potential depth of the trap level and ϵ is the electrical permittivity of the semiconductor. The exponent a is related to the behavior of the detrapped carrier prior to its retrapping by one of the next trap centers. For instance, in the 3D model of Jonscher [99], the probability of the charge carrier to escape not only in the direction of the applied field, but in all directions was considered and a was found to be $-\frac{1}{2}$. This value of the exponent was also found when a detrapped charge carrier was assumed to be captured by the first trapping center [100]. If the detrapped carriers travel a distance proportional to the applied field (Ohm's law) as in the crystalline (or semi-crystalline) semiconductors, Eq. 5.8 becomes the widely used Poole-Frenkel equation with the exponent $a=1$ [99, 101]. For

amorphous semiconductors, where the random diffusion process may be assumed, the velocity of a detrapped carrier is proportional to $F^{1/2}$ with $\frac{1}{2}$ being the exponent a in this case [101].

The field dependence in the exponential factor of Eq. 5.8 is taken as $F^{1/2}$, which is associated with the barrier lowering of a Coulomb potential under the applied field F . Coulomb potential requires an empty charged state like a donor or acceptor. However, it would be improper to assume the existence of donor-like sites within the band tails. Jonscher [99] discusses that it would be sufficient if the external ‘hill’ of the potential can be taken as Coulombic, while the inner well is kept steeper. He also suggests that the Poole-Frenkel emission from a trap is not necessarily into the relevant band, but rather into the higher energy band tails. This suggestion resembles the field assisted hopping of a charge carrier out of a neutral empty level to the localized band tails followed by its subsequent downward hopping [102, 103]. In the model of Apsley *et al.*, a mobility definition was introduced using the hopping probability to the nearest neighbor available site. The conductivity expression was reached by the integration of this mobility over energy. With the assumption of flat and uniform DOS, the exponential field dependence of conductivity was found to be F^2 at low fields and $F^{1/4}$ at very high fields. It was mentioned that $F^{1/2}$ dependence would be expected

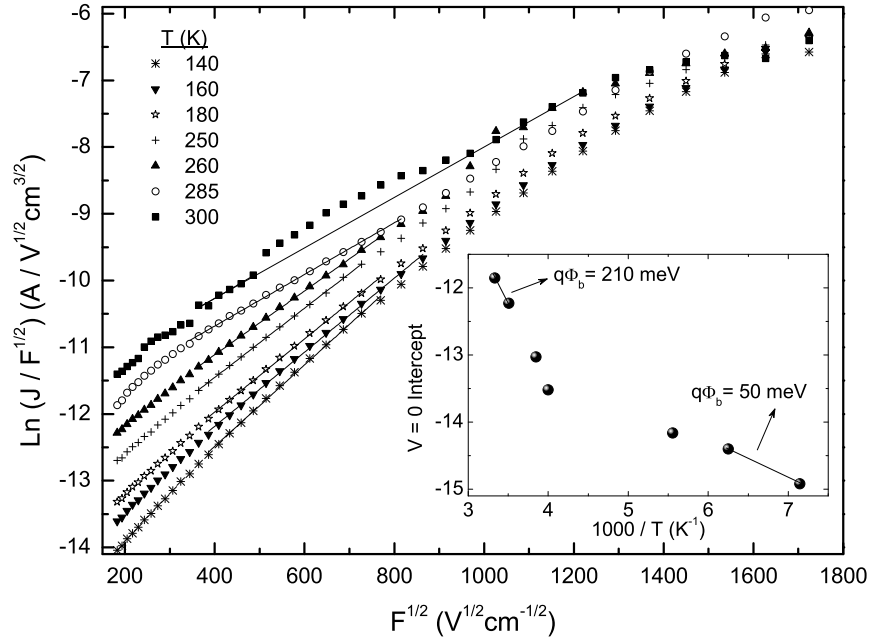


Figure 5.12: Poole-Frenkel plot of $\ln(J/F^{1/2})$ versus $F^{1/2}$ for D2 after the forming process at different temperatures. $V=0$ intercept of the main plot versus $1000/T$ with indicated energy depths of the trap level.

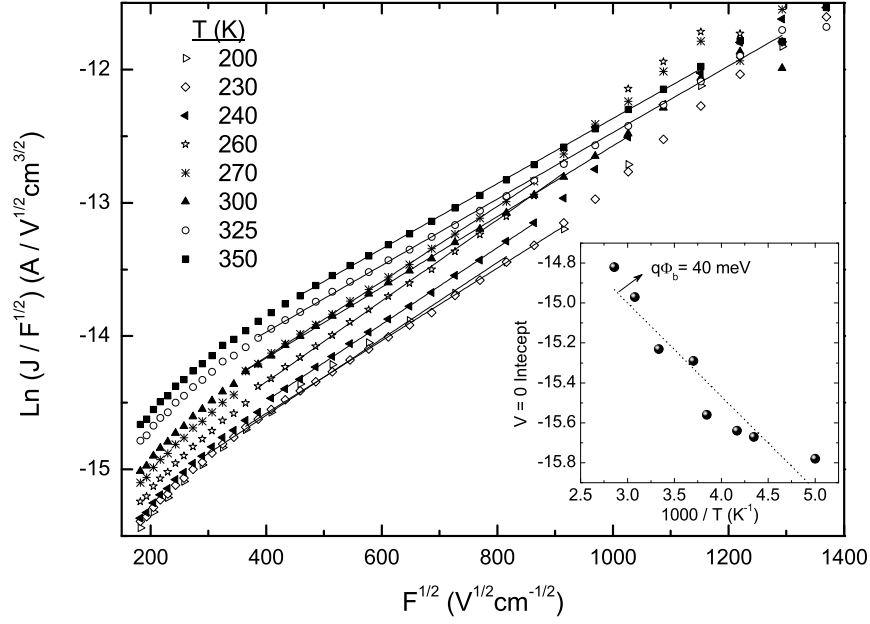


Figure 5.13: Poole-Frenkel plot of $\ln(J/F^{1/2})$ versus $F^{1/2}$ for D3 after the forming process at different temperatures. $V=0$ intercept of the main plot versus $1000/T$ with indicated energy depths of the trap level.

at intermediate fields [104]. The $F^{1/2}$ dependence in the diodes D2 and D3 is valid around 10^5 Vcm^{-1} , which is in the limit of intermediate/high fields (for D2 see Fig. 5.12; for D3 see Fig. 5.13). Although the band tail DOS can not be considered flat, it is rather slowly varying, since the characteristic energy E_0 is higher than 0.4 eV in these diodes.

In this respect, $F^{1/2}$ dependence in Fig. 5.12 and Fig. 5.13 may arise either from detrapping out of a potential well exhibiting Coulombic behavior at least around the external ‘hill’, or from hopping out of a neutral empty level. The latter seems to be the probable case, since the empty band tails are neutral states which present Dirac potential and it is difficult to admit any Coulombic behavior therein. Furthermore, the coincidence of the apparent activation energy E_A determined from the Ohmic region, and the barrier height $q\Phi_b$ inferred from Eq. 5.8, points out that the current is limited by the carrier emission out of the same kind of energy levels at low and intermediate fields, i.e. phonon and field assisted tunneling from E_{fund} to the band tails.

5.3.2.3 High field regime

The current densities in Fig. 5.9 tend to match on a single curve at higher fields for all T . In other words, when the thermal activation of the current density is considered, it is gradually

reduced with increasing voltage (see [104] for a similar behavior in a-C films). The high field I-V characteristics of D2 is given in Fig. 5.14 via the Fowler-Nordheim plot, whose linear slope supplies the effective barrier for the carriers to tunnel [105]. The linearity is observed only at lowest temperatures of $T=140$ K, 160 K and 180 K with respective barrier heights of $q\Phi_{FN}=15$ meV, 17 meV and 19 meV (at higher temperatures, the current is rather space charge limited with negligible thermal activation). The field enhancement of the current density may be associated with easier carrier emission from the traps or with improved carrier mobility. As indicated in the inset of Fig. 5.14, both are possible. Due to the huge band bending at high applied fields, the potential energy of the empty localized states to be hopped onto decreases relative to E_{fund} of the occupied potential well. In this case, the thermal excitation energy to hop onto the band-tail states is lowered when compared to the case of low/intermediate fields; i.e. easier carrier emission. Moreover, once the carrier hops out of the potential well, DOS of the empty localized states of the same potential energy increases

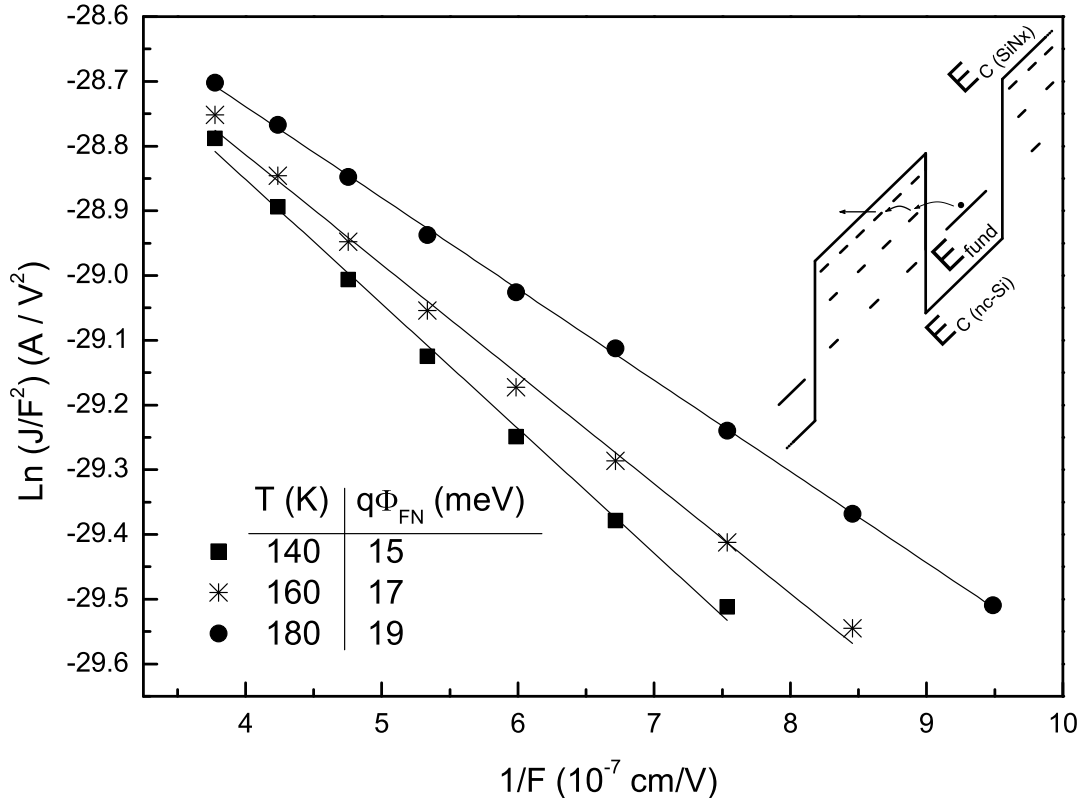


Figure 5.14: Fowler-Nordheim plot for the formed diode D2 using the I-V data measured at the lowest temperatures: 140 K, 160 K and 180 K. Inset shows the possible field-enhanced carrier transport mechanism.

with position. In other words, the separation between the available sites of same energy decreases as the carrier transport progresses. Consequently, the hopping rate increases each time the carrier tunnels to the nearest neighboring state; i.e. enhanced mobility. The effective barrier height slightly increases with temperature arising from the same reasons mentioned for the ohmic E_A in Fig. 5.10.

The above field-enhanced barrier lowering effect is not observed at higher temperatures ($T > 180$ K) in the high field regime. Due to the better carrier injection efficiency in this case, the density of injected carriers may become comparable to that of the available density of empty energy levels. In the steady state, the space charge accumulated within the bulk of the film would impede the transport of the behindhand carriers. If the transport is limited by the space charges of a single energy level E_t , the measured current would be proportional to the square of the applied voltage, i.e. $J \propto V^2$. Instead, if the space charge accumulation occurs at exponentially distributed band tails, the I-V relation is obtained as $J \propto V^a$ with $a \geq 2$ [106]. The latter is the case observed in the formed *pin* diodes at hand (see Fig. 5.4-a, 5.9 and 5.11 where $a \geq 2$ above ~ 2 V). This is consistent also with the band-tail hopping model proposed for low and intermediate field regimes.

5.3.2.4 Memory effect in the formed *pin* diodes

As it was shown above, the current density increases after the diode FP is over. In addition, under the forward bias, the intense light emission from the formed diodes is easily observed by naked eye in the dark room conditions. In the reverse bias regime, there is no visible light emission. Also, the I-V measurement sequence affects the diode characteristics in a way that in some cases under the forward bias there is no light emission and the current is similar to that of the reverse bias regime. To clarify these phenomena and to observe any possible memory effects, the I-V measurements have been taken in a systematic way. In Fig. 5.15, the I-V curves of the formed a-SiN_x:H based *pin* diode (D2) can be seen. The measurements in the forward bias regime (forward-1) have been found to be repeatable and visible light emission always accompanies. However, the diode exhibits hysteresis when the measurement is taken in the reverse bias regime, such that the current density for decreasing reverse bias (reverse-3) is about two orders of magnitude higher than that for the increasing case (reverse-2) especially below 1 V. It is interesting to note that the diode remembers its past when taking a forward measurement (forward-4) subsequent to reverse-3. The I-V curve of forward-4 shows almost the same ohmic behavior with that of reverse-3 and the visible light emission

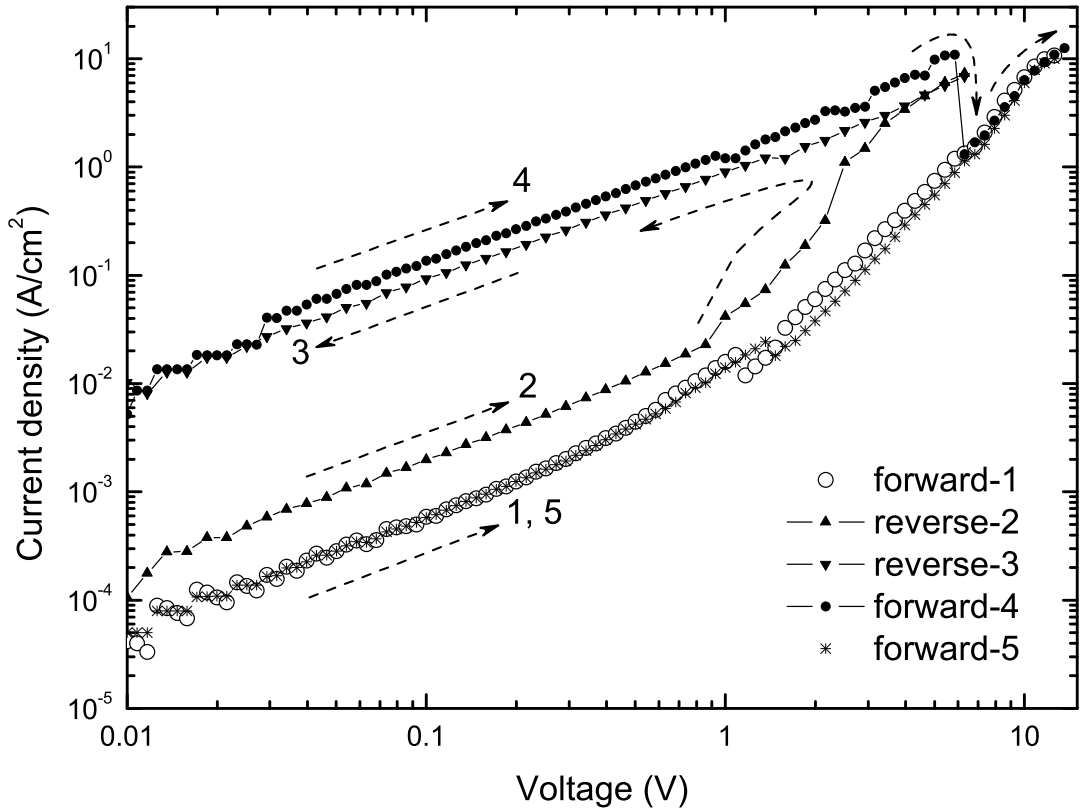


Figure 5.15: Forward and reverse I-V characteristics of a-SiN_x:H based *pin* diode (D2) after the forming process. The measurement sequence and the directions of the measurements are indicated by the numbers and the dashed arrows, respectively.

is absent until ~ 6 V. At this voltage, the current density suddenly drops down and the visible light emission starts. Beyond this voltage, the I-V curve of the original forward measurement, forward-1 and the light emission characteristics are restored. When a subsequent forward measurement (forward-5) is taken, the diode is verified to turn back to its initial state and reproduces the original curve of forward-1. This phenomenon was observed each time the above measurement procedure is repeated and is valid for all formed diodes.

In the previous Fig. 5.15 on the I-V characteristics of a formed a-SiN_x:H based *pin* diode (D2), a sudden drop in the current density was observed when taking a forward bias measurement subsequent to a reverse one. In Fig. 5.16, the kinetics of this drop was studied as a function of the applied forward voltage stress. The measurement was systematically repeated in the dark room for each data point as follows: first, the formed diode got through the charged state by applying a reverse current stress of 6.4 A/cm² for 2 min. Then, it was kept away from any current or voltage stresses for 1 min. Finally, a forward voltage stress was applied. The

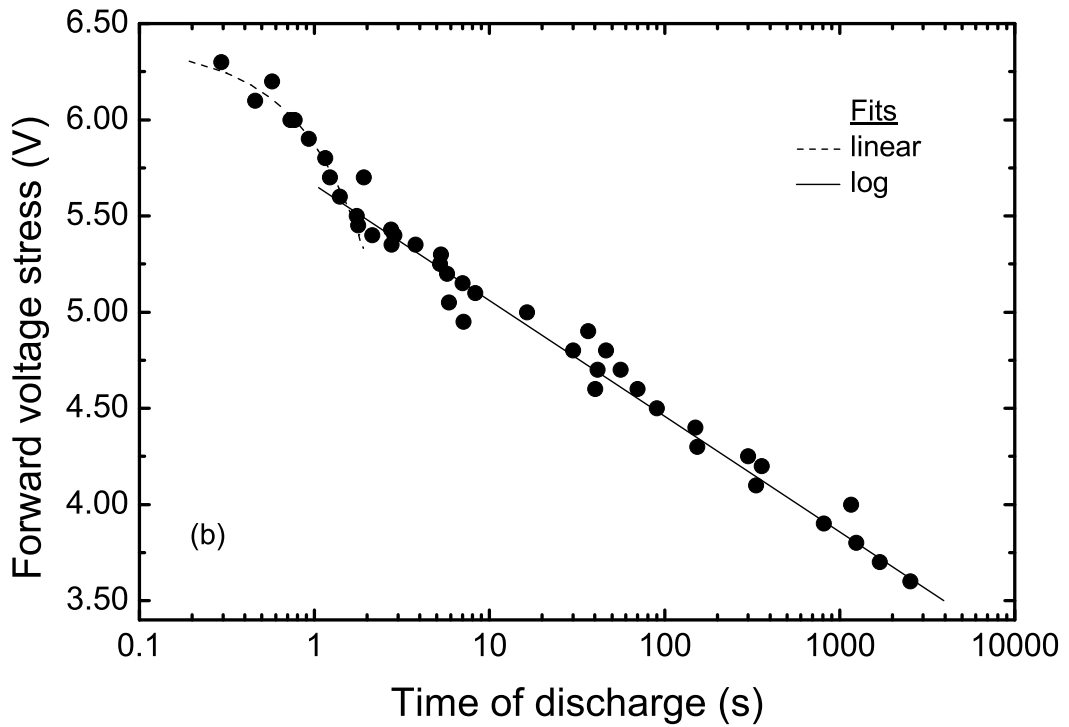
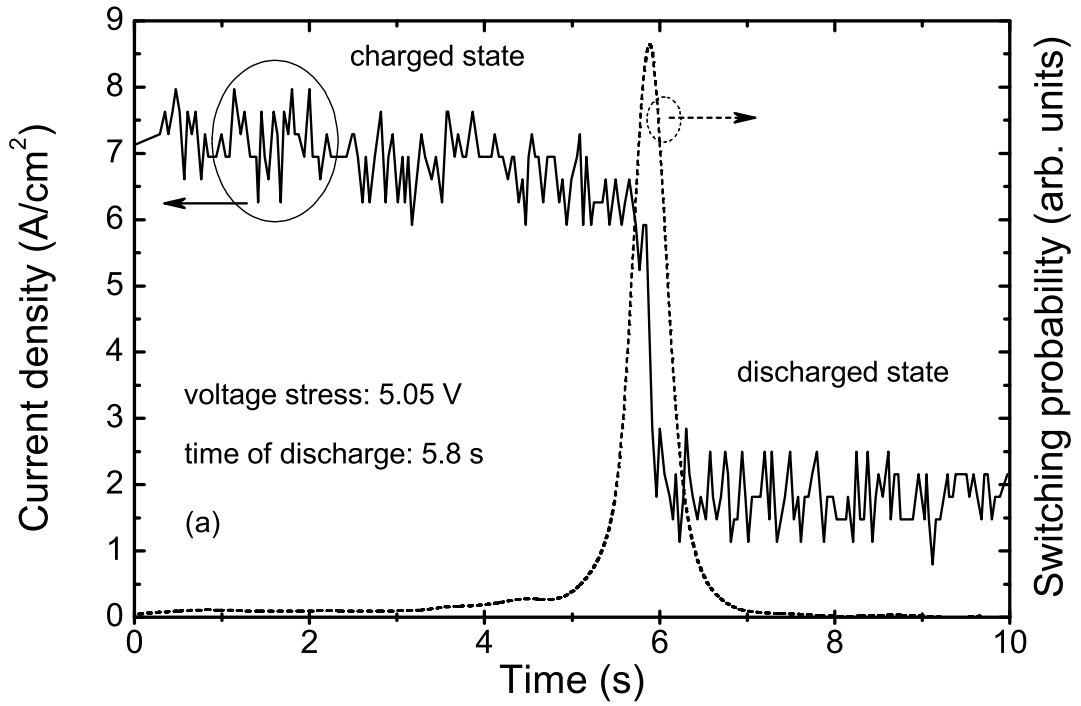


Figure 5.16: (a) Current versus time curve of a formed a-SiN_x:H based *pin* diode (D2) carrying out the charging/discharging moment under a forward bias of 5.05 V. (b) Forward biasing voltage versus charging/discharging time.

current was followed in time and the discharging moment was determined by a computer program. An output of this program is given in Fig. 5.16-a. The current density in the charged state is always higher than that in the discharged state. In addition, the discharging event may be regarded as a sudden phenomenon when the measurement is taken in the time scale of seconds. Therefore, the instant at which the current density suddenly drops was termed as the ‘time of discharge’. In Fig. 5.16-b, the time of discharge has a logarithmic dependence on the applied forward voltage stress below 5.50 V. While the discharging event occurs in less than 10 s after the application of voltage stresses above 5.00 V, it takes up to 1 hour when the voltage stress is reduced down to about 3.50 V. As for the voltage stresses above 5.50 V, the time of discharge seems to have a linear dependence on the voltage stress. Above 6.30 V, the time of discharge could not be determined by the present measurement system as the diode is discharged instantaneously just after the program is run. A possible explanation on this memory effect in formed *pin* diodes can be as follows.

In Fig. 5.17, the energy band diagram near *p* nc-Si:H/a-SiN_x:H heterojunction interface, where the crystallization after FP is rather weak (region *d3* of Fig. 5.7), is depicted. At equilibrium, in the neutral region, all the gap states below E_F are occupied by electrons. In the depletion region, the states above E_M are vacant of electrons, where E_M is determined by thermal emission rates for electrons and holes toward the relevant band edges (Fig. 5.17-(a-1) and (a-2)). Across the depletion region, the free carrier densities may be neglected due to the drift phenomenon by the built-in electric field. Consequently, the occupancy, f_i , of a gap state with energy E is determined in terms of the electron and hole emission rates e_n and e_p , respectively: $f_i = e_p/(e_p + e_n)$. The occupancy/unoccupancy boundary, $E = E_M$, within the mobility gap corresponds to $f_i = 1/2$, which leads to $e_n = e_p$. Using the well known expressions $e_n = \nu_n \exp(-(E_C - E)/kT)$ and $e_p = \nu_p \exp(-(E - E_V)/kT)$, the demarcation level E_M may be expressed as:

$$E_M = E_C - \frac{E_G}{2} + \frac{kT}{2} \ln\left(\frac{\nu_p}{\nu_n}\right), \quad (5.9)$$

where E_C - conduction band edge, E_V - valence band edge, E_G - mobility gap, ν_p and ν_n are the attempt-to-escape frequencies for holes and electrons, respectively. If $\nu_p \approx \nu_n$, then E_M is equal to the midgap. At forward bias, excess electrons, injected into intrinsic layer from *n*-side, propagate (probably by hopping across the localized tail states) towards *p*-side, while excess holes, injected into the intrinsic layer, propagate along the opposite direction.

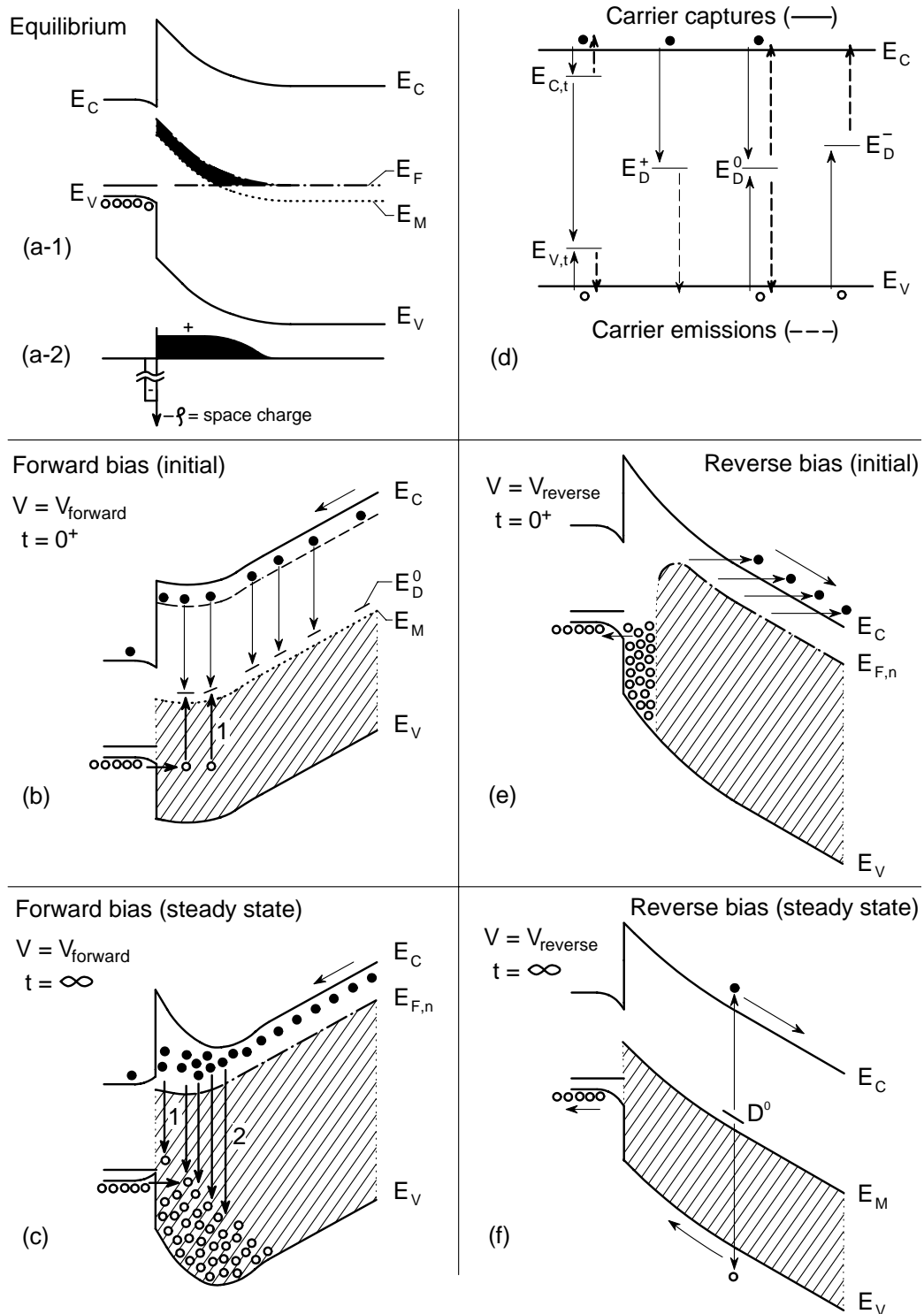


Figure 5.17: Proximity of p/i interface of a heterojunction pin diode. (a-1) Energy band diagram and (a-2) possible space charge under equilibrium. (b)-(c) Recombination and trapping phenomena at forward bias. (d) Schematical localized states and their carrier exchange with the relevant band edges. (e) Detrapping and (f) steady-state generation at reverse bias.

During the first stage of forward bias application (after reverse one), carriers, partly trapped by localized states, partly recombine through them. As holes are relatively slower, the majority of the recombinations (electron/hole meeting) occurs near p/i interface mainly through tail-to-empty dangling bonds (DBs) mechanism (mechanism 1 in Fig. 5.17-b). As time passes, trapped electrons raise the electron quasi-Fermi level, $E_{F,n}$ towards the conduction band edge (Fig. 5.17-c), probably above the doubly occupied DB level E_D^- (Fig. 5.17-d). At steady state, as the majority of DBs is saturated by electrons, they can not capture further electrons. Consequently, tail-to-DB recombination is attenuated and electron-hole recombination occurs through tail-to-tail mechanism (mechanism 2 in Fig. 5.17-c) leading to visible light emission. Parallely, the injected holes near p/i interface may form a net positive space charge, which create a barrier against the further hole transfer, i.e. a space charge limitation of holes is expected (Fig. 5.17-c). If a dc reverse bias voltage is applied, the previously trapped electrons will be progressively detrapped towards conduction band edge (Fig. 5.17-e). At steady state (Fig. 5.17-f), all localized states are emptied up to the demarcation level E_M and the reverse current is established through the neutral DBs generation without visible luminescence as shown in Fig. 5.17-f. Experimentally, after this steady state reverse bias regime, a forward bias voltage was applied and the kinetics of the current (current versus time) was followed as shown in Fig. 5.16-a. After a critical time duration, the current was reduced to a lower value. Before the switching time, the diode may only radiate through mechanism 1 in the near IR region. After the switching, the diode emits throughout the whole visible region including near IR by mechanisms 1 and 2, as depicted in Fig. 5.17-c. This last situation is preserved as long as the diode remains under forward bias. The critical time duration has been found exponentially applied forward bias dependent, as given in Fig. 5.16-b. This behavior is at least qualitatively expected, since large forward biases speed up both the building of positive space charge and the filling of localized states from E_M up to the final $E_{F,n}$.

5.3.3 Electroluminescence from formed pin diodes

In Fig. 5.18, the normalized EL spectra of a-SiN_x:H based formed *pin* diodes (D1) can be seen. The diodes have the same *pin* structure as they were produced in the same deposition set. The only difference is their window electrodes, i.e. Cr (80 nm), Al (80 nm) and ITO (300 nm). Since ITO is also a semiconductor having a band gap of 3.9 eV, one may doubt whether visible light emission is possible from this commonly used transparent window electrode or its interface with n⁺ nc-Si:H. Therefore, this experiment has been performed to make sure

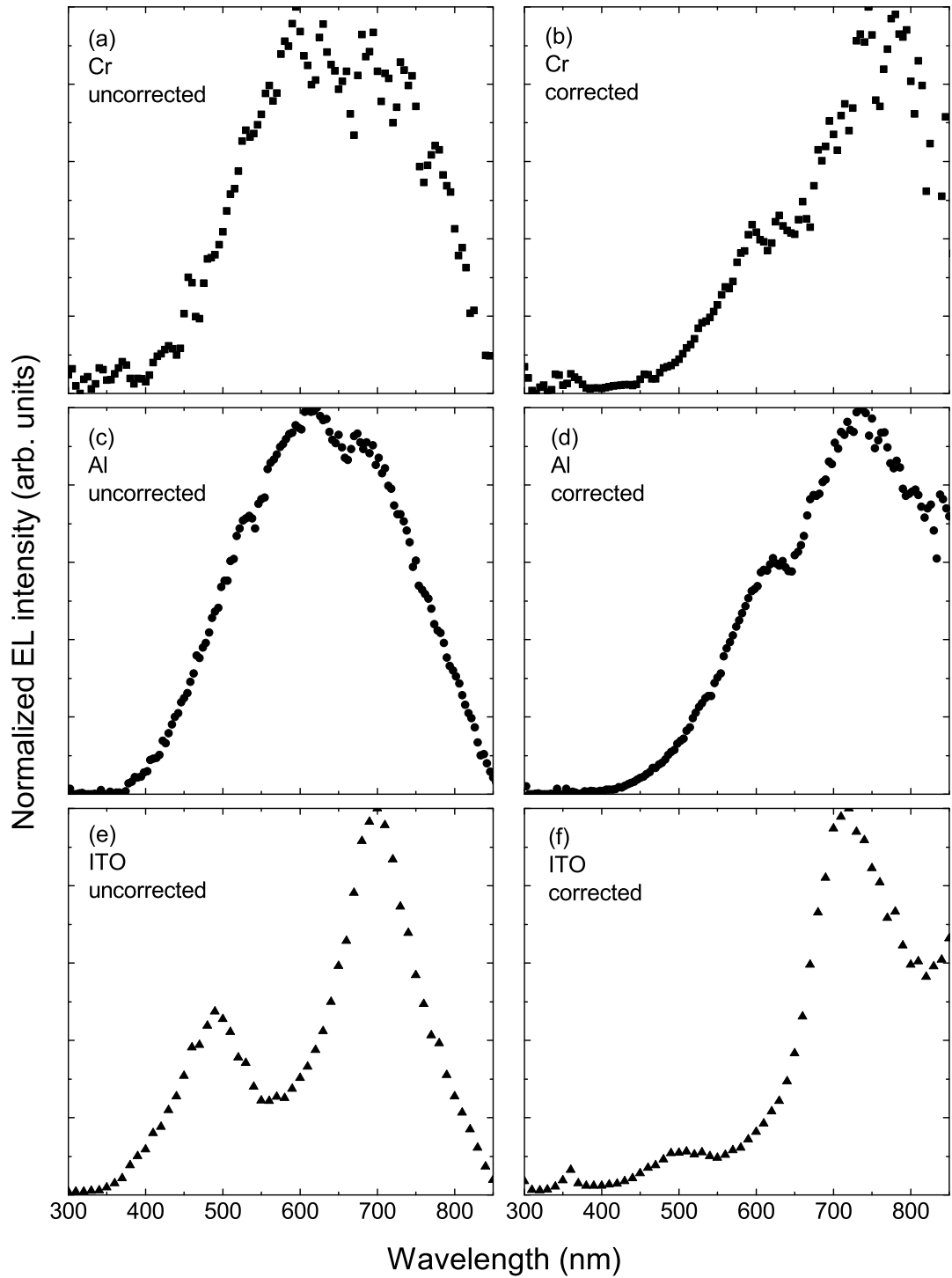


Figure 5.18: (a), (c), (e) Uncorrected and (b), (d), (f) corrected (for the PMT responsivity, appendix D) normalized EL spectra after the forming process of a-SiN_x:H based *pin* diodes (D1) having different window electrodes: Cr, Al, ITO, respectively.

that the emission source is not ITO related. The EL spectra measured from the diodes having Cr and Al window electrodes have almost the same wavelength dependence. However, these spectra differ from that of the diode with ITO electrode. In order to interpret this difference, the optical paths of the emitted light and the emission characteristics through the window electrode surfaces should be considered. ITO has been deposited much thicker than Cr and Al, since it was found that the light emission is uniformly distributed along the whole diode area more easily when the ITO thickness is increased from 100 nm to 300 nm. Considering 180 nm thickness of the *pin* structure, the total thickness of the '*pin*/ITO' composite is 480 nm which may cause several interference fringes when visible light emission is transmitted. Similar interference fringes might be expected also from the 260 nm '*pin*/Cr' and '*pin*/Al' composites. However, the emission characteristics through the surfaces of ITO and the metal window electrodes are not the same. The light emission through ITO is uniform, whereas, in the case of the metal window electrodes, the area through which the light is emitted cannot be expanded. In the latter, the light seems to be emitted through some small spots created on the metal surface by thermal damage. The emitted light should experience multiple reflections between the bottom and top metal electrodes which may be self-roughened as a result of FP. Therefore, the coherence of the light may be lost prior to its escape from the small spots.

Although EL could be detected using different window electrodes like Al and Cr as shown in Fig.5.18, the formed region is successfully propagated only when ITO is used as the top electrode. This is believed to be due to the difference between the thermal conductivities of metals and ITO. It has been verified by the XRD measurements of Fig. 5.6 that FP is a temperature related phenomenon. Therefore, the quality of FP should depend on whether the heat is stored in the system or dissipated towards the surroundings. In the case of the metal top electrodes which have very high thermal conductivities, e.g. 94 W/K·m for Cr and 234 W/K·m for Al, the heat produced within the *pin* diode during FP is likely to be dissipated. In this respect, the heat storage in the system does not seem to be successful. The formed region remains point-like and further forming is prevented by the dissipation of the excess heat through these point-like regions easily. As for the ITO electrode, it is a transparent semiconductor with high electrical conductivity. On the other hand, its thermal conductivity of 11 W/K·m is much lower when compared with the metals. Instead of the vertical dissipation of the heat towards the air, it may be stored in the system and distributed along the whole diode. Consequently, the excess heat of the system can be used to carry on FP until the diode is completely formed.

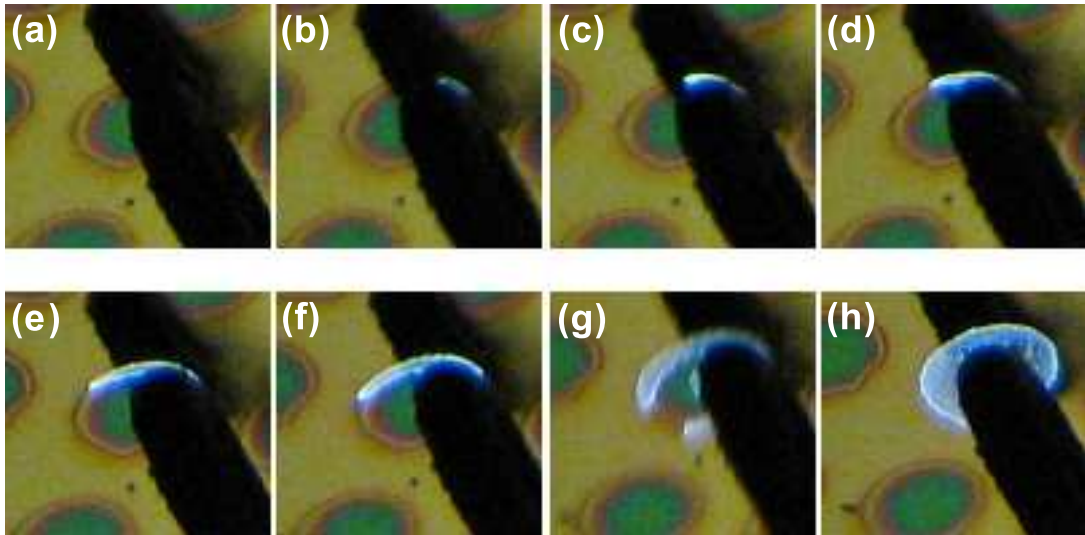


Figure 5.19: Lateral propagation of the formed region along the ITO electrode of the sample with the highest emission energy (D3) followed in time from (a) to (h) with ~ 10 s intervals.

The lateral propagation of the formed region throughout the whole ITO area has been observed and recorded by a commercial semi-professional camera. The photographs have been taken in a moderately illuminated room and reported here without any software modifications. Fig. 5.19-a illustrates the diode before the application of the voltage stress and Fig. 5.19-(b-h) exhibit the photographs of this diode under the forward voltage stress of 12 V taken at regular time intervals of about 10 s. In Fig. 5.19-b, the forming initiates at a small area which is not necessarily just under the measuring probe. Then, the formed region expands starting from this initial small area until the forming of the whole diode is completed in Fig. 5.19-h.

The temperature dependence of the EL spectra has been investigated; a typical example, that of the diode D2 is given in Fig. 5.20. As-measured EL spectra given in Fig. 5.20-a are a bit noisy due to the limitation on the current density when the measurement is performed under vacuum. The spectra corrected for the PMT responsivity using the as-measured data resulted in high fluctuations especially at wavelengths above 800 nm where the PMT responsivity is low. Therefore, the as-measured spectra were fitted by smooth lines and the corrections were performed using these smooth lines of each measurement (Fig. 5.20-b). The spectral distribution of the EL intensity seems to remain constant at different T . However, the total intensity slightly decreases at higher T . The thermal quenching of the EL intensity is not strong, as it is expected for wide-gap $a\text{-SiN}_x\text{:H}$ alloys [14].

The EL spectra of the formed diodes D0, D1, D2 and D3 are given in Fig. 5.21. The

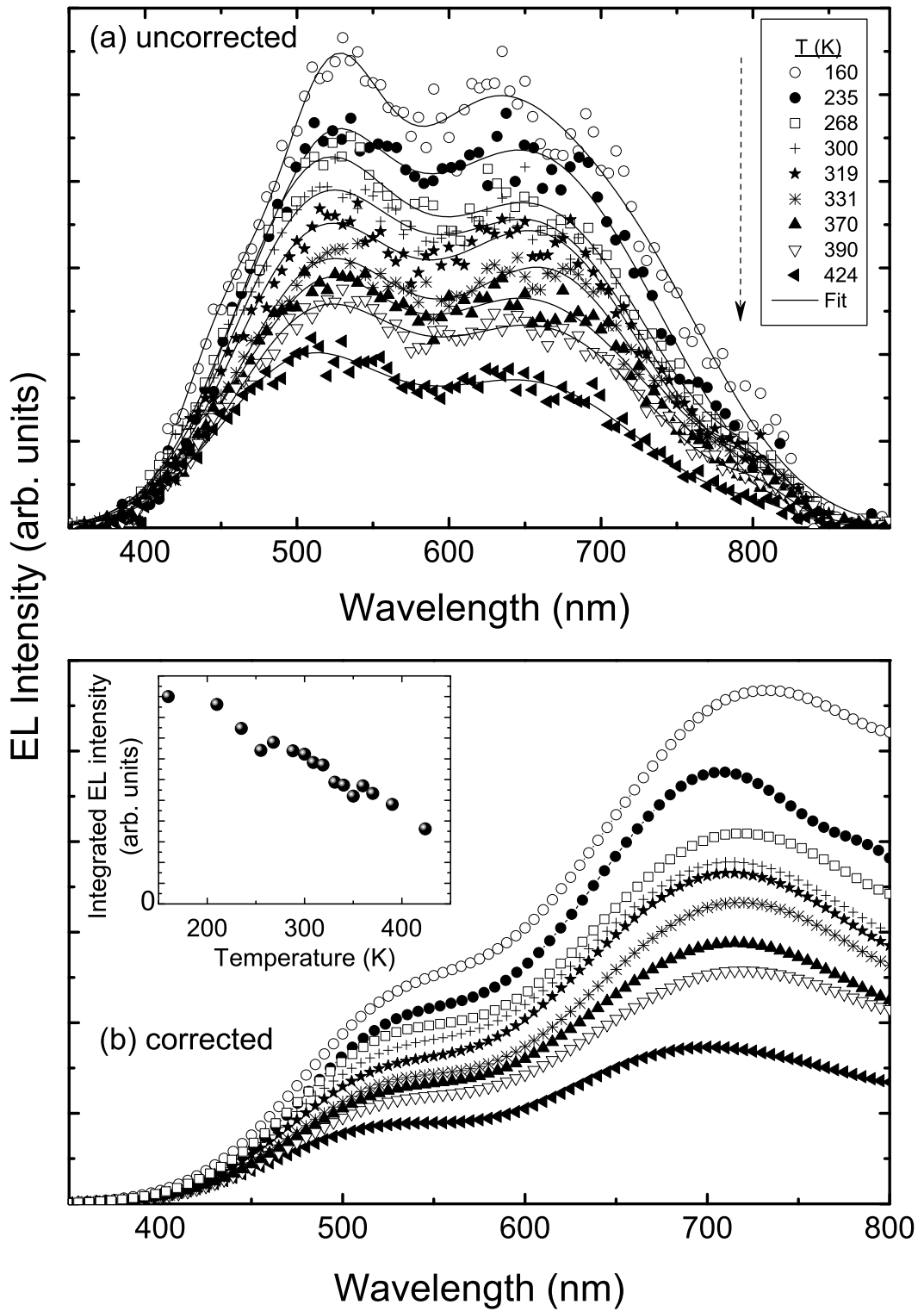


Figure 5.20: EL spectra at various temperatures for the diode D2. (a) As-measured EL data with their corresponding smoothing curves. (b) EL spectra corrected for the PMT responsivity using the smoothing curves of (a).

spectral ranges of EL emission of all the samples are broader than the responsivity range of the PMT at hand. The responsivity curves of several photodetectors used throughout this work can be seen in appendix D. In this regard, the data were collected by both PMT and Si photodiode to report the EL spectra from 300 nm to 1150 nm. The data measured by the Si photodiode was slightly noisy which resulted in high fluctuations in the corrected EL spectra especially at wavelengths above 1000 nm where the responsivity of the Si detector is low. Therefore, the spectra taken with the Si detector have been reported by the fitted smooth lines as shown in the inset of Fig. 5.21. After the corrections of the as-measured data for the responsivity of each detector, the EL curves obtained from different detectors have been matched by simple multiplication. The final spectrum of each diode was normalized for better comparison of their wavelength dependence. The interference fringes are due to the multiple reflections of the emitted light prior to its escape from the diode structure. The main thing to be recognized in Fig. 5.21 is that the peak wavelength of the emission is blueshifted when

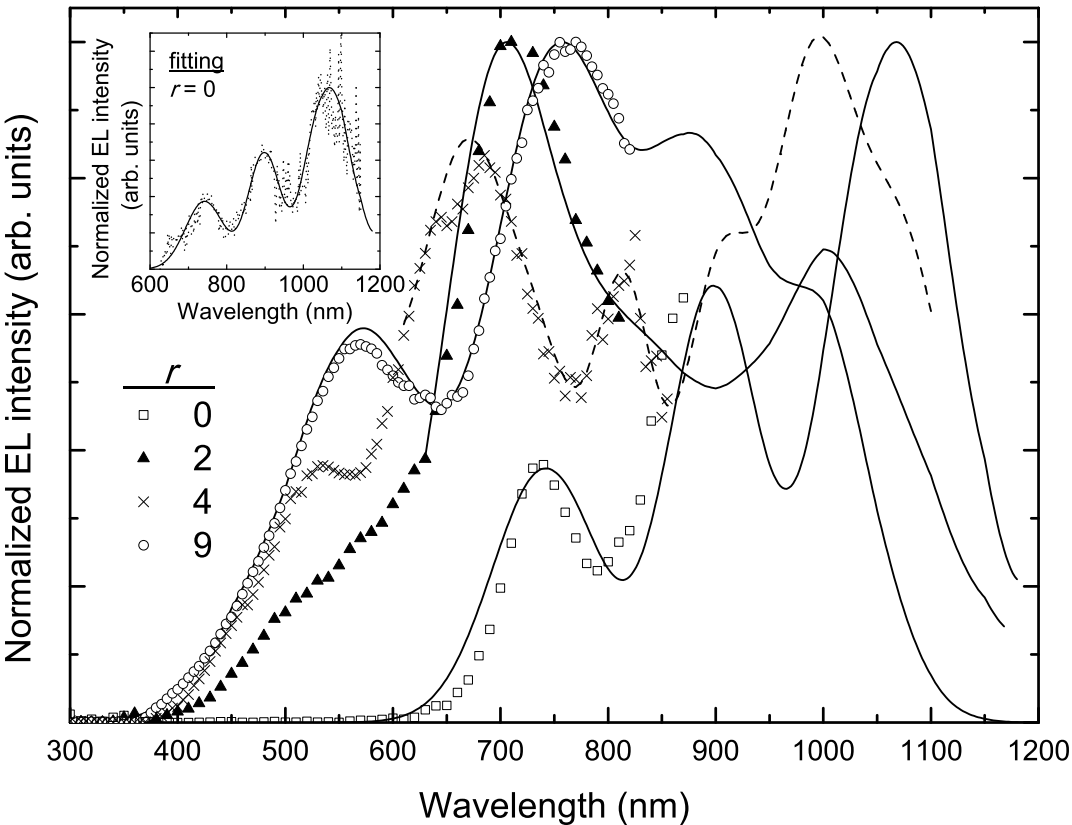


Figure 5.21: Corrected EL spectra of the formed diodes D0, D1, D2 and D3 produced with $r=0, 2, 4$ and 9 , respectively. Symbols are the data measured by the PMT and the lines are the fitted data taken with the Si photodiode. The fitting for the spectra of D0 is given in the inset.

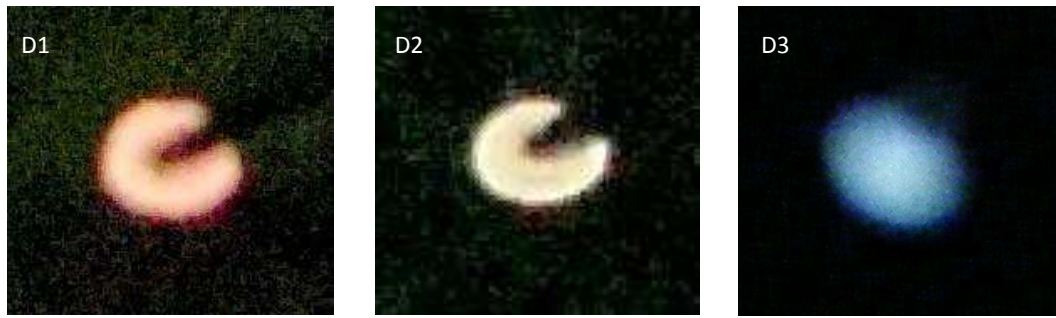


Figure 5.22: The photographs of the formed diodes D1, D2 and D3 during their light emission under application of the forward bias of ~ 11 V.

the ammonia to silane flow ratio in the intrinsic layer of the pin diode was increased. The EL spectrum of the homojunction diode D0 lies within the near infrared region, hardly including red color, but it is still invisible to the human eye. As for the heterojunction diodes D1, D2 and D3, the EL spectra has shifted to the full visible region, where the emissions can be easily perceived in the dark room as red-orange, orange-yellow and white-blue, respectively.

The photographs of the formed diodes D1, D2 and D3, taken with a commercial camera, is supplied in Fig. 5.22. The clarity of the photos is not as successful as that in Fig. 5.19 since manual focusing option was not available in this camera. However, it is clear that the EL emission blueshifts gradually from red-orange towards white-blue when r is increased from 2 towards 9.

It should be noted that besides the visible light emission, the diodes also emit in the near/mid infrared region. As an example, the EL data of the diode D1 was measured with different photodetectors in order to obtain the whole spectrum as given in Fig. 5.23. The data collected by the Si and Ge photodiodes was noisy; therefore, fitted smooth curves were used here for clear presentation (similar to Fig. 5.21). The normalized spectra in the visible-near infrared region measured with PMT, Si and Ge photodiodes were matched by simple multiplication. The emission in the near/mid infrared region decayed to zero intensity before reaching that in the visible-near infrared region. In this regard, the data of the near/mid infrared region measured by PbS was normalized independently since quantitative comparison between the emissions in each region was not possible. The emission around 2750 nm was absorbed by the CO_2 molecules present in the air.

The total electroluminescence intensities of the diodes were measured for different current densities. The plots for the diodes D0 and D2, given in Fig. 5.24, were normalized for their

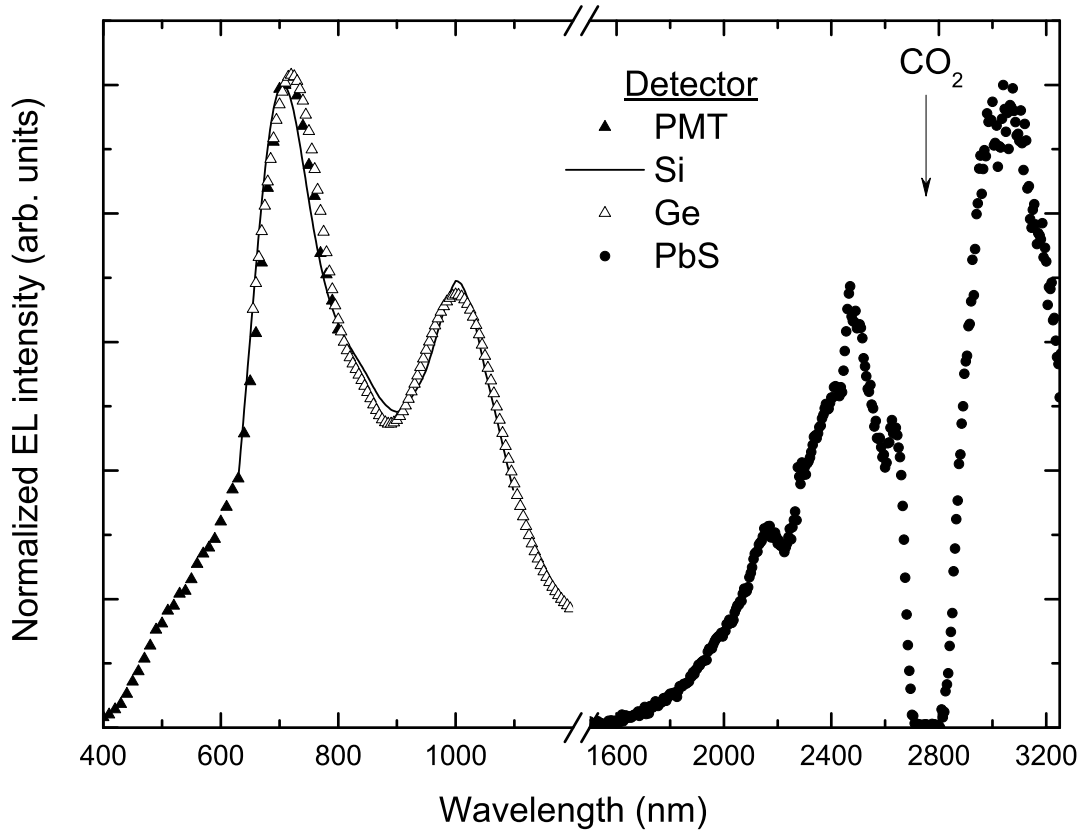


Figure 5.23: Normalized full EL spectrum of the diode D1 measured with different photodetectors. The band around 2750 nm is the absorption due to CO_2 molecules present in the air.

maximum brightness in order to make a better comparison between their behaviors. For the homojunction diode D0, the exponent m of the current density J in its proportionality with the brightness ($B \propto J^m$) is around 2 until the current density of 1 A/cm^2 is reached. The exponent m is reduced to about 1 when the current density exceeds 1 A/cm^2 . The dual character in the exponent was checked and verified via repeating the measurement in the opposite direction. As derived in section 1.6, $m \approx 2$ corresponds to the bimolecular radiative recombination of EHPs. Below 1 A/cm^2 , the applied field ($F < 1 \times 10^5 \text{ V/cm}$) may be considered intermediate. In this regime, the density of electrons and holes within the intrinsic layer can be assumed to be more or less comparable, so the bimolecular recombination dominates. Passing toward the high field regime, the current is space charge limited and the transport is supposed to be controlled by the capture and emission of the carriers out of the traps [77]. This process is possibly slower for the holes, considering the weaker crystallization towards p -side together with the lower hole mobility when compared to electrons. In this respect, the recombination

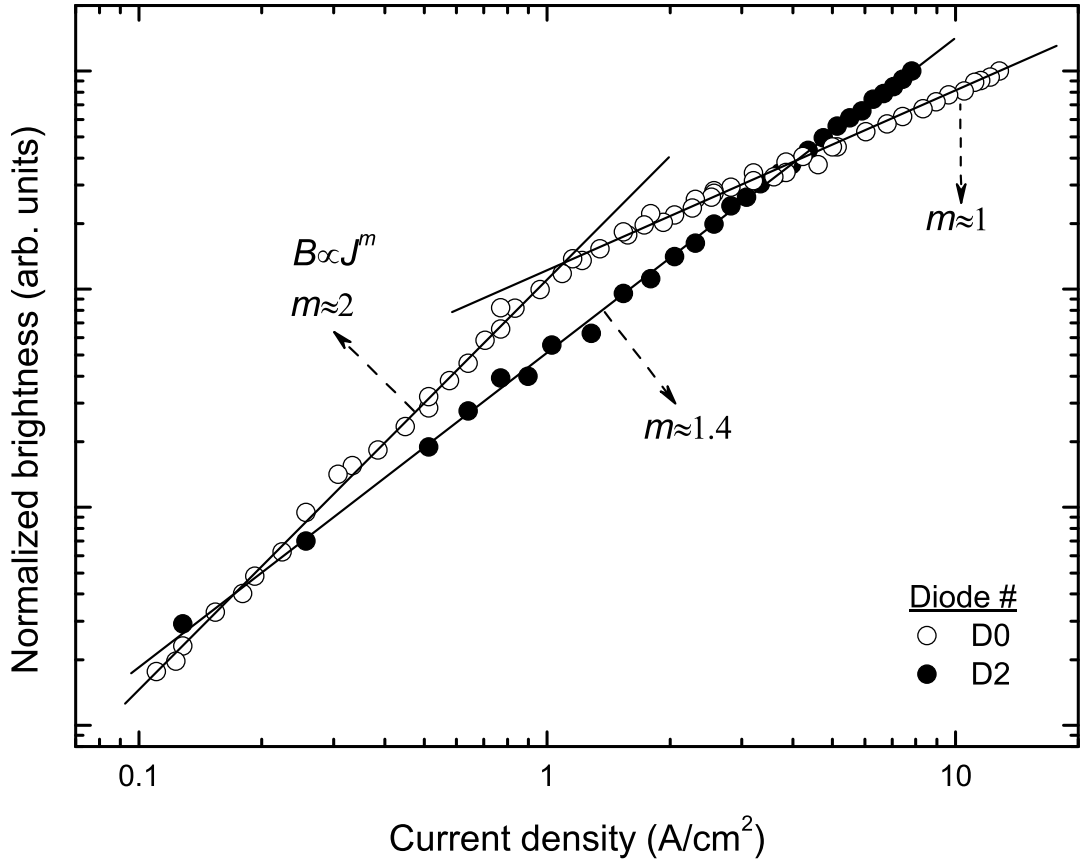


Figure 5.24: Normalized brightness versus current density plot of the diodes D0 and D2.

is determined by the hole being the minority carriers within the intrinsic layer, i.e. $m \approx 1$. As for the diode D2, the exponent m remains the same at about 1.4 for the whole current density range. The EL emission in the heterojunction diodes is detectable in the high field regime ($F > 5 \times 10^5$ V/cm). Similar to the high field case of the homojunction diode D0, the hole space charge may be rather accumulated near p/i interface and the electron space charge would extend throughout the whole intrinsic layer. The recombinations might be again concentrated close to p/i interface. However, the m value for D2 is rather higher, when compared with that of D0. It is probably associated with the higher band tail widths (i.e. α_c and α_v) in D2 case, where E_0 of the intrinsic layer was determined to be larger than that in D0 (see sections 2.3 and 4.3). The larger band tail width enhances the contribution of both hole and electron densities to the recombination process. Thus, this increase in E_0 together with the high F result in $m \approx 1.4$, which is an intermediate between the monomolecular and bimolecular cases.

5.4 Conclusion

The electrical and luminescent properties of a-SiN_x:H based *pin* diodes change drastically after their forming under high electric field at room temperature. XRD measurements verified that very high local temperatures were reached during FP. The temperature rise was sufficient for the transformation of the silicon rich regions in the intrinsic layer from amorphous to nanocrystalline phase. FP begins within a dimension of atomic orders. However, when ITO is used as the window electrode instead of metals, forming propagates throughout the whole diode area. Low heat conductivity of ITO prevents the produced heat from escaping to the air and contributes to the successful propagation of the forming.

The fresh diodes have good junction quality as concluded from high current rectification ratio. After FP, current density at low electric field increases several orders of magnitude, which is an expected result of crystallization at high local temperatures.

The thermal activation of conductivity after FP was explained via the band-tail hopping model with a slight modification. Instead of thermal excitation of the carriers from the midgap, their emission from Si nanocrystallites' fundamental energy level was assumed. At intermediate field regime, the field-enhanced carrier transport is limited by either detrapping from a Coulombic site or hopping out of a neutral empty state, latter being the probable case in this work. The high field current transport at low temperatures is assisted by both easier carrier emission from the potential wells and improved carrier mobility. At elevated temperatures of the high field regime, the density of injected carriers becomes comparable to the density of available states. In this case, the current is limited by the space charge accumulated in the exponentially distributed localized states.

The formed diodes experience a memory effect probably due to the rearrangement of the potential energy distribution within the intrinsic layer, arising from the charging/discharging phenomena of the deep traps for opposite polarities of the applied voltage.

The EL efficiency of the diodes is very poor before the forming. After FP is over, the EL intensity is improved by at least 30 times and the emission becomes easily perceivable by the human eye from the whole diode area. The EL energy distribution is temperature independent, while its intensity exhibits a weak thermal quenching. The emission spectra depend on the initial nitrogen content of the intrinsic layer. For nitrogen free homojunction *pin* diode, the maximum energy of the emitted light is ~2 eV with the low energy side of the spectrum extending towards the near infrared region. As the nitrogen is incorporated, the

emission energy blue-shifts. Although the spectra are broad for the time being, the emission color was adjusted from orange-red to white-blue via increasing the nitrogen content of the intrinsic layer.

CHAPTER 6

SUMMARY

The modern technology of electronics is based on a single material, silicon (Si). With the maturity of several decades, much information is known about Si processing and mass production of electronic devices. In addition, research and development centers are continuously investing on Si-based electronics. Therefore, it seems almost impossible to replace Si with other materials. On the other hand, the human interface of the electronic devices are fabricated with bright light emitting display systems, whose surface area is preferred to be as large as possible. Nowadays, either liquid crystal displays (LCDs) or organic light emitting diodes (OLEDs) are used in these display systems. However, none of these light sources are compatible with the complementary metal oxide semiconductor (CMOS) processing technology; their production requires high cost hybrid techniques. In order to produce very low cost display systems on very large areas, Si-based efficient light sources should be obtained.

With this motivation and in the light of literature, Si-rich hydrogenated amorphous silicon nitride (a-SiN_x:H) thin films were fabricated in a plasma enhanced chemical vapor deposition (PECVD) chamber at different $r = \text{NH}_3/\text{SiH}_4$ gas flow ratios in the range $2 < r < 9$ corresponding to $0.68 \leq x \leq 1.32$. The PL emission was controlled by the gas flow ratios and its intensity was high enough to be perceived at dark room by the naked human eye. The recombination properties were studied via considering both PL and optical absorption spectra. The behavior of the PL peak energy and PL FWHM with respect to the optical constants (optical gap and subgap absorption tail) indicated that band tail recombination is the dominant mechanism. A semiquantitative approach was introduced to estimate the band tail DOS among which the radiative recombination is promoted over the non-radiative processes. It was proposed that the carriers thermalize to some energy, i.e. PL peak energy, at which the band tail DOS reduces to ~1% of the relevant band edge DOS prior to their radiative recombination.

The PL intensities of different samples were compared after their correction for the absorbed light fraction of the PL excitation source. The result was in agreement with the band tail recombination model, where PL efficiency exponentially increased as the subgap absorption tail gets wider.

In this respect, a-SiN_x:H films seem suitable to be used as the luminescent active layer of Si-based LEDs. But beforehand, efficient electron and hole injections from either side of the intrinsic a-SiN_x:H film must be ensured. The most efficient way of opposite charge injections may be sandwiching the intrinsic layer between oppositely doped, *p*- and *n*-type layers to form a *pin* diode. The doping efficiency of the doped layers should be improved since the emission intensity is directly proportional to the injected carrier number. For this purpose, *p*-type nanocrystalline silicon (nc-Si:H) doping efficiency was optimized by systematically changing the growth conditions. The dark resistivity as low as 8 Ωcm was achieved, however, these films possessed high degree of nonuniformity along the PECVD electrode. With a little sacrifice from the lowest dark resistivity, fairly uniform films were obtained with the resistivity in the order of 10¹-10³ Ωcm. The optical gap of the optimized film was 2 eV, which is wide enough to transmit most of the emitted light.

The junction properties of the doped layers were tested in homojunction *pin* diodes. For this purpose, the optimum deposition conditions were determined as: B₂H₆/SiH₄≈0.34% for *p*-type nc-Si:H layer and H₂/SiH₄≈5 for intrinsic a-Si:H layer. The ideality factor of the optimized *pin* diode was 1.7 and its rectification ratio exceeded 4×10⁶ at 1.2 V. The thermal activation energy of the intrinsic layer was 830 meV, such that the Fermi level was slightly above the midgap in agreement with the *n*-type nature of undoped a-Si:H films. The energy distribution of DOS, deduced from SCLC method and CPM, exhibited the well known characteristic feature of a-Si:H, where DOS has a minimum around 0.5 eV below the conduction band edge. Consequently, the assumption of flat bands along the doped layers seems to be valid, pointing out that their free carrier densities are high enough for LED applications.

Although a-SiN_x:H films exhibit high PL efficiency at room temperature, their EL efficiency is below the technological limit of acceptance. The main bottleneck in the LEDs based on amorphous Si alloys is the difficult current transport through the wide band tails. As a solution, the nanocrystal silicon islands may be formed within a-SiN_x:H matrix. Then the increased free carrier density and mobility in the nanocrystallites would enhance the electrical transport. The usual crystallization methods require high annealing temperatures and/or sophisticated setups, e.g. laser irradiation, causing high cost and complex fabrication. Instead,

electro-forming at room temperature is promising for very low cost crystallization without the addition of any more fabrication steps. In this regard, good quality heterojunction *pin* diodes were electro-formed under high electric field; next, their I-V and EL characteristics were investigated in detail.

After the forming process (FP), the low field current density of all diodes increased by several orders of magnitude while high field regime I-V curve remained unchanged. The thermal activation energy was temperature dependent and was neither low enough for hopping conduction around the midgap nor high enough for thermal excitation towards the bands. On the other hand, band-tail hopping model seemed to account for these phenomena. In this respect, the carriers were assumed to be easily injected towards the nanocrystallites from quasi-Fermi levels of the doped layers. Then, they would be thermally excited to a band tail state followed by their subsequent downward hoppings.

The EL intensity was very weak before FP. A point-like light emission originated from an arbitrary region on the diode surface when FP started. If ITO was used as the window electrode, this region propagated throughout the whole diode area in seconds. After, strong and uniform light emission could be easily perceived in a moderately illuminated room. Although the EL band was broad, the emission color was adjustable from orange-red to white-blue by increasing the nitrogen content of the luminescent active layer.

REFERENCES

- [1] A. Zukauskas, M.S. Shur, R. Coska, *Introduction to Solid-State Lighting*, John Wiley & Sons Inc., New York, 2002, 1-48.
- [2] A. Lidow, Proceedings of APEC'99-14th Annual Applied Power Electronics Conf., Vol.1 (IEEE Piscataway, NJ) (1999), 10-15.
- [3] Energy Information Administration, *International Energy Outlook*, available at: www.eia.doe.gov/oiaf/ieo/index.html, Washington D.C., 2008, 61-62.
- [4] C. Hoelen, H. Borel, J. de Graaf, M. Keuper, M. Lankhorst, C. Mutter, L. Waumans, R. WeghProc., SPIE, Vol. 7058, 70580M (2008).
- [5] H.J. Round, *Electr. World* 49 (1907) 307.
- [6] O.V. Lossev, *Philos. Mag.* 6 (1928) 1024.
- [7] E.E. Violin, A.A. Kalnin, V.V. Pasyukov, Y.M. Tairov, D.A. Yaskov, 2nd International Conference on Silicon Carbide, 1968, *Mater. Res. Bull.*, 1969, 231.
- [8] J.A. Edmond, H.S. Kong, Jr. C.H. Carter, *Physica B* 185 (1993) 453.
- [9] E.F. Schubert, *Light-Emitting Diodes*, Cambridge University Press, United Kingdom, 2003, 3-85.
- [10] Gordon E. Moore, *Electronics*, 38, 8, April 19, 1965.
- [11] L. Pavesi, *J. Phys. Condens. Matter* 15 (2003) R1169-R1196.
- [12] H. Zimmermann, *Integrated Silicon Optoelectronics*, Springer, New York, 2000.
- [13] M.J. Powell, S.C. Deane, *Phys. Rev. B* 53(15) (1996) 10121-10132.
- [14] R.A. Street, *Hydrogenated Amorphous Silicon*, Cambridge University Press, Cambridge, 1991.
- [15] F. Boulitrop, D.J. Dunstan, *Phys. Rev. B* 28 (1983) 5923-5929.
- [16] D.J. Dunstan, F. Boulitrop, *Phys. Rev. B* 30 (1984) 5945-5957.
- [17] F. Giorgis, V. Vinegoni, L. Pavesi, *Phys. Rev. B* 61 (2000) 4693-4698.
- [18] A. Bacioglu, PhD Thesis, Hacettepe University, Turkey, 2006.
- [19] L. Tessler, I. Solomon, *Phys. Rev. B* 52 (1995) 10962-10971.
- [20] R.W. Collins, M.A. Paesler, W. Paul, *Solid State Commun.* 34 (1980) 833-836.
- [21] W. Siebert, R. Carius, W. Fuhs, K. Jahn, *Phys. Status Solidi B* 140 (1987) 311-321.

- [22] R.C. Chittick, J.H. Alexander, H.F. Sterling, *J. Electrochem. Soc.* 116, (1969) 77.
- [23] P.G. LeComber, W.E. Spear, *Phys. Rev. Lett.* 25 (1970) 509.
- [24] P.G. LeComber, A. Madan, W.E. Spear, *Proceedings of 13th Session of the Scottish Universities School in Physics 1972*, Academic Press, 1973, 393.
- [25] A. Madan, PhD Thesis, The University of Dundee, Scotland, 1973.
- [26] A. Madan, *J. Non-Cryst. Solids* 352 (2006) 881-886.
- [27] W.E. Spear, P.G. LeComber, *Solid State Commun.* 17 (1975) 1193.
- [28] W.E. Spear, P.G. LeComber, S. Kinmond, M.H. Brodsky, *Appl. Phys. Lett.* 28 (1976) 105.
- [29] D.E. Carlson, C. Wronski, *Appl. Phys. Lett.* 28 (1976) 671.
- [30] N.F. Mott, E.A. Davis (Eds.), *Electronic Processes in Non-Crystalline Materials*, Clarendon Press, Oxford, 1971.
- [31] R.A. Street, *Phys. Rev. Lett.* 49 (1982) 1187-1190.
- [32] R.A. Street, *Phys. Rev. B* 35 (1987) 1316-1333.
- [33] T. Aliyeva Anutgan, M. Anutgan, I. Atilgan, B. Katircioglu, *J. Non-Cryst. Solids* 356 (2010) 1102-1108.
- [34] S.M. Sze, K.K. Ng, *Physics of Semiconductor Devices*, 2nd Ed, Wiley, New York, 2002.
- [35] P. Fiorini, A. Mittiga, *Dark Electrical Characteristics of Amorphous n-i-n, p-i-p, p-i-n, and p-n Diodes in Amorphous and Microcrystalline Semiconductor Device, Vol. II, Material and Device Physics*, edr. J. Kanicki, Artech House, Norwood, MA, 1992.
- [36] C. van Berkel, M.J. Powell, A.R. Franklin, I.D. French, *J. Appl. Phys.* 73(10) (1993) 5264-5268.
- [37] A. Mittiga, P. Fiorini, M. Falconieri, F. Evangelisti, *J. Appl. Phys.* 66 (1989) 2667-2674.
- [38] A. Madan, M.P. Shaw, *The physics and applications of amorphous semiconductors*, Academic Press, Boston, 1988.
- [39] K. Luterva, T. Palent, I. Mikulskas, R. Tomasiuas, D. Muller, J.J. Grob, J.L. Rehspringer, B.J. Honerlage, *J. Appl. Phys.* 91 (2002) 2896.
- [40] W. Boonkosum, D. Kruangam, S. Panyakeow, *Jpn. J. Appl. Phys.* 32 (1993) 1534-1538.
- [41] D. Kruangam, M. Deguchi, T. Toyama, H. Okamoto, Y. Hamakawa, *IEEE T. Electron Dev.* 35 (7) (1988) 957-965.
- [42] R-H. Yeh, T-R. Yu, T-C. Chung, S-Y. Lo, J-W. Hong, *IEEE T. Electron Dev.* 55 (4) (2008) 978-985.
- [43] K.S. Cho, N-M. Park, T-Y. Kim, K-H. Kim, G.Y. Sung, J.H. Shin, *Appl. Phys. Lett.* 86 (2005) 071909.

- [44] N. Kashio, H. Kato, Y. Ohki, Proceedings of 2001 International Symposium on Electrical Insulating Materials (ISEIM 2001) 79-82.
- [45] B.-H. Kim, C.-H. Cho, S.-J. Park, N.-M. Park, G.Y. Sung, Appl. Phys. Lett. 89 (2006) 063509.
- [46] N.-M. Park, C.-J. Choi, T.-Y. Seong, S.-J. Park, Phys. Rev. Lett. 86 (2001) 1355-1357.
- [47] H. Kato, N. Kashio, Y. Ohki, K.S. Seol, T. Noma, J. Appl. Phys. 93(1) (2003) 239-244.
- [48] I. Atilgan, PhD Thesis, Middle East Technical University, Turkey, 1993.
- [49] A.V. Tikhonravov, M.K. Trubetskov, OptiChar, <http://www.optilayer.com> V 4.12 (2002), last visited on August 2010.
- [50] N.-M. Park, S. H. Kim, G. Y. Sung, S.-J. Park, Chem. Vapor Depos. 8(6) (2002) 254-256.
- [51] G. Scardera, T. Puzzer, G. Conibeer, M.A. Green, J. Appl. Phys. 104 (2008) 104310(7).
- [52] Y.Q. Wang, Y.G. Wang, L. Cao, Z.X. Cao, Appl. Phys. Lett. 83 (2003) 3474-3476.
- [53] W.A. Lanford, M.J. Rand, J. Appl. Phys. 49 (1978) 2473-2477.
- [54] E. Bustarret, M. Bensouda, M.C. Habrard, J.C. Bruyere, Phys. Rev. B 38 (1988) 8171-8184.
- [55] V. Verlaan, A.D. Verkerk, W.M. Arnoldbik, C.H.M. van der Werf, R. Bakker, Z.S. Houweling, I.G. Romijn, D.M. Borsa, A.W. Weeber, S.L. Luxembourg, M. Zeman, H.F.W. Dekkers, R.E.I. Schropp, Thin Solid Films 517 (2009) 3499-3502.
- [56] W.A.P. Claassen, W.G.J.N. Valkenburg, F.H.P.M. Habraken, Y. Tamminga, J. Electrochem. Soc. 130 (1983) 2419-2423.
- [57] T. Makino, J. Electrochem. Soc. 130 (1983) 450-455.
- [58] T.M. Searle, W.A. Jackson, Philos. Mag. 60(2) (1989) 237-255.
- [59] J.J. Markham, *F-centres in Alkali Halides*, Academic Press, New York, 1966.
- [60] M.J. Estes, G. Moddel, Phys. Rev. B 54(20) (1996) 14633-14642.
- [61] C.S. Magalhães, F. Alvarez, M. Sebastiani, P. Fiorini, F. Pozzilli, F. Evangelisti, J. Phys.-Condens. Mat. 5 (1993) A329-A330.
- [62] I. G. Austin, W. A. Jackson, T. M. Searle, P. K. Bhat, and R. A. Gibson, Philos. Mag. B 52 (1985) 271-288.
- [63] B.A. Wilson, A.M. Sergent, J.P. Harbison, Phys. Rev. B 30(4) (1984) 2282-2285.
- [64] D.V. Tsu, B.S. Chao, S.R. Ovshinsky, S. Guha, J. Yang, Appl. Phys. Lett. 71(10) (1997) 1317-1319.
- [65] C.C. Tsai, in *Amorphous Silicon and Related Materials*, edr. H. Fritzsche, World Scientific, Singapore, Vol. 1, 1988, p. 123.
- [66] T. Aliyeva, PhD Thesis, Middle East Technical University, Turkey, 2010.

- [67] M. Anutgan, T. Aliyeva Anutgan, E. Ozkol, I. Atilgan, B. Katircioglu, J. Non-Cryst. Solids 355 (2009) 1622-1629.
- [68] Z. Li, X. Zhang, G. Han, Phys. Status Solidi A 207(1) (2010) 144-148.
- [69] O. Sezer, M.S. Thesis, Middle East Technical University, Turkey, 2001.
- [70] J.M. Shah, Y.-L. Li, Th. Gessmann, E.F. Schubert, J. Appl. Phys. 94(4) (2003) 2627-2630.
- [71] K.D. Mackenzie, P.G. Le Comber, W.E. Spear, Philos. Mag. B 46 (1982) 377-389.
- [72] D. Han, K. Wang, Sol. Energ. Mat. Sol. C. 78 (2003) 181-233.
- [73] S. Nespurek, J. Sworakowski, J. Appl. Phys. 51(4) (1980) 2098-2102.
- [74] J. Kocka, M. Vanecek, F. Schauer, J. Non-Cryst. Solids 97-98 (1987) 715-722.
- [75] K. Pierz, H. Mell, J. Terukov, J. Non-Cryst. Solids 77-78 (1985) 547-550.
- [76] M.B. Bebek, M.S. Thesis, Middle East Technical University, Turkey, 2009, pp. 70-78.
- [77] S.M. Paasche, T. Toyama, H. Okamoto, Y. Hamakawa, IEEE T. Electron Dev. 36 (12) (1989) 2895-2902.
- [78] Y. Liu, T.P. Chen, L. Ding, M. Yang, J.I. Wong, C.Y. Ng, S.F. Yu, Z.X. Li, C. Yuen, F.R. Zhu, M. C. Tan, S. Fung, J. Appl. Phys. 101 (2007) 104306.
- [79] Z.H. Cen, T.P. Chen, L. Ding, Y. Liu, J.I. Wong, M. Yang, Z. Liu, W.P. Goh, F.R. Zhu, S. Fung, Appl. Phys. Lett. 94 (2009) 041102.
- [80] I. Pelant, P. Fojtik, K. Luterova, J. Kocka, A.Poruba, J. Stepanek, Appl. Phys. A 74 (2002) 557-560.
- [81] I. Stenger, A. Abramov, C. Barthou, Th. Nguyen-Tran, A. Frigout, P. Roca i Cabarrocas, Appl. Phys. Lett. 92 (2008) 241114.
- [82] V.A. Burdovitsin, V.L. Galanskii, V.D. Zamozhskii, B.M. Kuchumov, Yu.B. Yankelevich, Russ. Phys. J. (1975) 1698-1701.
- [83] S. Habermehl, R.T. Apodaca, R.J. Kaplar, Appl. Phys. Lett. 94 (2009) 012905.
- [84] A.K. Kulkarni, L.C. Chang, Thin Solid Films, 301 (1997) 17-22.
- [85] J.S. Ro, W.E. Hong, Jpn. J. Appl. Phys. 45 (2006) L1142-L1145.
- [86] P. Fojtik, K. Dohnaleva, T. Mates, J. Stuchlik, I. Gregorova, J. Chval, A. Fejfar, J. Kocka, I. Pelant, Philos. Mag. B 82 (2002) 1785-1793.
- [87] L. Dal Negro, J.H. Yi, L.C. Kimerling, S. Hamel, A. Williamson, G. Galli, Appl. Phys. Lett. 88 (2006) 183103.
- [88] S.M. Prokes, O.J. Glembocki, Mater. Chem. Phys. 35 (1993) 1-10.
- [89] P.D. Milewski, D.J. Lichtenwalner, P. Mehta, A.I. Kingon, D. Zhang, R.M. Kolbas, J. Electron Mater. 23(1) (1994) 57-62.

- [90] L. Brus, J. Phys. Chem. 98 (1994) 3575-3581.
- [91] H.L. Hao, L.K. Wu, W.Z. Shen, H.F.W. Dekkers, Appl. Phys. Lett. 91 (2007) 201922.
- [92] M.S. Hybertsen, Phys. Rev. Lett. 72 (1994) 1514-1517.
- [93] J.R. Heath J.M. Jasinski, Mater. Res. Soc. Symp. Proc. 256 (1992) 117-122.
- [94] J.M. Perez, J. Villalobos, P. McNeill, J. Prasad, R. Cheek, J. Kelber, J.P. Estrera, P.D. Stevens, R. Glosser, Appl. Phys. Lett. 61 (1992) 563-565.
- [95] F. Edelman, A. Chack, R. Weil, R. Baserman, Y.L. Khait, R. Werner, B. Rech, T. Roschek, R. Carius, H. Wagner, W. Bayer, Sol. Energ. Mat. Sol. C. 77 (2003) 125-143.
- [96] B. Gelloz, N. Koshida, Jpn. J. Appl. Phys. 43 (2004) 1981-1985.
- [97] C. Godet, Philos. Mag. B 81 (2) (2001) 205-222.
- [98] O. Ozdemir, M. Anutgan, T.A. Anutgan, I. Atilgan, B. Katircioglu, J. Non-Cryst. Solids 355 (2009) 851-859.
- [99] A.K. Jonscher, Thin Solid Films 1 (1967) 213-234.
- [100] E. Staryga, J. Swiatek, Thin Solid films 56 (1979) 311-319.
- [101] R.M. Hill, Philos. Mag. 23 (1971) 59.
- [102] N. Apsley, H.P. Hughes, Philos. Mag. 30 (1974) 963-972.
- [103] N. Apsley, H.P. Hughes, Philos. Mag. 31 (1975) 1327-1339.
- [104] C. Godet, S. Kumar, V. Chu, Philos. Mag. 83 (2003) 3351-3365.
- [105] M. Anutgan, M.Sc. Thesis, Middle East Technical University, Turkey, 2007.
- [106] M.A. Lampert, P. Mark, *Current Injection in Solids*, Academic, New York, 1970.
- [107] K.J. Price, L.R. Sharpe, L.E. McNeil, E.A. Irene J. Appl. Phys. 86 (1999) 2638-2641.
- [108] M. Ribeiro, I. Pereyra, M.I. Alayo, Thin Solid Films 426 (2003) 200-204.
- [109] L.D. Negro, J.H. Yi, J. Michel, L.C. Kimerling, S. Hamel, A. Williamson, G. Galli, IEEE J. Sel. Top. Quant 12, 6 (2006) 1628-1635.
- [110] R-H. Yeh, W-H. Liu, S-Y. Lo, J-W. Hong, Solid State Electron. 50 (2006) 1495-1500.
- [111] K.-H. Kim, J.-H. Shin, N.-M. Park, C. Huh, T.-Y. Kim, K.-S. Cho, J.C. Hong, G.Y. Sung, Appl. Phys. Lett. 89 (2006) 191120.
- [112] R. Huang, K. Chen, H. Dong, D. Wang, H. Ding, W. Li, J. Xu, Z. Ma, Ling Xu, Appl. Phys. Lett. 91 (2007) 111104.
- [113] R. Huang, K. Chen, P. Han, H. Dong, X. Wang, D. Chen, W. Li, J. Xu, Z. Ma, X. Huang, Appl. Phys. Lett. 90 (2007) 093515.
- [114] R. Huang, H. Dong, D. Wang, K. Chen, H. Ding, X. Wang, W. Li, J. Xu, Z. Ma, Appl. Phys. Lett. 92 (2008) 181106.

- [115] M. Perálvarez, J. Carreras, J. Barreto, A. Morales, C. Domínguez, B. Garrido, Appl. Phys. Lett 92 (2008) 241104.
- [116] S. Nespurek, J. Sworakowski, Phys. Status Solidi A 41 (1977) 619-627.

APPENDIX A

PHOTOMETRY

The visual sense of brightness is the main concern of *photometry* which differs from *radiometry* in dealing only with the visible spectrum. Therefore, the relevant concepts are usually derived from the Latin word *lumen*, meaning *light* and *shine*. The performance of a light source is usually considered via its *brightness* (or *luminance*), *luminous efficacy* and *quantum efficiency*. These quantities and their conventional units should be introduced to get familiar with the terminology before comparing various LEDs.

The *luminous flux*, Φ_v is the power corresponding to the visible part of a *radiant flux*, Φ_e received by human eyes. The human eye response to the radiation is introduced in 1924 by the International Commission on Illumination (CIE) through the *normalized luminous efficiency function*, $V(\lambda)$ which is defined in the visible range of 380-780 nm. The *luminous flux* is given in lumens (lm) and mathematically expressed as:

$$\Phi_v = 683 \text{ lm/W} \times \int \Phi_{e\lambda} V(\lambda) d\lambda, \quad (\text{A.1})$$

where $\Phi_{e\lambda} \equiv d\Phi_e/d\lambda$ is the spectral density of the radiant power and 683 lm/W is the Watt-to-lumen conversion constant for the peak value of $V(\lambda)$ at 555 nm.

The *luminous intensity*, I_v is the luminous flux emitted from a surface area A per unit solid angle:

$$I_v = d\Phi_v/d\Omega = 683 \text{ lm/W} \times \int I_{e\lambda} V(\lambda) d\lambda, \quad (\text{A.2})$$

where $I_{e\lambda} \equiv dI_e/d\lambda$ is the spectral density of the radiant intensity. The SI unit of the luminous intensity is candela (cd). Being directly proportional to the device area, the luminous intensity is not applicable to the light sources having finite dimensions; such that larger sources might have higher intensities even with very weak emission. Usually, LEDs are described by *brightness* B , which is the visibility of a light source by human eyes independent of both the

device area and the solid angle of the target (or eyes):

$$B = d^2\Phi_v/(d\Omega dA \cos \theta) \equiv dI_v/dA', \quad (\text{A.3})$$

where dA' is the projected area observed by an angle θ . The SI unit of brightness is candela per meter squared (cd/m^2 ; sometimes called *nits*). The brightness of a light source should be more than 10 cd/m^2 for a completely photopic vision where the color distinguishing cone receptors on the retina of the eye are susceptible. Otherwise, mesopic and then scotopic visions dominate by the color insensitive rod receptors. The brightnesses of the sun and the moon from the sea level are approximately $1.6 \times 10^9 \text{ cd/m}^2$ and 2500 cd/m^2 , respectively [1]. The commercial liquid crystal displays (LCDs) are as bright as $50\text{-}500 \text{ cd/m}^2$.

The capacity (or ability) of the radiant flux to produce a visual effect is called the *luminous efficacy*. Mathematically, it is the luminous-to-radiant flux ratio with the unit of lm/W :

$$K = 683 \text{ lm/W} \times \frac{\int_{380}^{780} \Phi_{e\lambda} V(\lambda) d\lambda}{\int_0^{\infty} \Phi_{e\lambda} d\lambda}. \quad (\text{A.4})$$

The efficacy takes its maximum value of 683 lm/W for a monochromatic radiation at 555 nm , creating the highest possible visual effect per radiant flux on the human eyes.

In addition to the characteristics of the emitted light, the power consumed during this process should also be taken into account. In an ideal LED, each electron-hole pair (EHP) injected into the luminescent active layer recombines radiatively and creates one photon with the *quantum efficiency* of unity. However in reality, electrons and holes may also be captured by non-radiative recombination centers. Furthermore, they can reach the relevant electrodes (anode and cathode, respectively) without any recombinations. In this respect, the *internal quantum efficiency* is defined as:

$$\xi_{int} = \frac{\text{radiant flux produced within the LED}}{\text{total number of EHPs present in the active region per second}}. \quad (\text{A.5})$$

The photons created within the luminescent layer should escape into the free space to contribute the brightness. However, several possible loss mechanisms prevent the photons from leaving the LED. The emitted light might be reabsorbed by the substrate and the metal contacts or even by the semiconductor itself. In addition, the difference between the refractive indices of the layers may lead to internal reflections reducing the escape probability of the light. After all, more than half of the photons cannot escape from a typical LED without complex and costly fabrication processes [9]. The *extraction efficiency* is the useful fraction

of the optical power produced via the radiative recombinations of the injected EHPs:

$$\xi_{extraction} = \frac{\text{radiant flux emitted into free space}}{\text{radiant flux produced within the LED}}. \quad (\text{A.6})$$

The numbers of electrons and holes injected into the luminescent active region are usually different, which may stem from the differences between their densities (n and p , respectively), mobilities (μ_n and μ_p , respectively) and the heights of the notch barriers (or band discontinuities) present in the heterostructures. However, their numbers are desired to be equal within the active region, such that the excess ones would reach the contacts without recombination and lead to uneconomical power consumption. In typical pn junctions, the light is extracted from only one region (e.g. p region) by engineering the depletion width with an appropriate doping ($N_D \gg N_A$). Hence, the already present holes of the p region are expected to recombine with the injected electrons. In this respect, the *injection efficiency* is the fraction of the injected minority carriers into the active region [1]:

$$\xi'_{inj} = \frac{I_{minority}}{I}, \quad (\text{A.7})$$

where I is the total current passing through the LED. If the active layer is intrinsic as in pin and MIM devices, the currents of both carriers are expected to be equal for an efficient injection:

$$\xi_{inj} = \frac{I_{carrier-1}}{I_{carrier-2}}; \text{ with } I_{carrier-2} \geq I_{carrier-1}. \quad (\text{A.8})$$

The overall quantum efficiency of LEDs is obtained by the product of extraction, injection and internal quantum efficiencies. The *external quantum efficiency* is defined as the ratio of the number of photons emitted into the free space to the number of charge carriers injected into the LED (per second):

$$\xi_{ext} = \xi_{int} \times \xi_{extraction} \times \xi_{inj} = \frac{\Phi_e/h\bar{\nu}}{I/q}, \quad (\text{A.9})$$

where $h\bar{\nu}$ is the mean energy of a single photon and q is the elementary charge (1.6×10^{-19} C). The mean energy, $h\bar{\nu}$ of the emitted photons are not necessarily equal to the energy, qV of the injected EHPs acquired from the power supply, where V is the voltage drop across the LED. Then, the photon energy might be reduced if the radiations occur via multiphase recombinations within the forbidden gap of the semiconductor. The energy difference is given out by phonon emissions, heating up the device. The energy of the photons might also be higher than that of the supply in the presence of higher thermal energy electrons. The photons with energies $h\nu > qV$ take away some portion of the heat from the device. The ratio of the

mean radiant energy to the electrical energy supplied by the power source is called the *feeding efficiency*:

$$\xi_f = \frac{h\bar{\nu}}{qV}. \quad (\text{A.10})$$

The *power efficiency*, which is also called the *wall plug efficiency*, is the amount of radiant flux emitted into the free space in exchange for the supplied power:

$$\xi_{power} = \xi_{ext} \times \xi_f = \frac{\Phi_e}{IV}. \quad (\text{A.11})$$

The above efficiency relations are independent of the wavelength of the radiation. If only the visible spectrum is to be taken into account, then these relations need to be multiplied by the luminous efficacy, Eq. A.4 to obtain the corresponding luminous efficiencies.

APPENDIX B

LITERATURE REVIEW CHARTS FOR THE LUMINESCENT PROPERTIES OF a-SiN_x:H THIN FILMS

The literature review on PECVD grown a-SiN_x:H based LEDs, that was started in section 1.6, is listed in the charts below (see Fig. B.1-B.5). The sources (1-14) numerated in the 'Year' column correspond to the references [107, 46, 52, 108, 43, 45, 109, 110, 111, 112, 113, 114, 42, 115], respectively. The sequence of the sources is arranged with respect to the year in order to provide easier chronological follow of the research. 'Post deposition treatment' column is particularly given since the use of the thermal treatment adds an expensive step to the fabrication and consequently increases the production cost. 'Comments' column describes the observations and results on the luminescent properties of a-SiN_x:H films and/or LED devices obtained in each study. Note that: RF power density is given if possible and RT denotes 'room temperature'.

Year	Source gas	Flow parameters	Power	Press. (Torr)	Subst. Temp. (°C)	Post deposition treatment	Device structure	Comments
1-1999	5% SiH ₄ in He 10% N ₂ O in He	N ₂ O: SiH ₄ = 13:20	35 W	0.1	300	Some of the films: 950°C in quartz furnace for 30 min. in 100 sccm 10% H ₂ in N ₂ .	0.5 cm ² , 1.5 nm Au/53 nm, $\eta \sim 1.66$ (optimized) SiO ₂ N _x / (100) 2 Ωcm p-Si/Ga:In	Maximum power efficiency at forward bias: 4×10^{-6} , at reverse bias: 7×10^{-7} . EL was observed only in the annealed samples. EL from the films thinner than 50 nm was not significant. $I \sim V^n$, $n \sim 1-2.3$, space charge limited current.
2-2001	N ₂ -diluted 5% SiH ₄ and N ₂	SiH ₄ : 10, N ₂ : 100-800 (sccm)	6 W	0.5	300	No	Si (001)/a-SiN _x	PL from confinement effect: E (eV) = $1.56 + 2.40/r^2$ with r being the quantum dot (QD) size (or diameter). $r_{avg} = 1.9$ nm, QD density = 1.9×10^{19} cm ⁻³ . Emitting orange light at 560 nm. Small Stoke's shift of about 300 meV indicates passivated QD surface states avoiding deep luminescent centers.
3-2003	SiH ₄ /N ₂ /H ₂	N ₂ :SiH ₄ = 1-5.5 Total: 60 sccm	35 W	1.13	< 60	<900°C, 2 min, N ₂ /Ar.	1.2 μm on Si (100)	PL _{max} when N ₂ :SiH ₄ = 3.5. Low T, high-density Si-QDs (4×10^{12} cm ⁻²). If Si-H bond density increases then gap opens and PL blueshifts. Annealing enhances PL.
4-2003	SiH ₄ /N ₂ O	N ₂ O/ SiH ₄ : 0.25-0.5	500 mW/cm ²	0.01	320	750-1000°C, 2-33 hours, under N ₂ .	p-Si (100) 1-10 Ωcm/ \sim 100 nm SiN _x	Larger the QDs, lower the emission energy, consistent with the size effect. PL intensity decreased with crystallization.

Figure B.1: Literature review chart of a-SiN_x:H based LEDs.

Year	Source gas	Flow parameters	Power	Press. (Torr)	Subst. Temp. (°C)	Post deposition treatment	Device structure	Comments
5-2005	<i>i layer</i> : NH ₃ /10% Argon diluted SiH ₄ . <i>n layer</i> : 10% Argon diluted SiH ₄ , CH ₄ , trimethyl phosphate metalorganic source.	<i>i layer</i> : NH ₃ :SiH ₄ = 10:50 (sccm)	5 W	0.5	250	Before metallic contacts, 900°C, 3 min. rapid thermal annealing to activate doping layer.	ITO/transparent <i>n a-</i> SiC:H (10^{15} cm ⁻³)/Si-in-SiN _x /p-Si (10^{16} cm ⁻³)/Ni:Au (30:120) Mesa: 0.5×0.5 mm ²	Current rectification of ~2-4 orders of magnitude. Current dominated by Fowler-Nordheim tunneling. Similar PL/EL at 600 nm (orange). $\xi_{\text{ext}} = 1.6\%$. Very poor EL without SiC doping layer.
6-2006	N ₂ -diluted 5% SiH ₄ and NH ₃	No info	6 W	0.5	300	400°C, 80 s, under air.	20-100 nm Ni-Au (not annealed)/ 10^{15} cm ⁻³ p-Si (100)/Si-in-SiN _x /9-2 nm Ni-Au (annealed)	Annealing leads to more transparent Ni/Au contacts and lower turn-on voltage. NiSi formation at the interface lowers the barrier height. Light of energy 1.96 eV was observed by naked eye in dark room at 6 V bias with $\xi_{\text{ext}} = 3.3 \times 10^{-3}\%$.
7-2006	N ₂ /SiH ₄	Si rich. No other info.	No info	No info	400	Nitrogen annealing 600-800°C for 10 min	Au/700 nm Si rich nitride/ <i>n</i> ⁺⁺ or <i>p</i> ⁺⁺ Si/100 nm Au or 100 nm p-ITO for MIS or pin structures, respectively	Electrical properties dramatically enhanced after annealing. Similar PL/EL peaking around 600-1200 nm. N-Si bonds between the Si clusters and Si rich nitride matrix were claimed to be responsible for the light emission.

Figure B.2: Literature review chart of a-SiN_x:H based LEDs (continued).

Year	Source gas	Flow parameters	Power (W)	Press. (Torr)	Subst. Temp. (°C)	Post deposition treatment	Device structure	Comments
8-2006	> 90% H ₂ -diluted SiH ₄ , PH ₃ , B ₂ H ₆ and GeH ₄ . Pure NH ₃ and C ₂ H ₂ .	i a-SiC:H – SiH ₄ :C ₂ H ₂ = 100:12.5 (sccm) i a-SiN:H – SiH ₄ :NH ₃ = 100:20 (sccm). See reference for the other layers.	14 mW/cm ²	0.41-0.5	180	100 sccm H ₂ , 210 mW/cm ² , 0.4 Torr, 5 min., after each layer. After contact growth, rapid annealing at 420°C under H ₂ for 25 min (for the nitride).	400 nm Al/n ⁺ [100], 0.005 ohm.cm CZ Si/n ⁺ a-Si:H (7.5 nm)/n ⁺ a-SiCGe:H (23.5 nm)/i a-SiN (or C):H (30 nm)/p ⁺ a-SiC:H (15 nm)/p ⁺ a-Si:H (5 nm)/ITO (120 nm, 0.78 cm ²)	Rapid thermal annealing improved the ohmic contacts between the electrodes and the amorphous layers. Carbide and nitride layers: 1860 cd/m ² at 650 nm and 370 cd/m ² at 530 nm, respectively both at 300 mA/cm ² injection current. Graded gap structure led to voltage dependent activation of different luminescent centers at the interfaces: voltage tunable LEDs. B vs. J ^m , m~0.78, tail-to-tail recombinations.
9-2006	<i>i</i> layer and <i>rugged surface</i> : NH ₃ /10% Argon diluted SiH ₄ . <i>n</i> layer: 10% Argon diluted SiH ₄ , CH ₄ , trimethyl phosphate metalorganic source.	No info.	5 W	0.5	250	Activation of <i>n</i> layer by 950°C, 2 min rapid thermal annealing	a-SiN _x (rugged surface)/ITO/ <i>n</i> a-SiC:H (300 nm)/i a-SiN:H with Si nanocrystals (50 nm)/p-Si/Ni:Au	ITO effective for current spreading. 2.8 fold enhancement in light extraction efficiency compared to a flat surface.
10-2007	NH ₃ /SiH ₄	R _N =NH ₃ /(NH ₃ +SiH ₄)= 0.5-0.8	20 W	0.62	RT	Oxidation, 100°C, 20 W	Al/80 nm SiN _x /(50 ohm per square) ITO/glass	EL from Si-rich, N-rich SiN films. Barrier reduced for Si-rich films (from Fowler-Nordheim). Much higher EL at 550 nm for Si-rich films. PL/EL may be related to the same Si-O luminescent centers.

Figure B.3: Literature review chart of a-SiN_x:H based LEDs (continued).

Year	Source gas	Flow parameters	Power	Press. (Torr)	Subst. Temp. (°C)	Post deposition treatment	Device structure	Comments
11- 2007	NH ₃ /SiH ₄	NH ₃ : SiH ₄ = 8:32 (sccm)	20 W	0.62	RT	Oxidation, 100°C, 20 W	3 mm diameter Al/a-SiN _x /(50 ohm per square) ITO/glass or 0.785 mm ² Al circular ring/ a-SiN _x /4 ohm.cm (100) <i>p</i> -Si/Al	LEDs with ITO and <i>p</i> -Si anodes had peak emissions at 560 nm and 540 nm with 9 V and 6 V thresholds, respectively, observable at dark room conditions. Downwards band bending of <i>p</i> -Si ($E_F = E_V + 0.3$ eV). Upwards band bending for 3.75 eV gap <i>p</i> -ITO. Lower barrier height for <i>p</i> -Si. Smaller difference between PL and EL for <i>p</i> -Si. 500nm PL is attributed to the Si-O luminescent centers.
12- 2008	NH ₃ /SiH ₄	R _N =0.66->0.92	10 W	0.28	250	No	1.5 mm diameter Al/(Si _{0.76} N _{0.24})Si-rich, 3 nm/N-rich, 4 nm (9.5 periods multilayers)/(50 ohm per square) ITO/glass	Well heights are modulated by varying R _N . If R _N increases (66 to 92%) then barrier height increases (0.2 to 1 eV). EL _{max} at 500 nm for R _N = 88%. EL deterioration for R _N > 88% due to lattice mismatch.

Figure B.4: Literature review chart of a-SiN_x:H based LEDs (continued).

Year	Source gas	Flow parameters	Power	Press. (Torr)	Subst. Temp. (°C)	Post deposition treatment	Device structure	Comments
13-2008	>90% H ₂ -diluted SiH ₄ , PH ₃ , B ₂ H ₆ and GeH ₄ , Pure NH ₃ and C ₂ H ₂ .	<i>p</i> -layer: SiH ₄ :B ₂ H ₆ = 100:36 varying C ₂ H ₂ :NH ₃ = 3->0:0->4 (last 1 min.) (sccm). <i>i</i> -layer: SiH ₄ :NH ₃ = 100:18. <i>n</i> -layer: SiH ₄ :PH ₃ :NH ₃ = 100:72: (18->4) (sccm). SiH ₄ :PH ₃ :C ₂ H ₂ :GeH ₄ = 100:72: (0->3) : (0->5) (sccm). SiH ₄ :PH ₃ = 100:72 (sccm).	14 mW/cm ²	0.25-0.5	180	H ₂ , 7 mW/cm ² , 0.3 Torr, 10 min, after each layer. After contact growth, rapid annealing at 300°C under H ₂ for 25 min	Glass/TiO ₂ /p-a-Si:H/p-a-SiC:H/p-a-SiN:H/i-a-SiN:H/n-a-SiN:H/n-a-SiC:H/n-a-Si:H/1.13×10 ² cm ² Al, where <i>p</i> and <i>n</i> layers are composition graded (CG)	Rapid annealing treatment improves device performance. Besides DC white LEDs, nearly symmetrical AC ones were fabricated discarding the <i>p</i> and <i>n</i> layers of the pin diode. DC LEDs: 200 cd/m ² at 600 mA/cm ² at 460 nm. AC LEDs: 170 cd/m ² at 100 mA/cm ² at 535 nm. AC LEDs have less power dissipation, lower turn-on voltage (8.4 V), better stability (20 min for EL intensity to drop to 50% of its initial value at 9 V rms) when compared to DC ones.
14-2008	Oxide: N ₂ O/SiH ₄ Nitride: NH ₃ /SiH ₂ Cl ₂ (dichlorosilane)	Oxide: N ₂ O:SiH ₄ = 9.17 for nanocrystalline Si of 3.6 nm and 5×10 ¹⁷ cm ⁻³ density (PECVD). Nitride: mixture (LPCVD).	0.07 mW/cm ²	0.2	300 (PECVD) 800 (LPCVD)	Nitrogen post deposition on the Si rich oxide.	N-doped semitransparent poly Si (250 nm)/15 nm nitride/55 nm Si rich oxide with 20% excess Si/ <i>p</i> -Si (0.1-4 Ωcm, 3×10 ¹⁶ cm ⁻³)/Al.	MOS and MNOS LEDs were fabricated for comparison. MNOS outperformed MOS by more than 1 order of magnitude in EL power. Very dense nanocrystallites for N ₂ O:SiH ₄ = 9.17. Nitride avoids leakage current. MNOS $\xi_{\text{power}} = 0.1\%$ and more stable (a few months). Performance: 0.2 μs rise, 10 μs fall.

Figure B.5: Literature review chart of a-SiN_x:H based LEDs (continued).

APPENDIX C

SPECTRAL RESPONSIVITIES OF THE PHOTODETECTORS

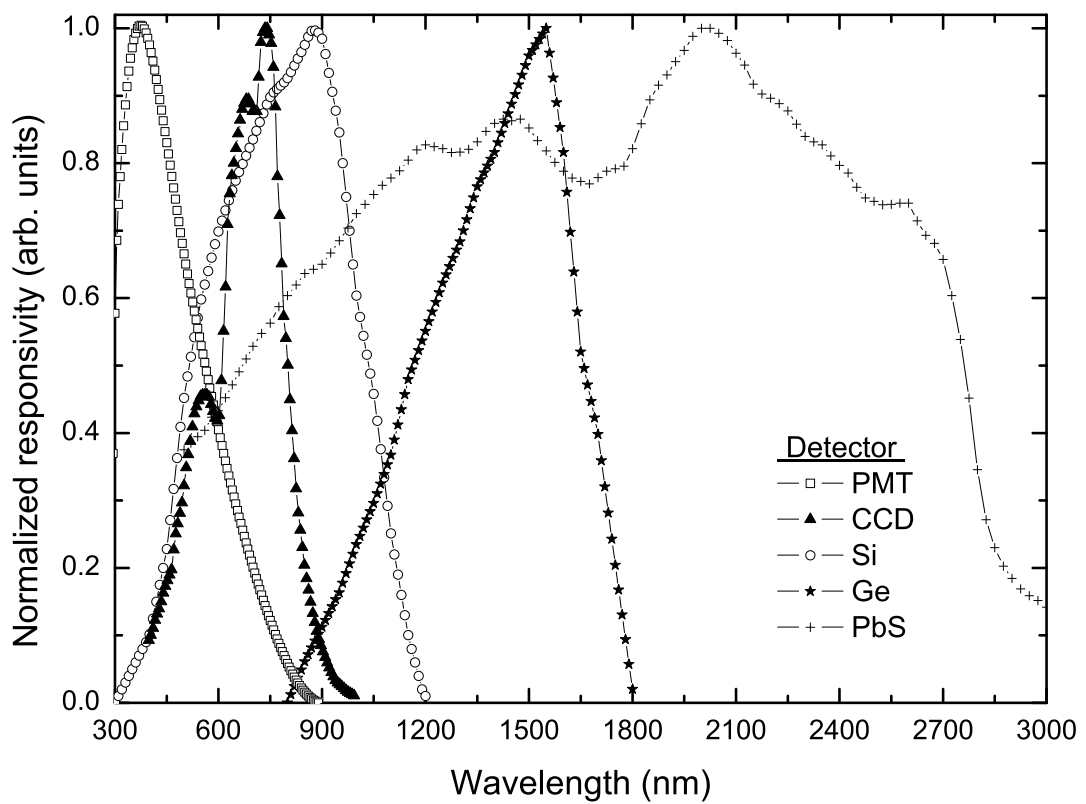


Figure C.1: The normalized spectral responsivities of the PMT, CCD, Si, Ge and PbS detectors.

The photodetector to be used in the luminescence experiments should be chosen correctly for the best results. Each detector given in Fig. C.1 has its own characteristic responsivity curve. For the emissions in the visible region, the PMT should be preferred due to its high sensitivity and suitable spectral responsivity. CCD is a must for fast and/or time resolved

measurements. However, the intensity of the emission needs to be high enough as the sensitivity of a CCD is much lower when compared to PMT. The Si photodiode can be used if the spectrum of the visible luminescence exceeds about 800 nm. When the emission energy is low in the near-infrared region, Ge photodiode and PbS should be utilized. The sensitivity of the non-cooled Ge photodiode is low whose output is noisy when the emission intensity is moderate. The PbS used in this work is cooled down to about 243 K in order to reduce its dark current and to enhance its sensitivity. For luminescence spectra of energy lower than 1 eV (i.e. wavelengths longer than about 1200 nm) PbS may be a good choice.

APPENDIX D

DERIVATION OF THE TOTAL ABSORBED LIGHT FRACTION USED IN PL INTENSITY CORRECTION

Fig. D.1 shows the intensity changes of the incident light (I_0 , 325 nm line of a HeCd UV laser used as the excitation source in PL measurements) at the air/film, film/Si wafer interfaces during its multiple internal reflections. Here T_f , R_f and R_{Si} are the air/film transmission, air/film reflection and film/Si wafer reflection coefficients, defined as follows:

$$\begin{aligned} T_f &= \frac{4n_{air}n_{film}}{(n_{air} + n_{film})^2}, \\ R_f &= \frac{(n_{air} - n_{film})^2}{(n_{air} + n_{film})^2}, \\ R_{Si} &= \frac{(n_{film} - n_{Si})^2}{(n_{film} + n_{Si})^2}. \end{aligned} \quad (D.1)$$

The exponential term in Fig. D.1 includes α - the absorption coefficient of the film at the excitation energy and d - the film thickness. As it is described in section 2.3, the as-measured PL intensity should be divided by the fraction of the absorbed intensity, A , in order to compare quantitatively the PL output of the different films. AI_0 is found by extracting the light intensity at the film/Si wafer interface from that at the air/film interface and vice-versa following the path of Fig. D.1. So, A is defined as:

$$\begin{aligned} A &= (T_f - T_f e^{-\alpha d}) + (T_f R_{Si} e^{-\alpha d} - T_f R_{Si} e^{-2\alpha d}) + (T_f R_{Si} R_f e^{-2\alpha d} - T_f R_{Si} R_f e^{-3\alpha d}) + \\ &\quad (T_f R_{Si}^2 R_f e^{-3\alpha d} - T_f R_{Si}^2 R_f e^{-4\alpha d}) + (T_f R_{Si}^2 R_f^2 e^{-4\alpha d} - T_f R_{Si}^2 R_f^2 e^{-5\alpha d}) + \\ &\quad (T_f R_{Si}^3 R_f^2 e^{-5\alpha d} - T_f R_{Si}^3 R_f^2 e^{-6\alpha d}) + \dots \end{aligned} \quad (D.2)$$

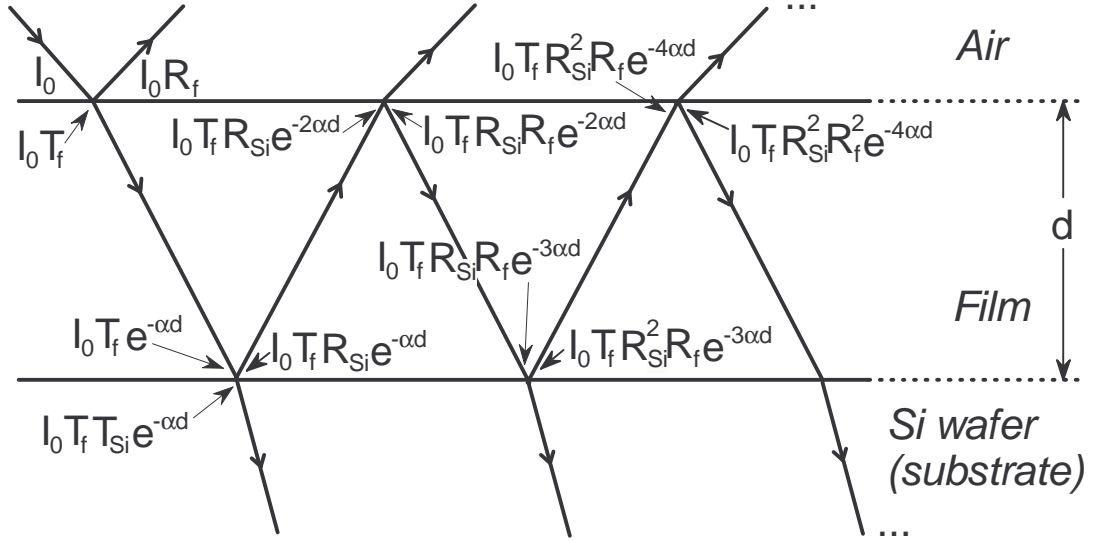


Figure D.1: The schematic representation of the path followed by a ray of light incident on the air/film interface and the modifications in its intensity during its travel within the bulk of the film.

Each of the parentheses has the common term $(1 - e^{-\alpha d})$ so that the above expression is grouped as:

$$A = T_f (1 - e^{-\alpha d}) (1 + R_{Si} e^{-\alpha d} + R_{Si} R_f e^{-2\alpha d} + R_{Si}^2 R_f e^{-3\alpha d} + R_{Si}^2 R_f^2 e^{-4\alpha d} + R_{Si}^3 R_f^2 e^{-5\alpha d} + \dots). \quad (D.3)$$

Next, the common term $(R_{Si} e^{-\alpha d} (1 + R_f e^{-\alpha d}))$ in the second parenthesis of equation D.3 is grouped as:

$$A = T_f (1 - e^{-\alpha d}) (1 + R_{Si} e^{-\alpha d} (1 + R_f e^{-\alpha d}) (1 + R_{Si} R_f e^{-2\alpha d} + R_{Si}^2 R_f^2 e^{-4\alpha d} + \dots)). \quad (D.4)$$

The term $(1 + R_{Si} R_f e^{-2\alpha d} + R_{Si}^2 R_f^2 e^{-4\alpha d} + \dots)$ has a form of $\Sigma = (1 + x + x^2 + x^3 + x^4 + \dots)$, where $x = R_{Si} R_f e^{-2\alpha d}$. Using the short formula for $\Sigma = \frac{1}{1-x}$ the equation D.4 is modified as following:

$$A = T_f (1 - e^{-\alpha d}) \left(1 + \frac{R_{Si} e^{-\alpha d} (1 + R_f e^{-\alpha d})}{1 - R_{Si} R_f e^{-2\alpha d}} \right). \quad (D.5)$$

The second parenthesis in the above equation is simplified and $(1 - R_f)$ is written instead of T_f to obtain the final form of A:

$$\begin{aligned}
A &= T_f (1 - e^{-\alpha d}) \left(\frac{1 - R_{S_i} R_f e^{-2\alpha d} + R_{S_i} e^{-\alpha d} + R_{S_i} R_f e^{-2\alpha d}}{1 - R_{S_i} R_f e^{-2\alpha d}} \right) = \\
&= (1 - R_f) (1 - e^{-\alpha d}) \left(\frac{1 + R_{S_i} e^{-\alpha d}}{1 - R_{S_i} R_f e^{-2\alpha d}} \right). \tag{D.6}
\end{aligned}$$

APPENDIX E

SPACE CHARGE LIMITED CURRENT SPECTROSCOPY

The energy distribution of DOS below the conduction band edge of the intrinsic layer (a-Si:H) of the diode #5 was deduced from the experimental diode I-V data at room temperature. In this purpose, the space charge limited current (SCLC) spectroscopy was utilized for the region that deviated from the extrapolated linear fit in the diode I-V curve, as shown in Fig. 4.5. The derivation of the formula used in this DOS calculation is provided below through the ‘differential method’ [73, 116].

Since the doping efficiency and the majority carrier mobility of the n -layer are much higher than those of p -layer, the current transport may be assumed to be dominated by the electrons in a-Si:H based homojunction pin diode. Therefore, only the electron transport is considered in the following derivations. Neglecting the diffusion current, the current-voltage characteristics of a semiconductor are given by the set of equations:

$$J = e\mu n_f(x)F(x) \quad (\text{E.1})$$

$$\frac{dF(x)}{dx} = \frac{e}{\epsilon} [n_f(x) + n_t(x)] \quad (\text{E.2})$$

$$- \int_0^d F(x)dx = V \quad (\text{E.3})$$

where J is the current density, μ -drift mobility, n_f -free carrier density, F -electric field, ϵ -electric permittivity, n_t -trapped carrier density, d -film thickness, V -voltage. Here, n_f and n_t are by described Boltzmann and Fermi-Dirac distribution functions, respectively:

$$n_f(x) = N_b \exp\left(-\frac{E_f(x)}{kT}\right) \quad (\text{E.4})$$

$$n_t(E, x) = \frac{h(E)}{1 + \exp\left(\frac{E - E_f(x)}{kT}\right)} \quad (\text{E.5})$$

where $h(E)$ is the distribution of trap levels within the forbidden gap, defined as:

$$h(E) = \frac{dn_t(x)}{dE}. \quad (\text{E.6})$$

The electric field and the voltage drop at the anode (Cr) are related by:

$$F(d) = \kappa_1 \frac{V}{d}, \quad (\text{E.7})$$

where κ_1 is a dielectric dependent constant with value between 1 and 2.

Then, the Fermi level at the anode may be estimated after the substitution of Eq. E.4 and E.7 into E.1:

$$E_F(d) = -kT \ln \frac{d}{\kappa_1 N_b e \mu} - kT \ln \frac{J}{V}. \quad (\text{E.8})$$

The above equation supplies the dependence of the Fermi level on the I-V characteristics of the diode, which in turn permits the trap occupancy analysis at the anode.

Now, let us consider the derivative of total-to-free carrier ratio (θ^{-1}) with respect to the energy $E_F(d)$:

$$\frac{d(\ln \theta^{-1})}{dE_F(d)} = \frac{d \left[\ln \frac{n_f(d) + n_t(d)}{n_f(d)} \right]}{dE_F(d)}. \quad (\text{E.9})$$

The ratio θ^{-1} can be modified in the following way:

$$\begin{aligned} \frac{n_f(d) + n_t(d)}{n_f(d)} &= \frac{[n_f(d) + n_t(d)] e \mu F(d)}{n_f(d) e \mu F(d)} \\ &= \frac{[n_f(d) + n_t(d)] e \mu \frac{e}{\epsilon} d [n_f(d) + n_t(d)]}{J} \\ &= \frac{\frac{e^2 d^2}{\epsilon^2} [n_f(d) + n_t(d)]^2 \frac{\mu \epsilon}{d}}{J} = \frac{F^2 \frac{\mu \epsilon}{d}}{J} \\ &= \frac{F^2 d^2 \frac{\mu \epsilon}{d^3}}{J} = \frac{\kappa_1^2 \mu \epsilon \frac{V^2}{d^3}}{J} = \frac{J_M}{J} \end{aligned} \quad (\text{E.10})$$

To make use of Eq. E.2 in the second line of the above equation, the carrier density throughout the sample is assumed to be constant. Eq. E.7 is applied for the last simplification.

J_M is the Mott's current derived from his SCLC model. As a result, Eq. E.9 can be rewritten as:

$$\frac{d\left[\ln\frac{n_f+n_t}{n_f}\right]}{dE_F} = \frac{d\left[\ln\frac{J_M}{J}\right]}{dE_F}. \quad (\text{E.11})$$

After taking partial derivatives, the left hand side of Eq. E.11 can be modified as:

$$\frac{d\left[\ln\frac{n_f+n_t}{n_f}\right]}{dE_F} = \frac{1}{n_f+n_t} \left(\frac{dn_t}{dE_F} + \frac{n_t}{kT} \right). \quad (\text{E.12})$$

In parallel, using the differential form of Eq. E.8, the right hand side of Eq. E.11 can be simplified as follows:

$$\frac{d\left[\ln\frac{J_M}{J}\right]}{dE_F} = \frac{a-2}{kT(a-1)}, \quad (\text{E.13})$$

where a is the differential slope of the I-V curve in the log-log scale ($d[\ln J]/d[\ln V]$).

Equating Eq. E.12 and Eq. E.13, the following is obtained:

$$\frac{dn_t}{(n_f+n_t)d(-E_F/kT)} = \frac{1}{a-1} - \theta. \quad (\text{E.14})$$

For $n_t \gg 0$ or $\theta \ll 1$ the above equation is reduced to:

$$\frac{d(\ln(n_t))}{d(-E_F/kT)} = \frac{1}{a-1}. \quad (\text{E.15})$$

The energy states below the quasi-Fermi level should be totally filled in the steady state condition, i.e. $n_t \approx N_t$. Eq. E.6 at the Fermi level can be obtained using Eq. E.15:

$$\begin{aligned} h(E_F) &= \frac{dn_t}{dE_F} = -\frac{n_t}{kT(a-1)} \\ &= -\frac{n_0}{kT(a-1)} \exp\left(\frac{1}{kT} \int_{E_0}^{E_F} \frac{1}{a-1} dE_F\right), \end{aligned} \quad (\text{E.16})$$

where n_0 and E_0 are the boundary values. Here, the integral variable E_F can be changed into V using Eq. E.8 and can be solved to give out:

$$h(E_F) = \frac{AV}{kT(a-1)}, \quad (\text{E.17})$$

where $A = n_0/U_0$ and U_0 is the lowest applied voltage. To determine the constant A , the $h(E_F)$ should be normalized as:

$$N_t = \int_{E_0}^{E_{TFL}} h(E_F) dE_F, \quad (\text{E.18})$$

where E_{TFL} is the trap filling limit of the quasi-Fermi level for the occupancy of the whole trap states. By making use of Eq. E.8 and Eq. E.17 this integration is solved as:

$$N_t = n_0 \left(\frac{U - U_0}{U_0} \right), \quad (\text{E.19})$$

where $U = 2U_{TFL}$ with $U_{TFL} = (eN_t d^2)/(\epsilon\kappa_1\kappa_2)$ is considered to be the upper limit for the voltage corresponding to E_{TFL} [106]. Since $U_{TFL} \gg U_0$, the constant A in Eq. E.18 can be extracted and the final form of Eq. E.17 becomes:

$$h(E_F) = \frac{\epsilon\kappa_1\kappa_2}{2ed^2} \frac{V}{kT(a-1)}, \quad (\text{E.20})$$

where $\frac{1}{2} \leq \kappa_2 \leq 1$ is a constant accounting for the non-uniformity in the electrical properties of the film.

APPENDIX F

BAND-TAIL HOPPING RESULTS FOR D3

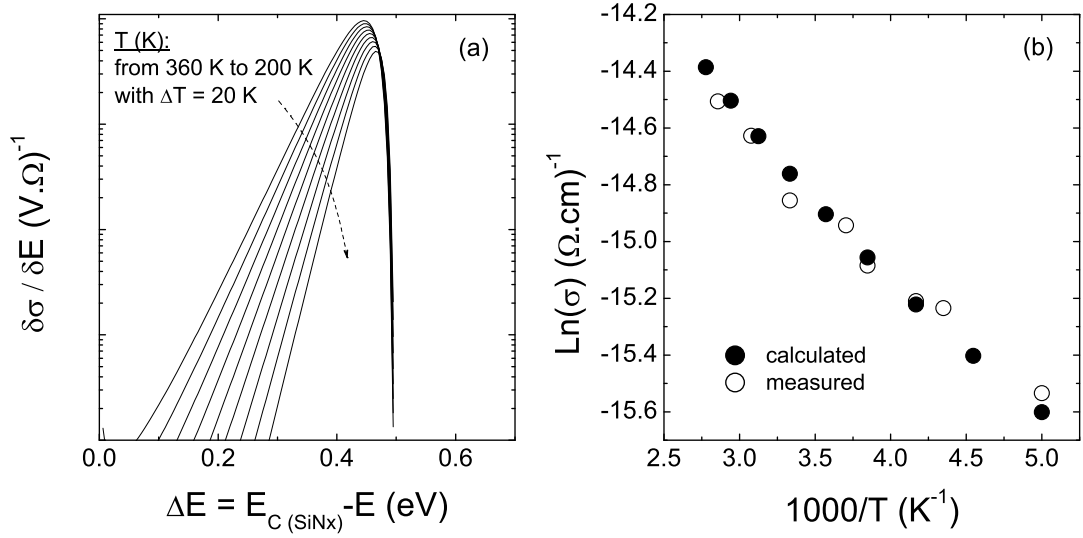


Figure F.1: (a) Differential conductivity of D3 versus energy measured from the conduction band edge. (b) Arrhenius plot of calculated and measured conductivity data. In the calculations, h_0^c and E_0 are taken as 7×10^{22} and 600 meV, respectively.

VITA

Born in Safranbolu, Turkey, on August 9, 1983, Mustafa Anutgan graduated from Safranbolu Anatolian High School in 2001. In 2005, he received B.S. degree in Advanced Physics from Middle East Technical University (METU). During 2005-2007, he conducted his M.S. studies in Physics at METU on plasma deposited boron nitride thin films. Since 2007, he has carried out his Ph.D. studies at the Solid State Electronics Lab in METU Physics Department. His main research topics are production/characterization of amorphous/nanocrystalline thin films and their application in devices, such as *pin* light emitting diodes, thin film transistors.

His publications include:

1. M. Anutgan, T. (Aliyeva) Anutgan, I. Atilgan, B. Katircioglu, Photoluminescence analyses of hydrogenated amorphous silicon nitride films. (2010) Submitted to Journal of Luminescence.
2. T. Aliyeva Anutgan, M. Anutgan, I. Atilgan, B. Katircioglu, Optimization of n^+ nc-Si:H and a-SiN_x:H layers for their application in nc-Si:H TFT. (2010) Submitted to Vacuum.
3. T. Aliyeva Anutgan, M. Anutgan, I. Atilgan, B. Katircioglu, Capacitance analyses of hydrogenated nanocrystalline silicon based TFT. (2010) Submitted to Thin Solid Films.
4. T. Aliyeva Anutgan, M. Anutgan, I. Atilgan, B. Katircioglu, Large area uniformity of plasma grown hydrogenated nanocrystalline silicon and its application in TFTs. J. Non-Cryst. Solids 356 (2010) pp. 1102-1108.
5. T. Aliyeva Anutgan, M. Anutgan, I. Atilgan, B. Katircioglu, Stability and degradation of plasma deposited boron nitride thin films in ambient atmosphere. Thin Solid Films 518 (1) (2009) pp. 419-425.
6. M. Anutgan, T. Aliyeva Anutgan, E. Ozkol, I. Atilgan, B. Katircioglu, Influence of the

- nitrogen flow rate on the order and structure of PECVD boron nitride thin films. *J. Non-Cryst. Solids* 355 (2009) pp. 1622-1629.
7. O. Ozdemir, M. Anutgan, T. Aliyeva Anutgan, I. Atilgan, B. Katircioğlu, Electrical transport mechanism in boron nitride thin film. *J. Non-Cryst. Solids* 355 (2009) pp. 851-859.
 8. O. Ozdemir, M. Anutgan, T. Aliyeva Anutgan, I. Atilgan, B. Katircioğlu, Annealing improvement on the localized states of plasma grown boron nitride film assessed through admittance measurements. *J. Alloys Comp.* 475 (2009) pp. 794-803.
 9. T. Aliyeva Anutgan, M. Anutgan, O. Ozdemir, I. Atilgan, B. Katircioglu, Effect of heat treatment on the stress and structure evolution of plasma deposited boron nitride thin films. *Surf. Coat. Technol.* 202 (13) (2008) pp. 3058-3066.
 10. O. Ozdemir, M. Anutgan, T. Aliyeva Anutgan, I. Atilgan, B. Katircioğlu, Instability phenomenon originated from disordered layer of plasma deposited BN film/c-Si interface assessed through MIS structure by admittance measurement. *Semicond. Sci. and Technol.* 23 (2008) (025006) pp. 1-8.
 11. M. Anutgan, Investigation of plasma deposited boron nitride thin films. M.S. Thesis, METU, July 2007.
 12. O. Özdemir, M. Anutgan, İ. Atılğan, B. Katircioğlu, Investigation of instability phenomenon on AlBNSiAl MIS structure via admittance and FTIR spectroscopies. GeT Univation Conference, Germany, 24 February 2007, p. 84.
 13. O. Özdemir, M. Anutgan, İ. Atılğan, B. Katircioğlu, Instability evolution within boron nitride film through MIS structure. GeT Univation Conference, Germany, 24 February 2007, p. 83.
 14. A. Dâna, O. Ergun, M. Anutgan, T. Aliyeva, A. Aydinli, R. Turan, Charging dynamics of MOS capacitors containing PECVD grown germanium nanocrystals. SEMINANO 2005, Budapest, Hungary.